Electronic Supplementary Material (ESI) for Journal of Materials Chemistry A.
This journal is © The Royal Society of Chemistry 2017

Supporting Information

Porphyrinic Coordination Lattices with Fluoropillars

Qipu Lin,[a†] Chengyu Mao,[a] Aiguo Kong,[a] Xianhui Bu,*[b] Xiang Zhao[a] and Pingyun Feng*[a]

[a]Department of Chemistry, University of California, Riverside, CA 92521, United States.

[b]Department of Chemistry and Biochemistry, California State University, 1250 Bellflower Boulevard, Long Beach, CA 90840, United States.

[†]State Key Laboratory of Structural Chemistry, Fujian Institute of Research on the Structure of Matter, Chinese Academy of Sciences, Fuzhou 350002, China.

*To whom correspondence should be addressed.

E-mail: pingyun.feng@ucr.edu; xianhui.bu@csulb.edu

Table of Contents

1. General methods (materials and instrumentation)

2. Procedures for ligand synthesis

3. Characterization of ligands

4. Synthesis of CPM-13X

5. Single crystal X-ray diffraction analysis

6. Photographs of crystals

7. Characterization of CPM-13X

8. Additional structural pictures

9. Gas sorptions

10. Pyrolysis of CPM-13X (to CPM-13X/C)

11. Characterization of CPM-13X/C

12. Electrocatalytic activities for ORR

13. Supplementary reference

1. General methods

Materials: All of the reagents used were obtained from commercial supplies without further purification. 4-pyridinecarboxaldehyde (97%, C_6H_5NO, 107.11, Sigma-Aldrich), pyrrole (98%, C_4H_5N, 67.09, Sigma-Aldrich), propionic acid (99.5%, CH_3CH_2COOH, 74.08, Sigma-Aldrich), $ZnSiF_6 \cdot xH_2O$ (99%, ~207.47, Sigma-Aldrich).

Instrumentation: Solution ^1H NMR spectroscopic data were recorded for samples in 5 mm tubes (outer diameter) with a Varain Inova 300 NMR spectrometer. Mass spectrometry (MS) was performed on a Finnigan LCQ-3 instrument, using a Pauli ion trap to collect, resolve and detect ions. Elemental Analysis (EA) was carried out with a Perkin-Elmer 2400 CHNS Elemental Analyzer (Atlantic Microlab, Inc.). Single-crystal X-ray analysis was performed on a Bruker APEX II diffractometer with nitrogen-flow temperature controller using graphite-monochromated MoKα radiation (λ = 0.71073 Å), operating in the ω and φ scan mode. The SADABS programme was used for absorption correction. The structures were solved by direct method followed by successive difference Fourier method. All atoms (except H) were refined anisotropically. Computations were performed using SHELXTL[1] and final full-matrix refinements were against F^2. Powder X-ray diffraction (PXRD) experiments were carried out with a Bruker D8 Advance X-ray powder diffractometer operating at 40 kV and 40 mA (Cu Kα radiation, λ = 1.5418 Å). The data collection was performed with a step size of 0.02 ° and counting time of 2 second per step. The simulated powder XRD pattern was obtained from the single-crystal data. Microscopic imaging was carried out at the UCR Microscopy Core at the Institute for Integrative Genome Biology (IIGB). The thermogravimetric analysis (TGA) was carried out using a TA Instruments TGA Q500 apparatus in the temperature range of 30 ℃ to 800 ℃ under N_2 flow at a heating rate of 2 ℃·min^{-1}. Nitrogen, hydrogen, carbon dioxide, methane and acetylene adsorption-desorption isotherms were obtained on a Micromeritics ASAP 2020/2010 physisorption analyzer. Prior to the measurement, the as-synthesized crystal sample was dried by using the "degas" function of the surface area analyzer for 12 hr at 100 ℃. Liquid N_2, acetone-dry ice, ice water, and water were used as the temperature controlling media for 77, 195, 273, and 298 K, respectively. UV-vis (liquid absorption and solid-state diffuse reflectance) spectra were recorded on a Shimadzu UV-3101PC spectrophotometer.

Fourier transformed-Infrared spectroscopy (FT-IR) was performed on a Thermo Nicolet Avatar 6700 FT-IR with cesium iodide optics allowing the instrument to observe from 525 to 4000 cm^{-1}. Scanning electron microscopy (SEM) images were taken on Nova NanoSEM450 (Schottky field emission scanning electron microscope) integrated with energy-dispersive X-ray (EDX) allowing to perform qualitative and quantitative chemical analysis, and image capture. Transmission electron microscope (TEM) images were obtained on a JEM-2010 transmission electron microscope at an acceleration voltage of 200 kV. X-ray photoelectron spectroscopy (XPS) measurements were made on a Kratos analytical AXIS Ultra Delay-Line Detector (DLD) Imaging XPS equipped with a vacuum ultraviolet light source, using C 1s (284.8 eV) as a reference to correct the binding energy (Francisco Zaera Surface Group, UCR). Liquid fluorescence spectra were recorded on Spex Fluorolog Tau-3 fluorescence spectrophotometer.

Electrocatalytic activities for ORR of the as-prepared catalysts were evaluated by cyclic voltammetry (CV) and rotating disk electrode (RDE) techniques on a CHI-650 electrochemical analyzer. A three-electrode cell was employed using a glass carbon RDE (5mm in diameter, Pine) as working electrode, an Ag/AgCl, KCl (3 M) electrode as the reference electrode, and a Pt wire electrode as the counter electrode. The ORR experiments were carried out in 0.1 M KOH or 0.1 M $HClO_4$ solution. The potential was scan between -1~+0.2 (base) or -0.2~+1 (acid) V (*versus* Ag/AgCl) at a scan rate of 10 mV s^{-1} at the ambient temperature after purging O_2 or Ar gas for 20 min. All the working electrodes were prepared as following: 5 mg of catalysts and 40 μL of Nafion solution (5 wt%) were dispersed in 600 μL of ethanol by sonication for 30 min to form a homogeneous ink. Then, 5 (base) or 15 (acid) μL of ink was loaded onto polished glassy carbon rotating disk electrode of 0.196 cm^2 surface, and the electrode was dried at room temperature. Electrolyte was saturated with oxygen by bubbling O_2 prior to the measurements. A flow of O_2 was maintained over the electrolyte during the measurements. For the RDE recording, the working electrode was scanned cathodically at a rate of 10 mV s^{-1} with varying rotating speed from 400 to 2500 rpm. Commercial 20 wt% Pt/C catalysts obtained from Alfa Aesar were used for comparison. The catalyst loading of active Pt-free catalysts on the working electrode is 0.2 (base) or 0.6 (acid) mg cm^{-2} in 0.1 M KOH or $HClO_4$ solution. For Pt/C, the loading of active material is 10

μg Pt cm^{-2} (0.1 mg Pt/C cm^{-2}). All the potentials were calibrated to the potentials *versus* RHE (Potentials *versus* RHE = potential *versus* Ag/AgCl+0.949 (base), +0.268 (acid) V).

The Koutecky-Levich plots (J^{-1} vs $\omega^{-1/2}$) were analyzed at various electrode potentials. The slopes of the linear lines were used to calculate the number of electrons transferred (n) according to the following Koutechy-Levich equation.

$$\frac{1}{J} = \frac{1}{J_L} + \frac{1}{J_K} = \frac{1}{B\omega^{1/2}} + \frac{1}{J_K} \qquad \text{(K-L)}$$

$$B = 0.62nFC_0(D_0)^{2/3}\upsilon^{-1/6}$$

$$J_K = nFkC_0$$

where J, J_K and J_L are the measured current density, kinetic- and diffusion-limiting current densities, respectively; ω is the angular velocity of the disk, n is the electrons transferred number, F is the Faraday constant (=96485 C mol^{-1}), C_0 is the bulk concentration of O_2 (C_0 = 1.2 × 10^{-3} mol L^{-1} in 0.1 M KOH), D_0 is diffusion coefficient of O_2 (D_0 = 1.9 × 10^{-5} cm s^{-1} in 0.1 M KOH), υ is the kinematic viscosity of the electrolyte (υ = 0.01 cm^2 s^{-1} in 0.1 M KOH), and k is the electron transfer rate constant. The number of electrons transferred (n) and J_K can be obtained from the slope and intercept of the K–L plots. An accelerated assessment experiment by cycling CV curves from 0.2 to -1.0 V (*versus* Ag/AgCl) was used to measure the stability of electrode materials, with a scanning rate of 2 V s^{-1}.

2. Procedures for ligand synthesis

Ligands of 5,10,15,20-tetrapyridylporphyrin and its metallated analogues (TPyP-M, M = H_2, Fe, Zn, Cu) were synthesized based on Adler's method with modifications.[2] Typically, we obtained these ligands by two steps as follows:

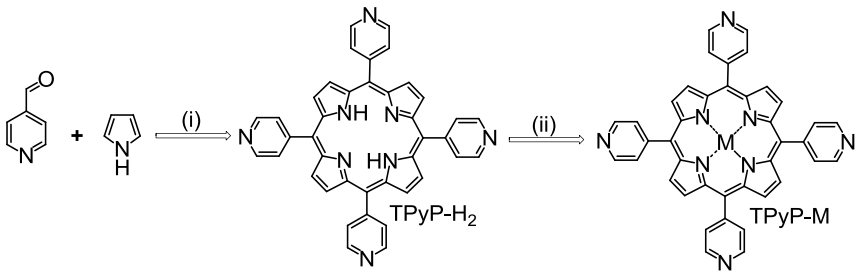

Scheme S1. Synthetic route for TPyP-M (M = H_2, Fe, Zn, Cu). Reagents and conditions: (i) propionic acid, reflux, 3 hr; (ii) $FeCl_2{\cdot}4H_2O$ or $Zn(OAc)_2{\cdot}2H_2O$ or $Cu(OAc)_2{\cdot}2H_2O$, $MeOH/CHCl_3$, reflux, 12 hr.

(1) 5,10,15,20-Tetrakis(4-pyridyl)porphyrin (TPyP-H_2): 4-pyridinecarboxaldehyde (4.28 g, 40 mmol) was stirred in propionic acid (300 mL) and heated to reflux. To refluxed solution was added pyrrole (2.77 mL, 40 mmol), then solution was refluxed for 3 hr in darkness. After cooled to room temperature, crude purple product was collected by suction-filtration. The crude product was chromatographed on silica (CH_2Cl_2/hexane = 20/1) to yield 3.5 g (49% yield). ^{1}H NMR ($CDCl_3$): δ = 9.08 (t, 8H), 8.87 (s, 8H), 8.16 (t, 8H), -2.92 (s, 2H). MS (FAB) calcd for $C_{40}H_{26}N_8$ $[M+H]^+$ 619.2314, found 619.2372. FT-IR: ν = 3680 (w), 3310 (w), 2970 (m), 2360 (s), 1740 (m), 1590 (s), 1400 (m), 970 (m), 783 (m) cm^{-1}. EA data: C 76.13, H 4.15, N 17.65; calculated: C 77.65, H 4.24, N 18.11 %.

(2) 5,10,15,20-Tetrakis(4-pyridyl)porphyrin-Fe(II) (TPyP-Fe): A solution of TPyP-H_2 (0.62 g, 1.0 mmol) and $FeCl_2{\cdot}4H_2O$ (1.60 g, 8 mmol) in 100 mL of $CHCl_3$ (mixed by 30 mL of CH_3OH) and the mixture was heated to reflux for 12 hr. After cooling down to room temperature, the $CHCl_3/CH_3OH$ was removed under reduced pressure. The obtained solid was washed three times with methanol, dried to give quantitative dark red crystals. ^{1}H NMR (d_6-DMSO): δ = 8.97 (t, 8H), 8.79 (s, 8H), 8.17 (t, 8H). MS (FAB) calcd for $C_{40}H_{24}N_8FeCl$ $[M+H]^+$ 708.9702, found 708.0012. FT-IR: ν = 2970 (m), 2360 (s), 1600 (s), 1490 (m), 1220 (m), 1070 (s), 858 (m), 796 (s) cm^{-1}. EA data: C 66.92, H 3.56, N 15.27; calculated: C 67.86, H 3.42, N 15.83 %.

(3) 5,10,15,20-Tetrakis(4-pyridyl)porphyrin-Zn(II) (TPyP-Zn): A solution of TPyP-H_2 (0.62 g, 1.0 mmol) and Zn(OAc)·$2H_2O$ (2.19 g, 10 mmol) in 100 mL of $CHCl_3$ (mixed by 30 mL of CH_3OH) and the mixture was heated to reflux for 12 hr. After cooling down to room temperature, the $CHCl_3/CH_3OH$ was removed under reduced pressure. The obtained solid was washed three times with water and methanol, dried to give quantitative dark red crystals. ^{1}H NMR (d_6-DMSO): δ = 8.99 (t, 8H), 8.81 (s, 8H), 8.19 (t, 8H). MS (FAB) calcd for $C_{40}H_{24}N_8Zn$ $[M+H]^+$ 681.1485, found 681.1489. FT-IR: ν = 2970 (w), 2360 (m), 1590 (s), 1340 (m), 1070 (s), 991 (s), 789 (s) cm^{-1}. EA data: C 69.32, H 3.63, N 15.87; calculated: C 70.44, H 3.55, N 16.43 %.

(4) 5,10,15,20-Tetrakis(4-pyridyl)porphyrin-Cu(II) (TPyP-Cu): A solution of TPyP-H_2 (0.62 g, 1.0 mmol) and Cu(OAc)·$4H_2O$ (2.49 g, 10 mmol) in 100 mL of $CHCl_3$ (mixed by 30 mL of CH_3OH) and the mixture was heated to reflux for 12 hr. After cooling down to room temperature, the $CHCl_3/CH_3OH$ was removed under reduced pressure. The obtained solid was washed three times with water and methanol, dried to give quantitative dark red crystals. ^{1}H NMR (d_6-DMSO): δ = 8.96 (t, 8H), 8.79 (s, 8H), 8.16 (t, 8H). MS (FAB) calcd for $C_{40}H_{24}N_8Cu$ $[M+H]^+$ 681.2182, found 680.1519. FT-IR: ν = 3310 (w), 2990 (s), 2360 (s), 1610 (s), 1400 (m), 1000 (m), 795 (s) cm^{-1}. EA data: C 69.05, H 3.59, N 15.97; calculated: C 70.63, H 3.56, N 16.47 %.

3. Characterization of ligands

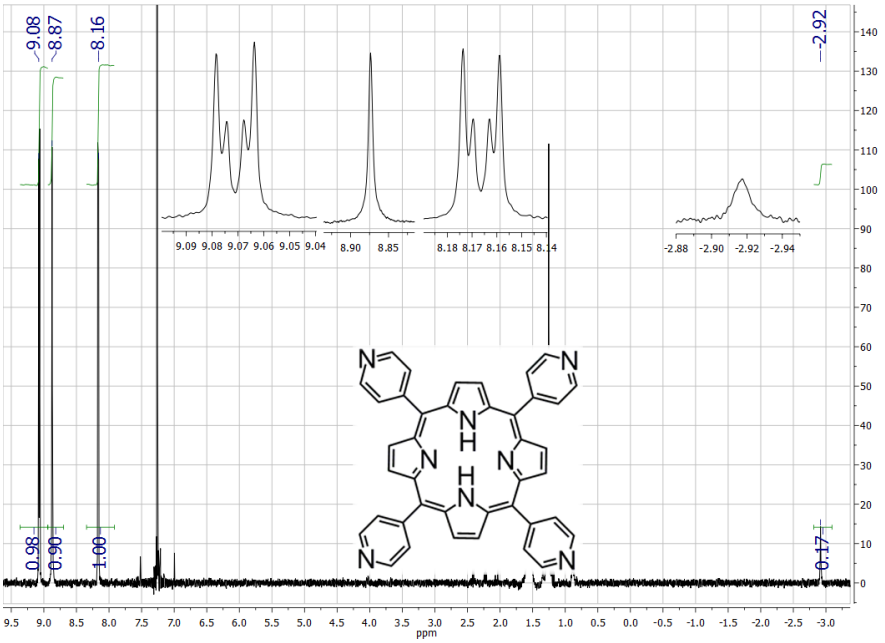

Fig. S1 ^{1}H NMR spectrum of TPyP-H_2 in $CDCl_3$ solution.

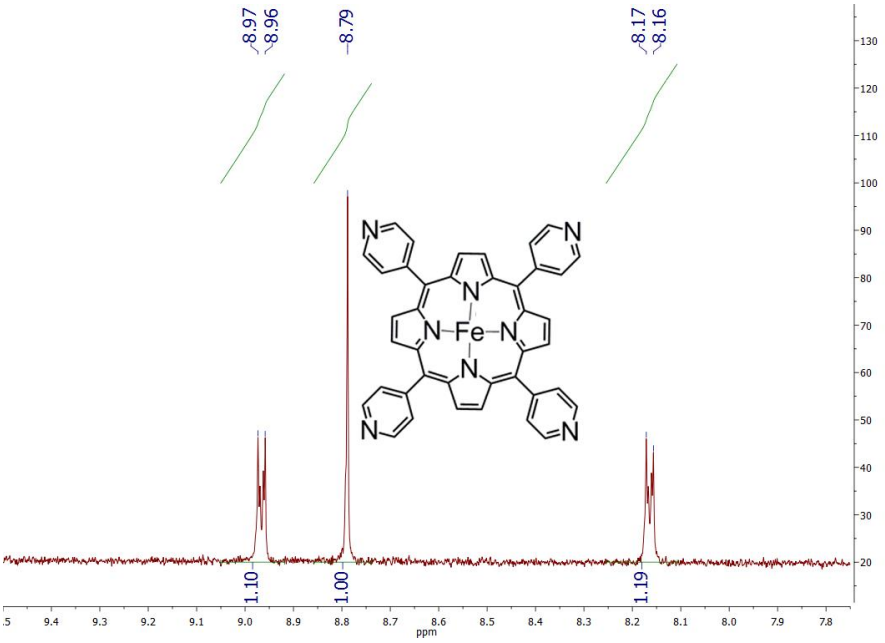

Fig. S2 ^{1}H NMR spectrum of TPyP-Fe in d_6-DMSO solution.

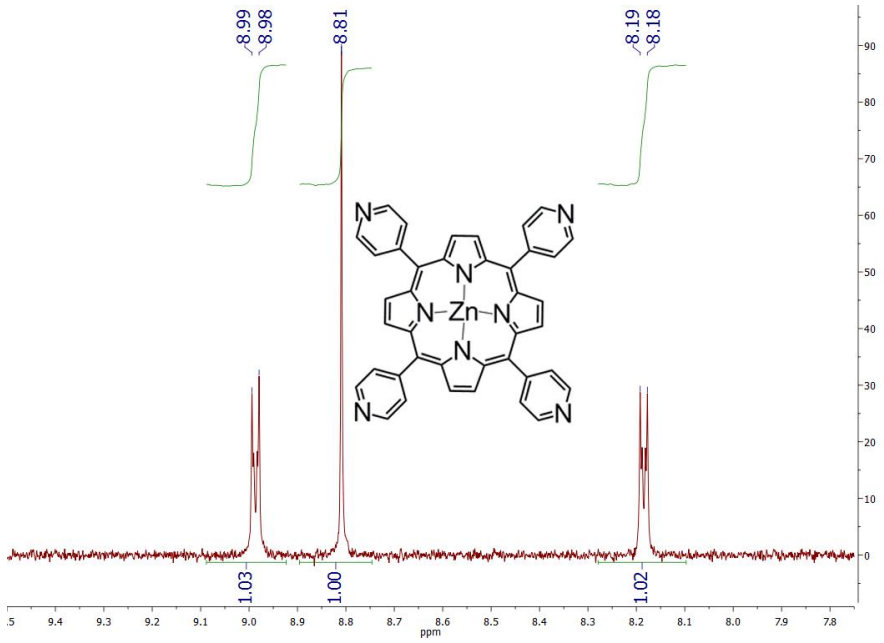

Fig. S3 ^{1}H NMR spectrum of TPyP-Zn in d_6-DMSO solution.

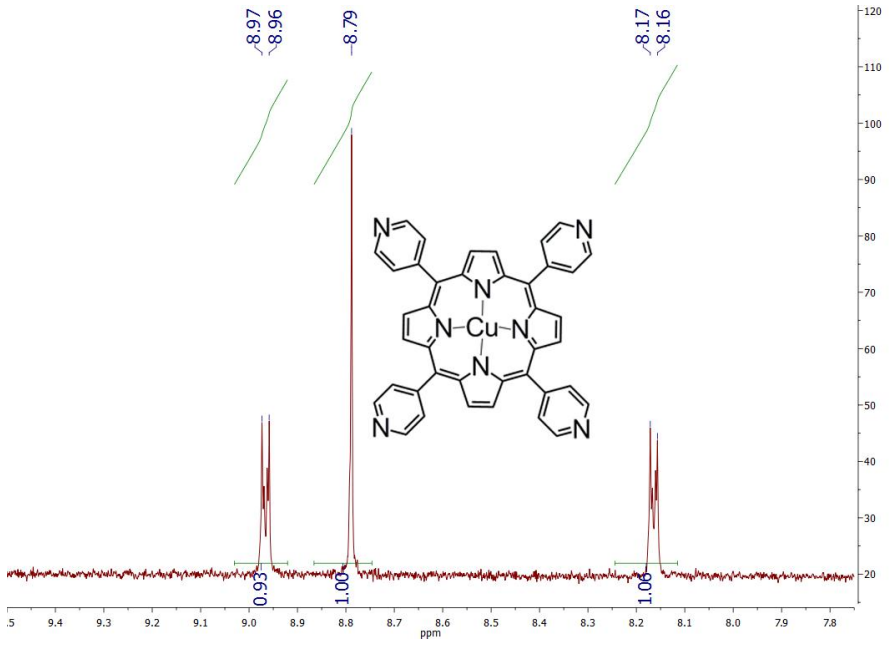

Fig. S4 ^{1}H NMR spectrum of TPyP-Cu in d_6-DMSO solution.

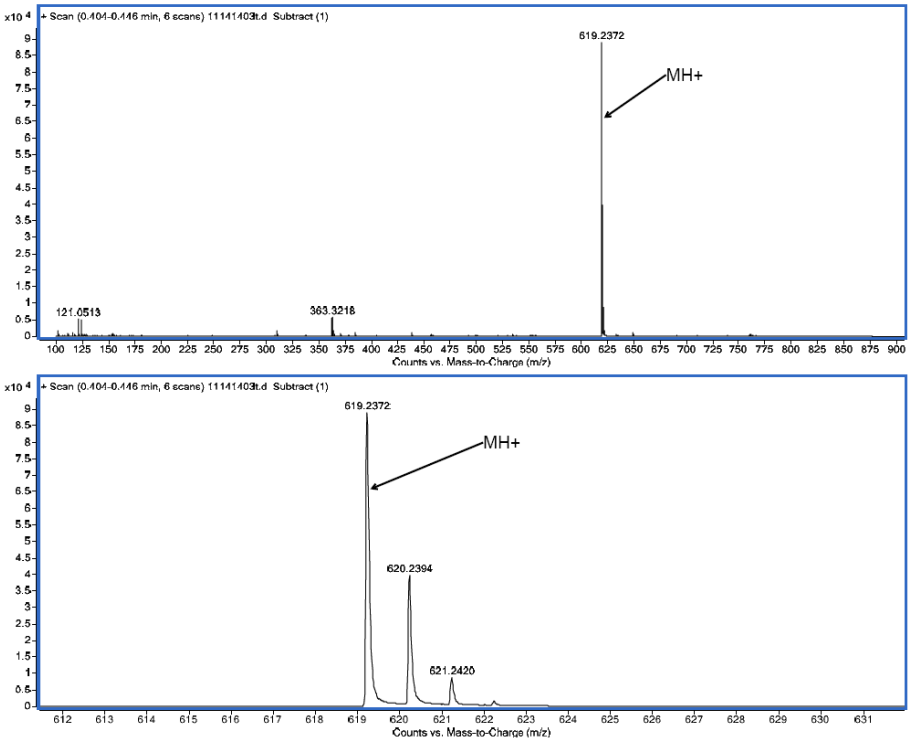

Fig. S5 Mass spectrum of TPyP-H_2.

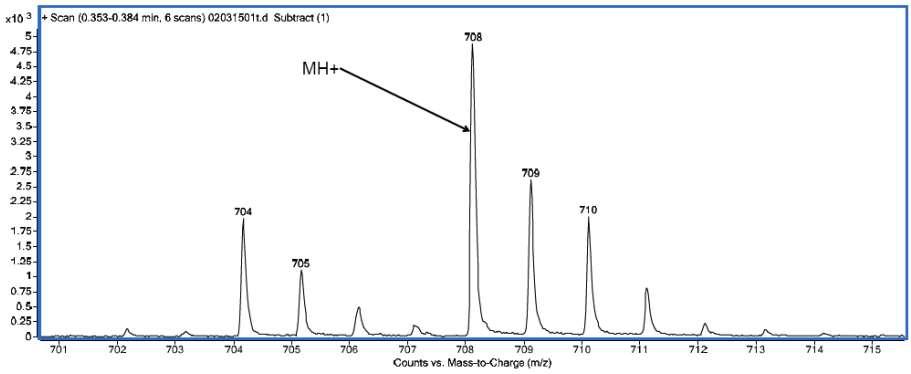

Fig. S6 Mass spectrum of TPyP-Fe.

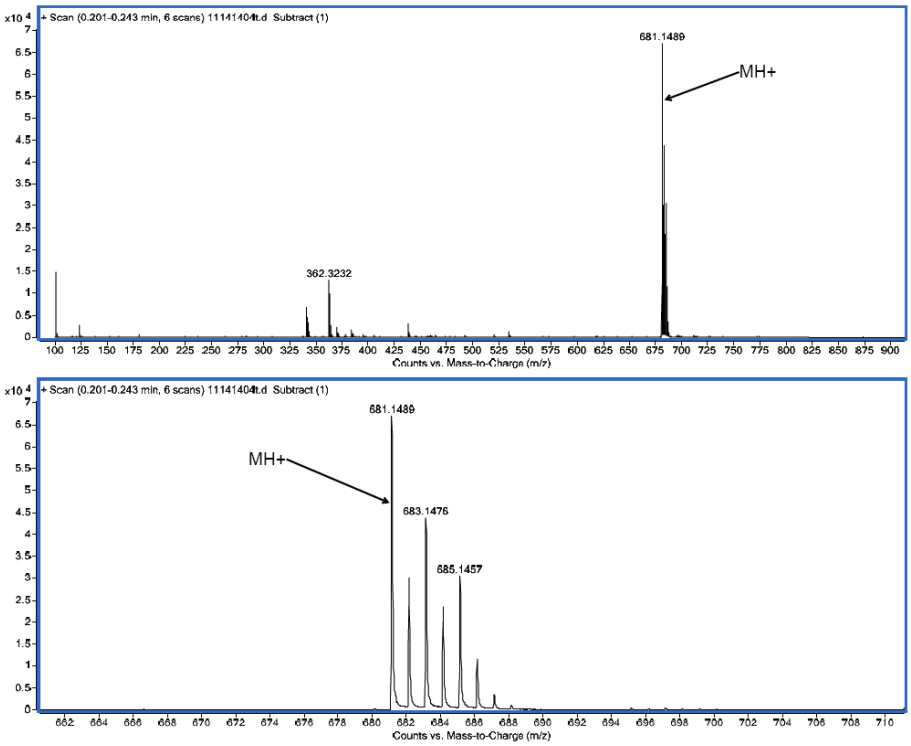

Fig. S7 Mass spectrum of TPyP-Zn.

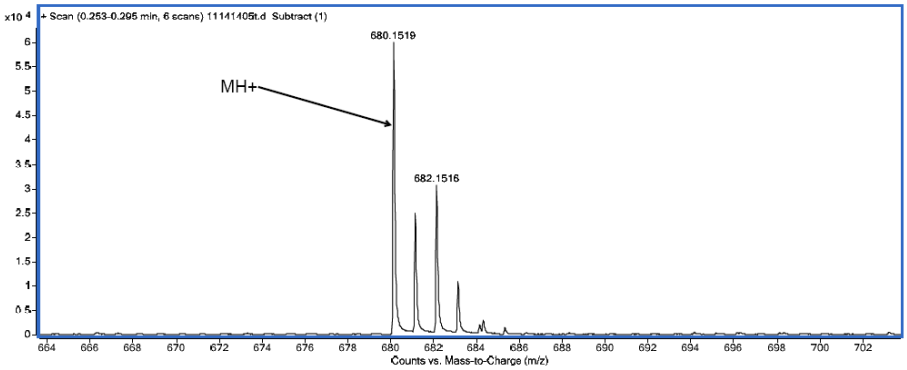

Fig. S8 Mass spectrum of TPyP-Cu.

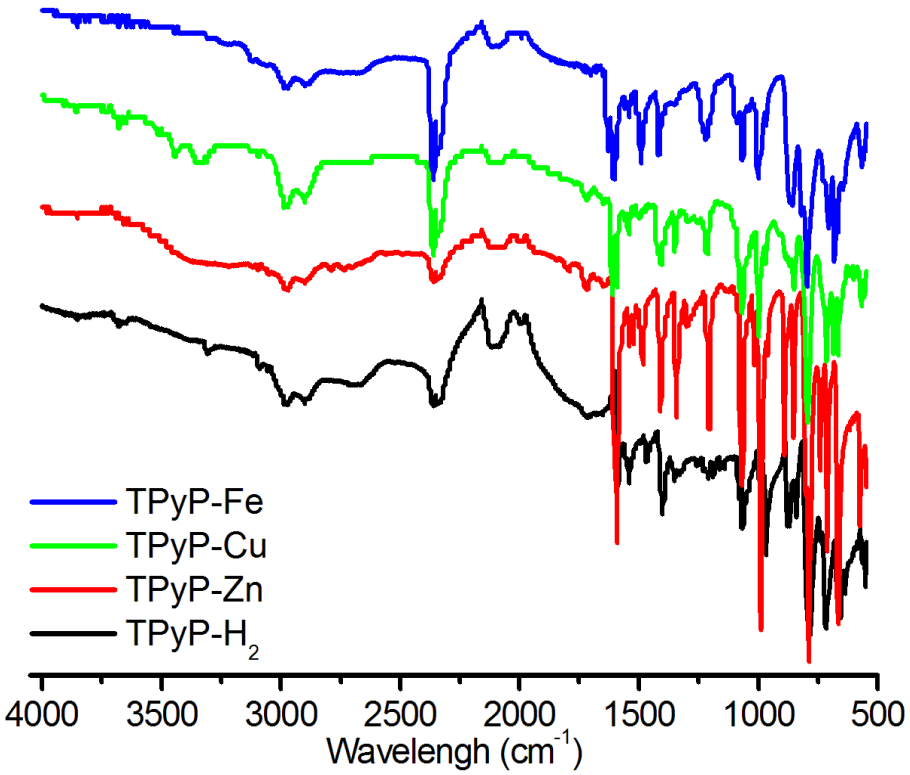

Fig. S9 FT-IR spectra of TPyP-M ligands.

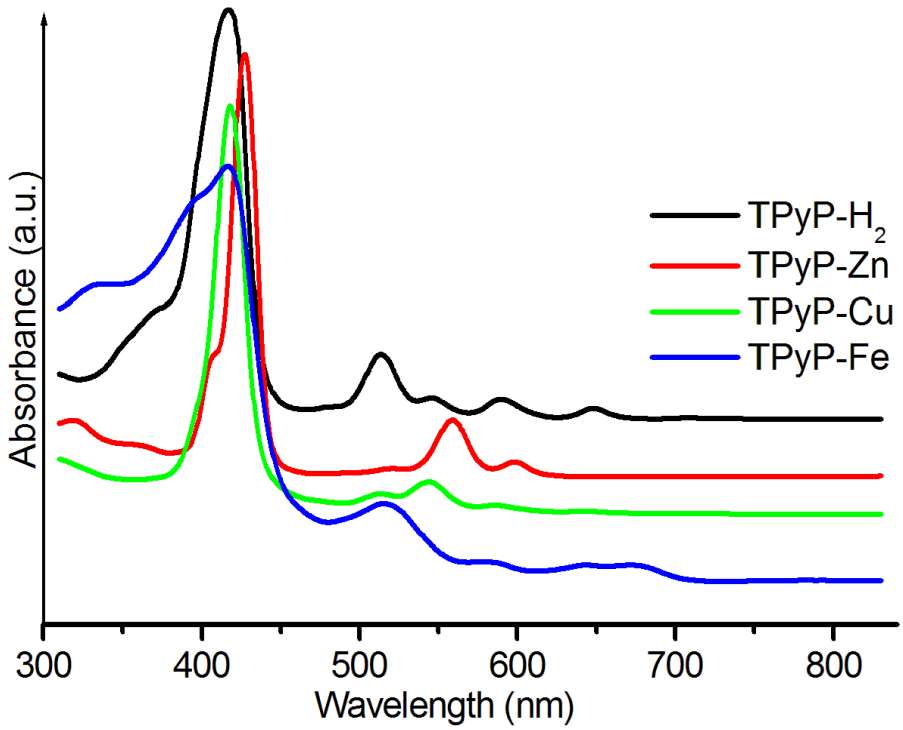

Fig. S10 UV-Vis absorbance spectra of TPyP-H_2 (in $CHCl_3$) and TPyP-M (M = Fe/Zn/Cu, in DMSO).

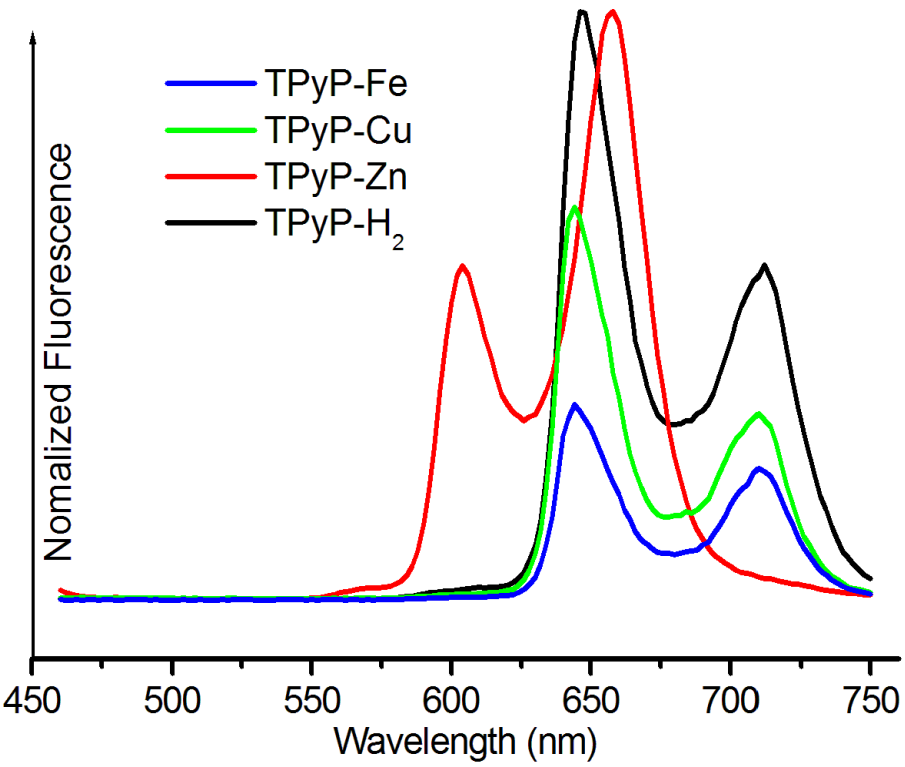

Fig. S11 Fluorescence emission spectra of TPyP-(H_2, Fe, Zn, Cu) at a scan wavelength (λ_{ex}) of ca. 435 nm.

4. Synthesis of CPM-13X

(1) CPM-131 ([(TPyP-Fe)Zn(SiF_6)]$_n$**-fsc)**: A solution of 10 mg of TPyP-Fe in 8 mL of *N*-methyl-2-pyrrolidone was layered over a solution of 10 mg of $ZnSiF_6 \cdot xH_2O$ in 3 mL of ethylene glycol in vial. Interdiffusion of the solutions (at room temperature or heated at 80 ℃) for a period of 5 days yielded square-shaped crystals (42% yield based on TPyP-Fe). FT-IR: ν = 3680 (m), 2990 (s), 2360 (w), 1610 (s), 1410 (s), 1070 (s), 715 (s) cm^{-1}. EA data: C 49.37, H 3.14, N 11.18 %.

(2) CPM-132 ([(TPyP-Zn)$_2$$F_2$$Zn_2$($SiF_6$)]$_n$**-fsx)**: A solution of 10 mg of $ZnSiF_6 \cdot xH_2O$ in 3 mL of propylene glycol was layered over a solution of 10 mg of TPyP-Zn in 10 mL of dimethylsulfoxide (mixed with 2 mL of chloroform) in vial. Low temperature (60 ℃) diffusion of the solutions for a period of 6 days yielded square-shaped crystals (62% yield based on TPyP-Zn). FT-IR: ν = 2990 (s), 2360 (m), 1650 (m), 1610 (s), 1420 (m), 991 (s), 717 (s) cm^{-1}. EA data: C 51.45, H 3.67, N 12.35 %.

(3) CPM-133 ([TPyP-Cu]$_n$**-nbo)**: TPyP-Cu (0.10 g) was dissolved in 4 mL of *N*,*N*-diethylacetamide solution (with 1 drop of concentrated nitric acid) firstly, then 1 mL of ethanol was added. The mixture was heated in 120 ℃ oven for 3 days. After cooling down to room temperature, hexagonal prism-shaped crystals were harvested by filtration (43% yield based on TPyP-Cu). FT-IR: ν = 3680 (m), 2990 (s), 2360 (m), 1590 (s), 1410 (s), 991 (s), 789 (s), 667 (s) cm^{-1}. EA data: C 68.07, H 3.73, N 15.90 %.

5. Single crystal X-ray diffraction analysis

Materials of CPM-13X suitable for single-crystal X-ray diffraction have been obtained in our experiments. The single crystal intensity data were collected on a Bruker APEX-II diffractometer with nitrogen-flow temperature controller using graphite-monochromated MoKα radiation (λ = 0.71073 Å), operating in the ω and φ scan mode. The SADABS programme was used for absorption correction. The structures were solved by direct method followed by successive difference Fourier method. Non-hydrogen atoms were refined with anisotropic displacement parameters during the final cycles. Hydrogen atoms were placed in calculated positions with isotropic displacement parameters set to 1.2 × U_{eq} of the attached atom. CCDC 1061788-1061790 contain the supplementary crystallographic data for this paper. These data can be obtained free of charge from the Cambridge Crystallographic Data Centre via www.ccdc.cam.ac.uk/data_request/cif.

Table S1 Crystal Data and Structure Refinements for CPM-13X in this study.

Compound reference	CPM-131	CPM-132	CPM-133
Chemical formula	$C_{40}H_{24}F_6FeN_8O_2SiZn$	$C_{84}H_{52}Cl_{12}F_8N_{16}SiZn_4$	$C_{40}H_{24}CuN_8$
Formula Mass	912.00	2152.47	680.22
Crystal system	Tetragonal	Tetragonal	Rhombohedral
a/Å	13.9664(3)	13.985(10)	33.0984(19)
b/Å	13.9664(3)	13.985(10)	33.0984(19)
c/Å	7.7060(5)	24.40(4)	9.3673(11)
α/ °	90.00	90.00	90.00
β/ °	90.00	90.00	90.00
γ/ °	90.00	90.00	120.00
Unit cell volume/ Å^3	1503.13(11)	4772(9)	8887.1(13)
Temperature/K	195(2)	195(2)	195(2)
Space group	*P4/mmm*	*I4/m*	*R-3*
Z (No. of formula units per unit cell)	1	2	9
No. of reflections measured	6590	4827	13910
No. of independent reflections	735	2576	3506
R_{int}	0.0539	0.1011	0.0774
GOF	0.993	0.992	1.002
Final R_1 values ($I > 2\sigma(I)$)	0.0883	0.0875	0.0444
Final $wR(F^2)$ values ($I > 2\sigma(I)$)	0.2524	0.2165	0.0836
Final R_1 values (all data)	0.0973	0.2014	0.0736
Final $wR(F^2)$ values (all data)	0.2595	0.2780	0.0899

$R_1 = \sum||F_o| - |F_c||/\sum|F_o|$, $wR = \{\sum w[(F_o)^2 - (F_c)^2]^2/\sum w[(F_o)^2]^2\}^{1/2}$.

6. Photographs of crystals

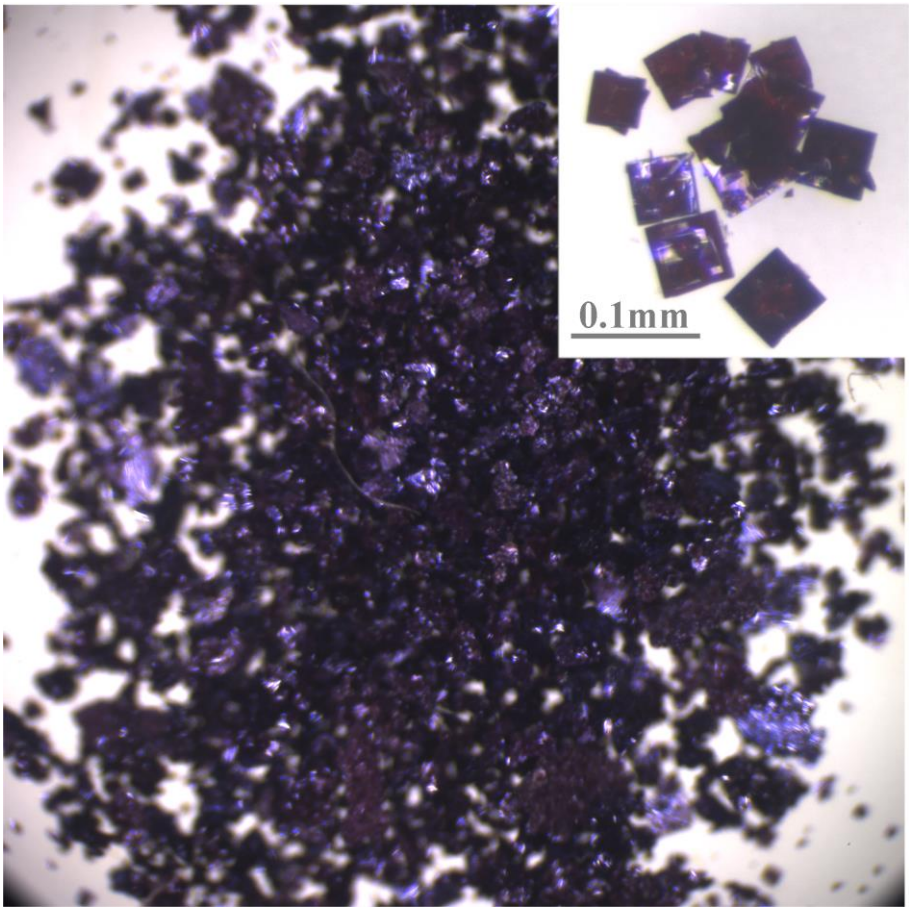

Fig. S12 Photograph of CPM-131.

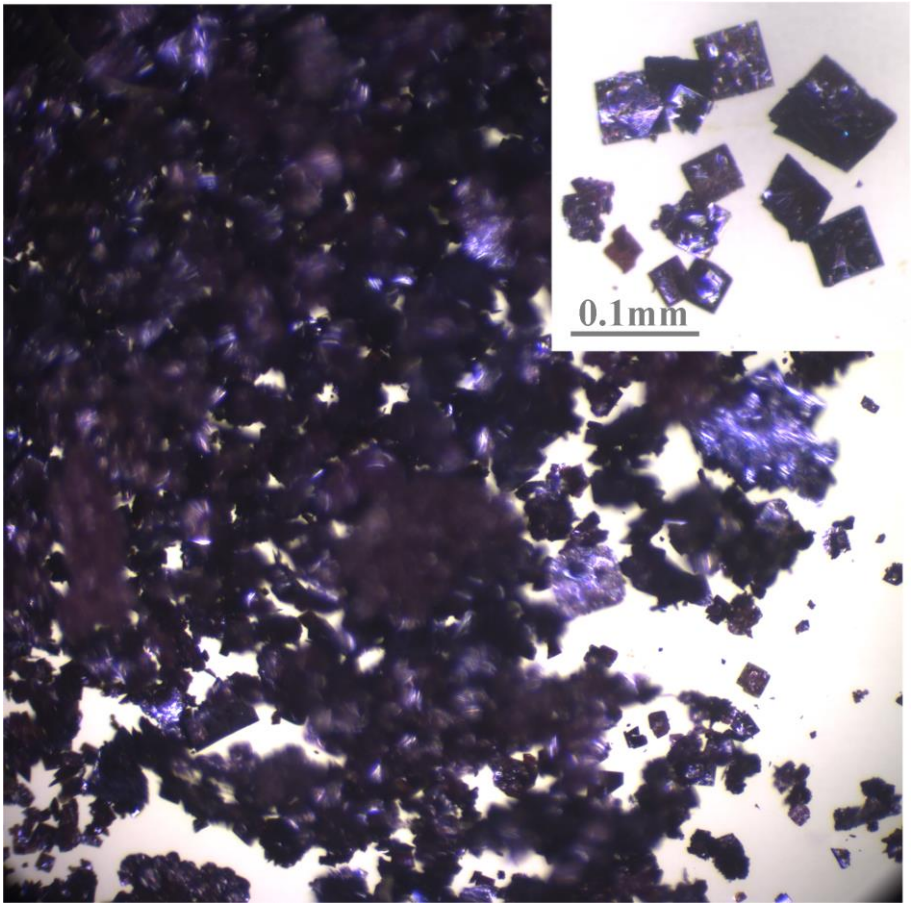

Fig. S13 Photograph of CPM-132.

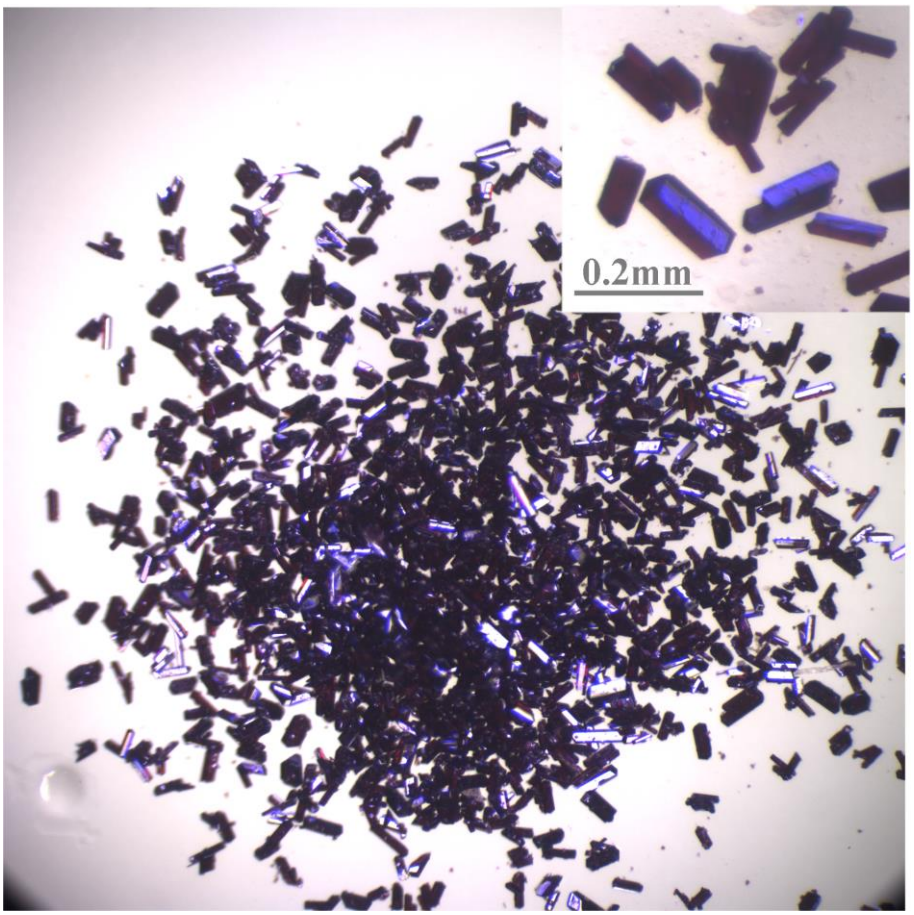

Fig. S14 Photograph of CPM-133.

7. Characterization of CPM-13X

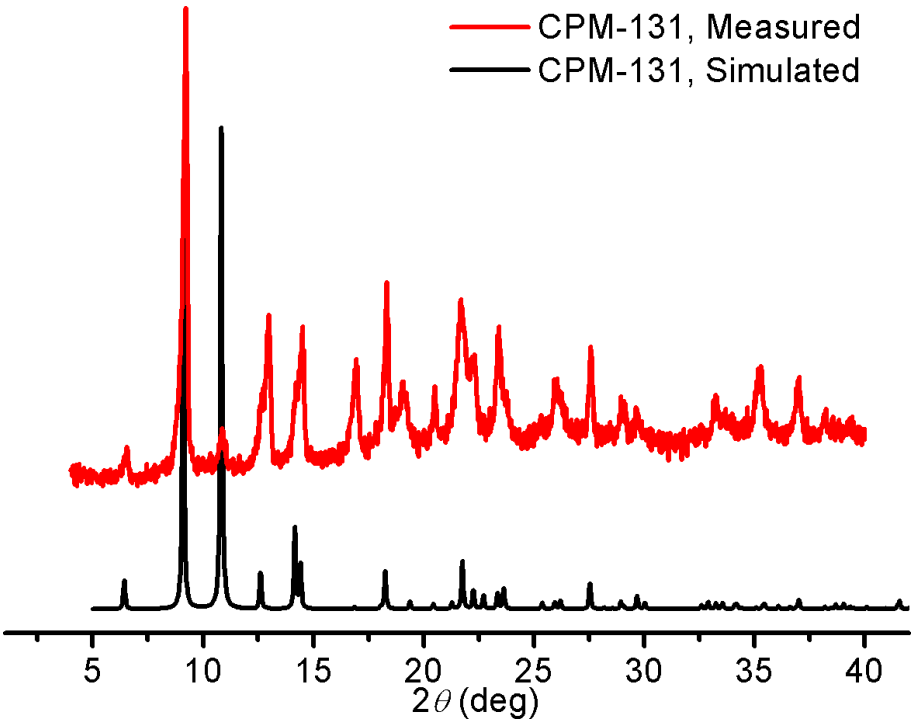

Fig. S15 Measured and simulated PXRD patterns of CPM-131.

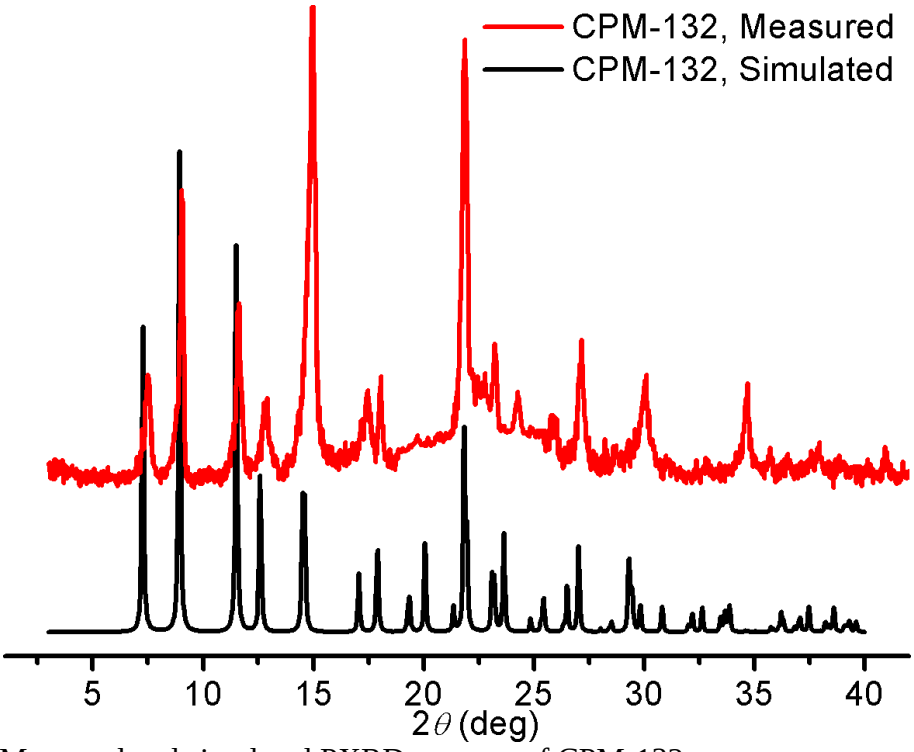

Fig. S16 Measured and simulated PXRD patterns of CPM-132.

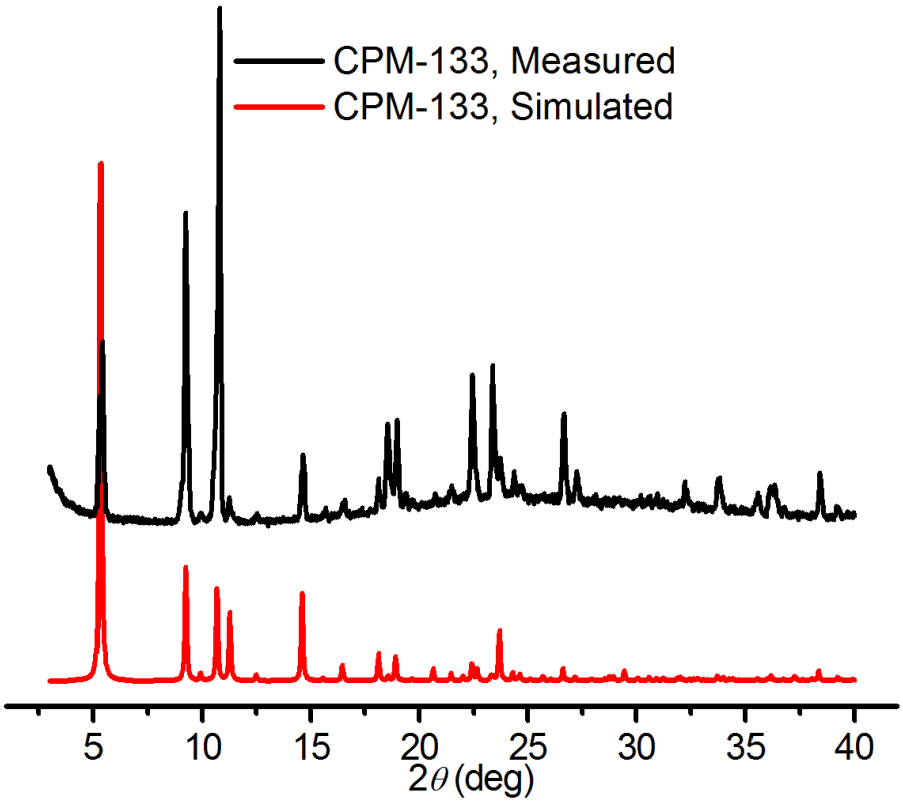

Fig. S17 Measured and simulated PXRD patterns of CPM-133.

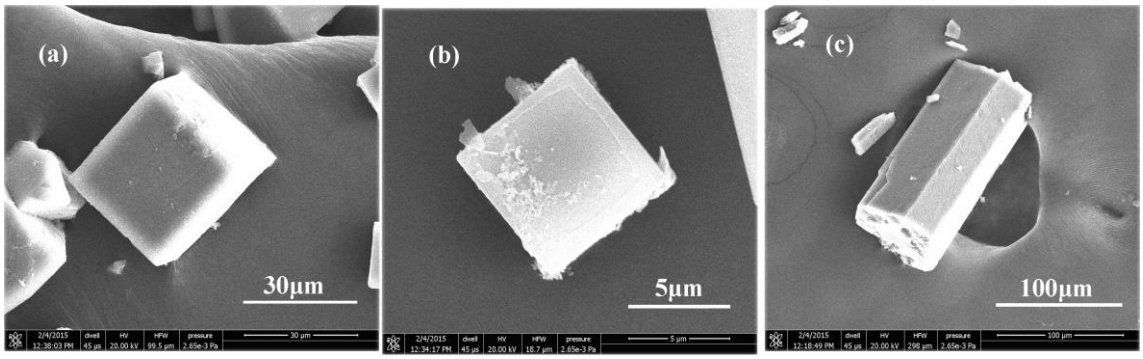

Fig. S18 SEM images of (a) CPM-131, (b) CPM-132, and (c) CPM-133.

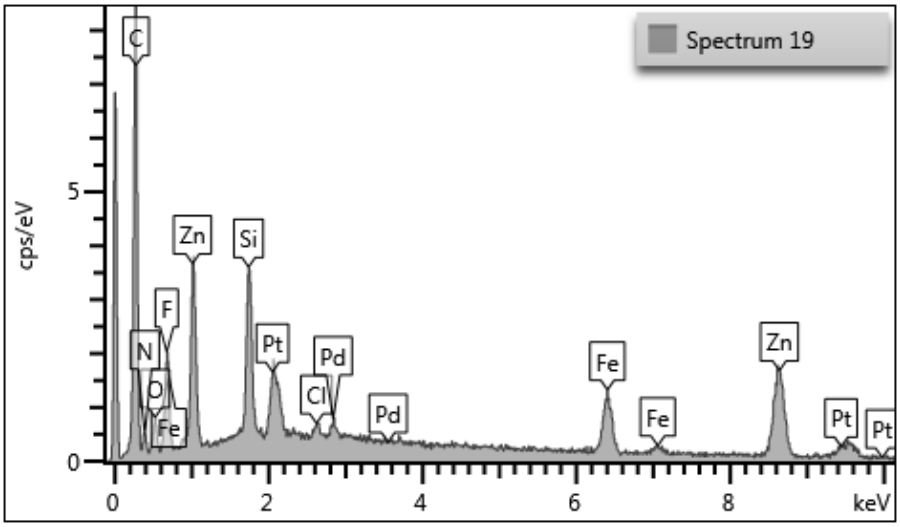

Fig. S19 EDX of the crystal CPM-131 (coated with Pd/Pt).

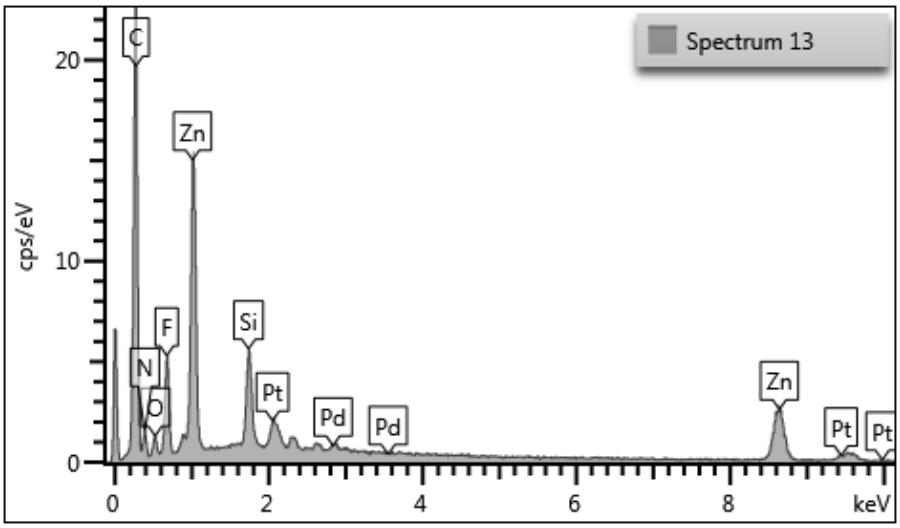

Fig. S20 EDX of the crystal CPM-132 (coated with Pd/Pt).

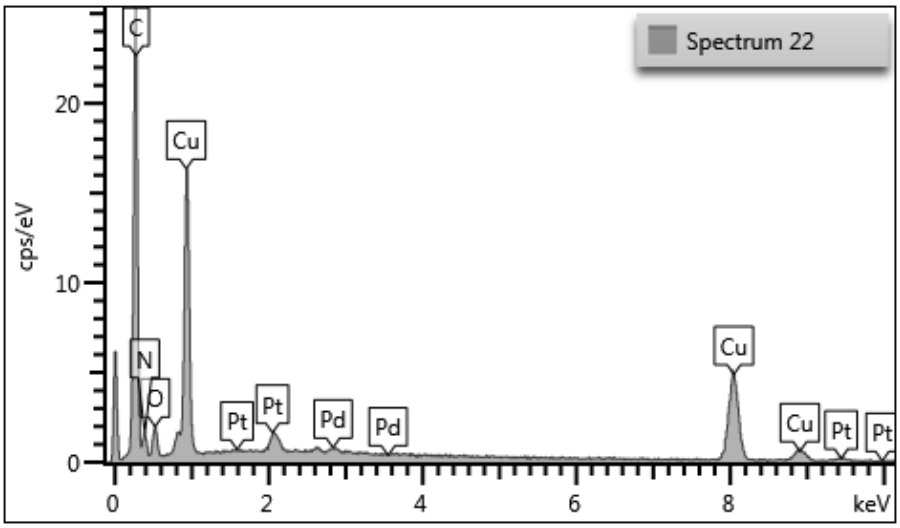

Fig. S21 EDX of the crystal CPM-133 (coated with Pd/Pt).

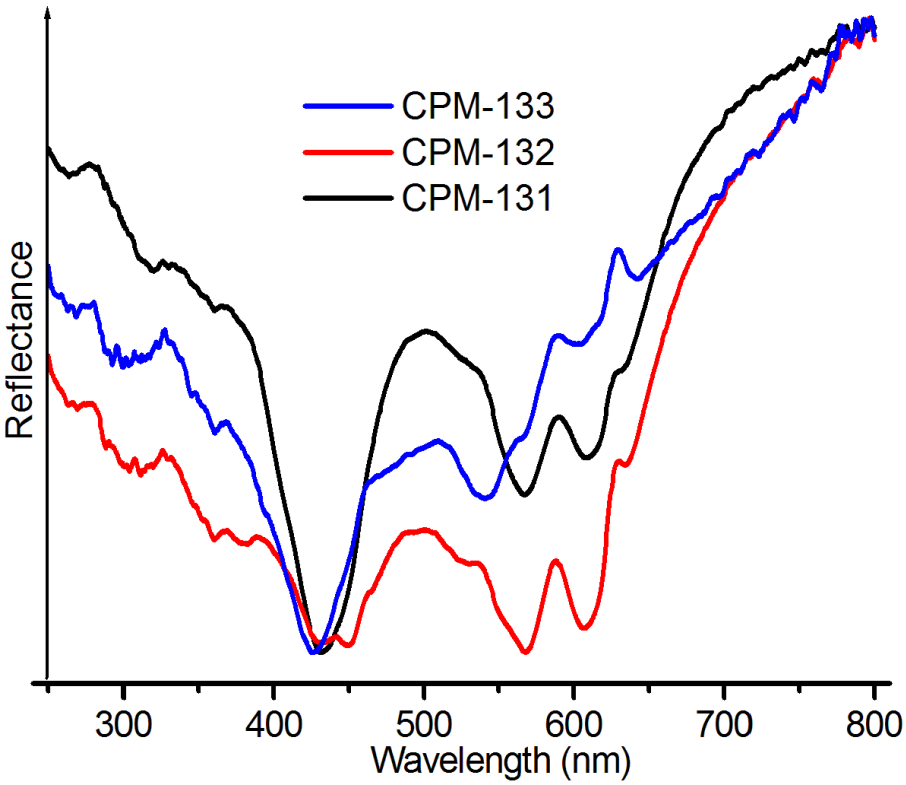

Fig. S22 Normalized solid-state diffuse reflectance spectra of the CPM-13X.

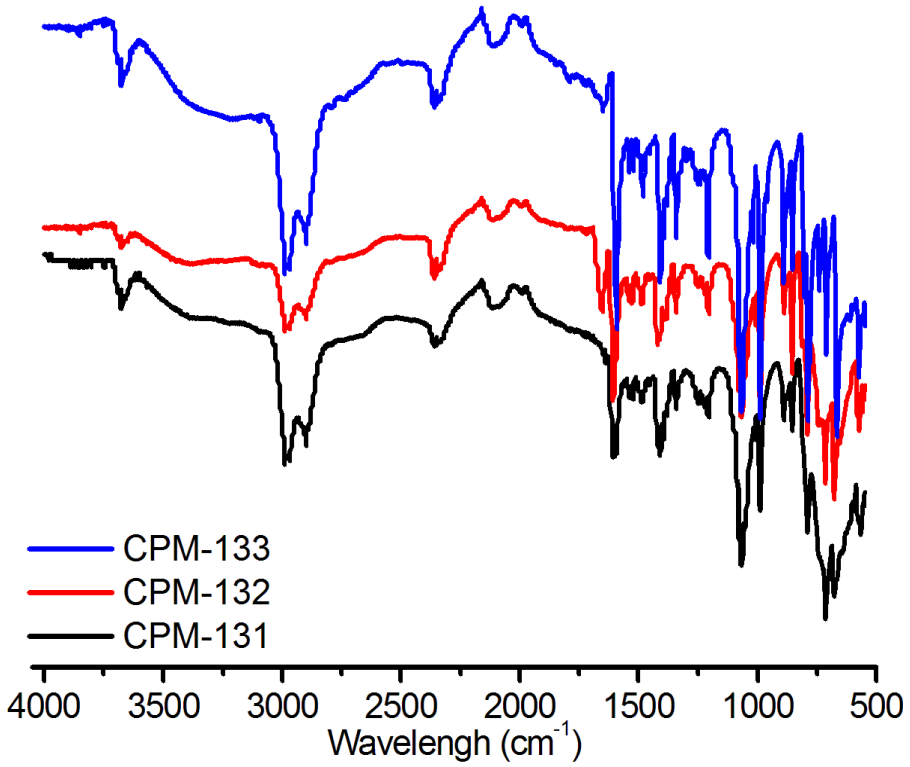

Fig. S23 FT-IR spectra of CPM-13X.

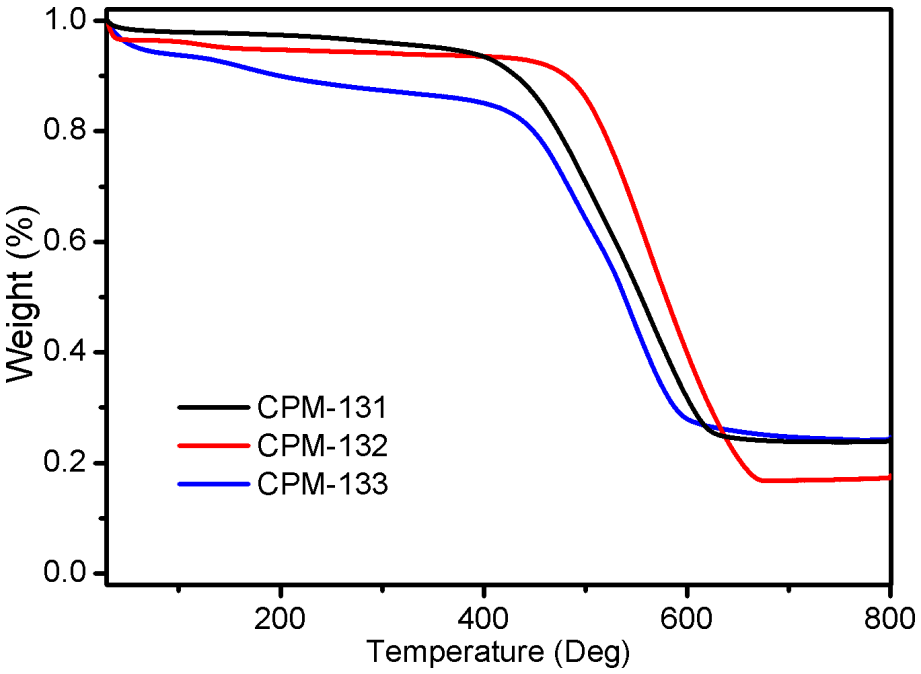

Fig. S24 TGA curves of CPM-13X.

8. Additional structural pictures

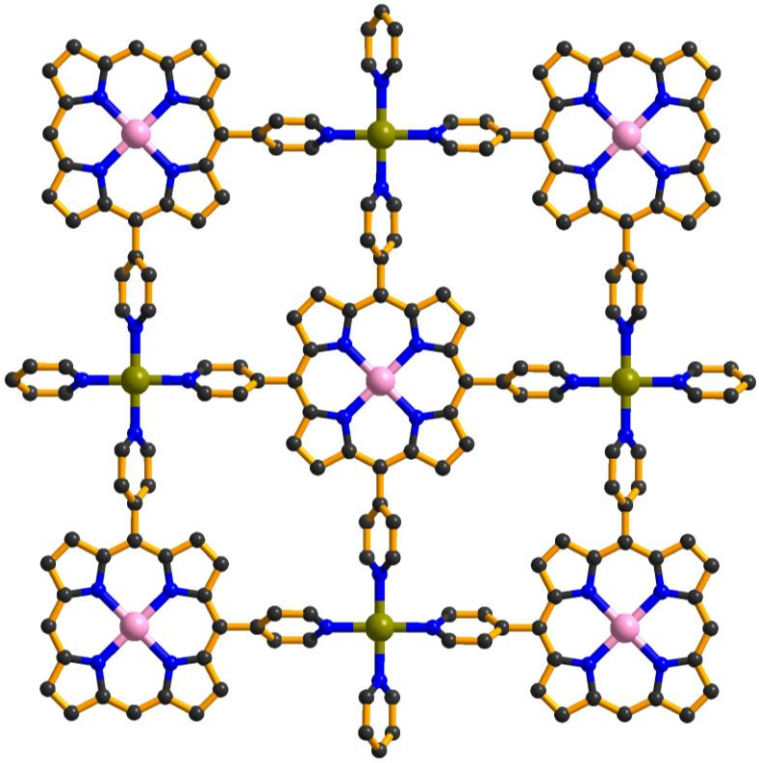

Fig. S25 Layer of [(TPyP-Fe)Zn]$_n$ in CPM-131.

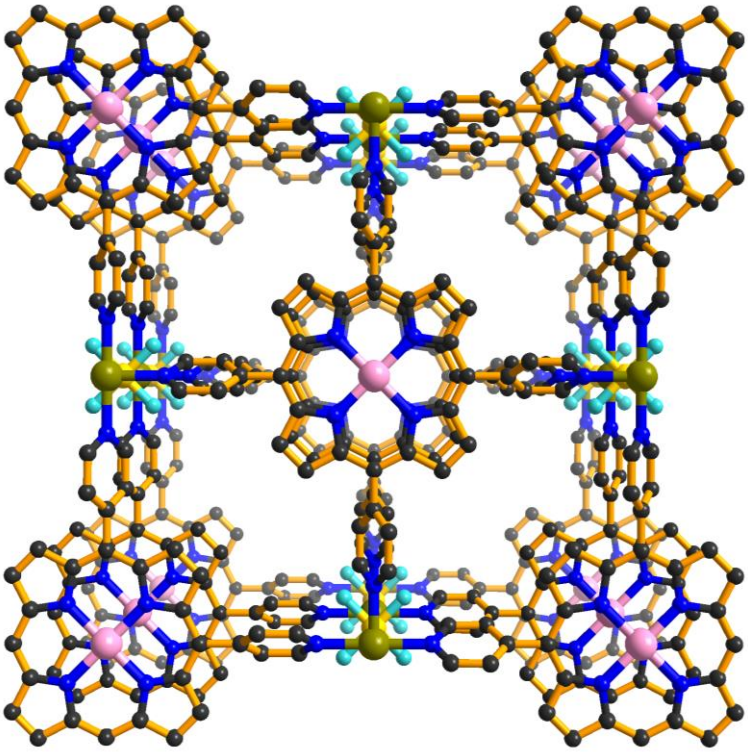

Fig. S26 Projection of structure of CPM-131 along *c* axis.

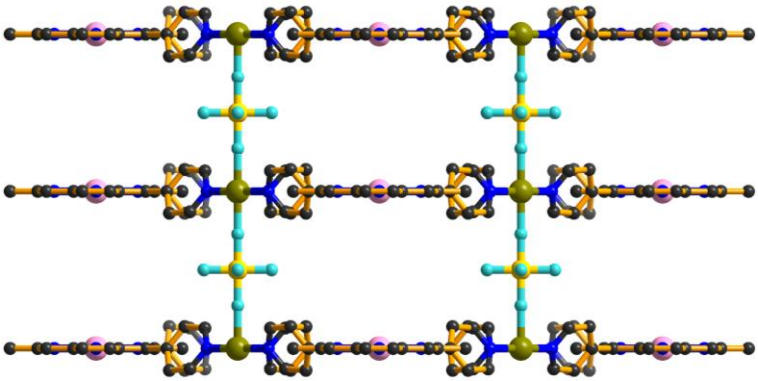

Fig. S27 Side view of 3D structure of CPM-131.

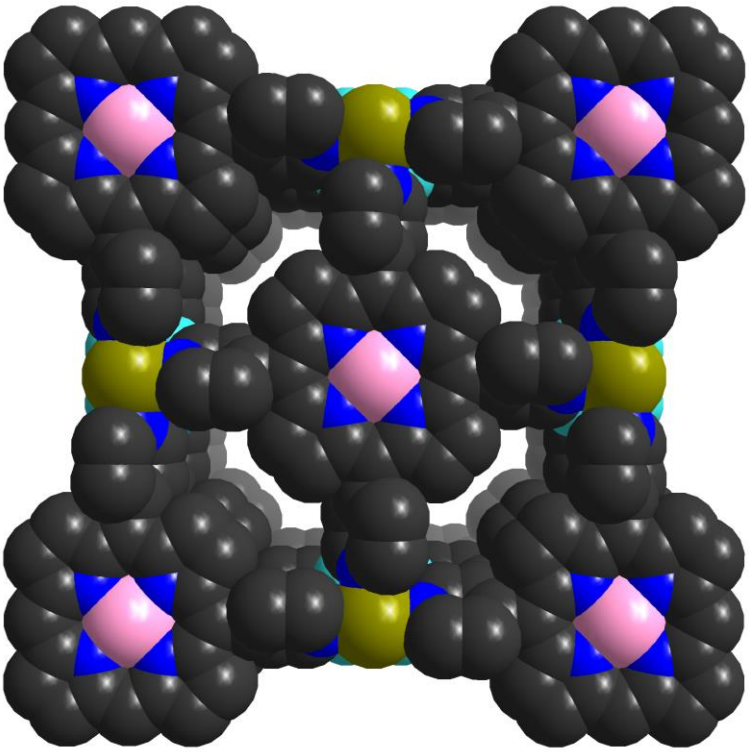

Fig. S28 Space-filling model of CPM-131 along *c* axis.

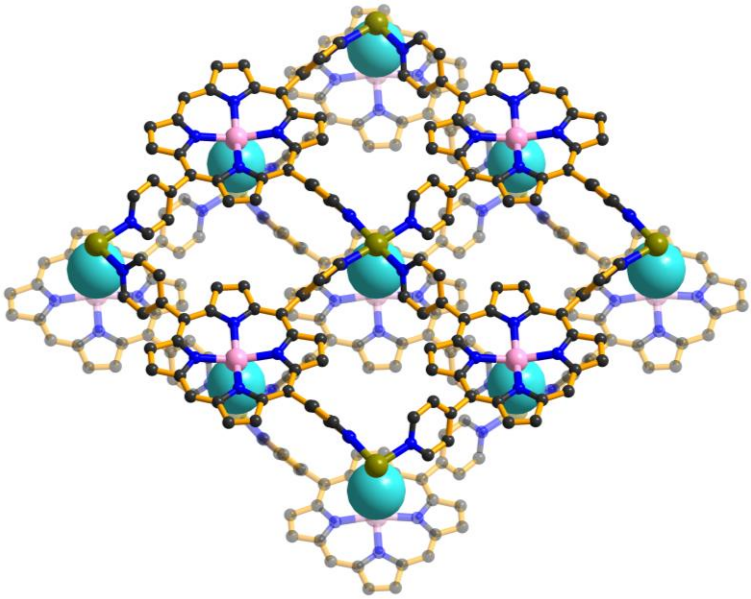

Fig. S29 Bi-layer (pillared by F^- ions) in CPM-132.

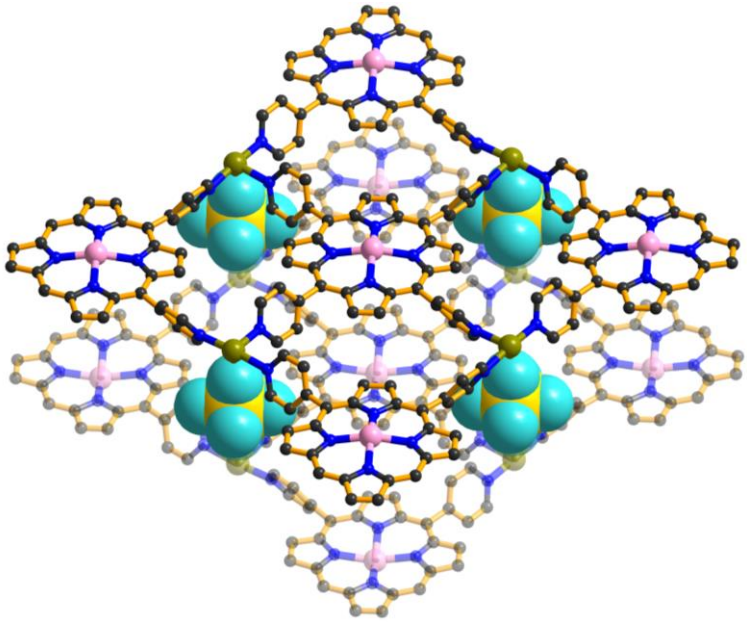

Fig. S30 Bi-layer (pillared by SiF_6^{2-} ions) in CPM-132.

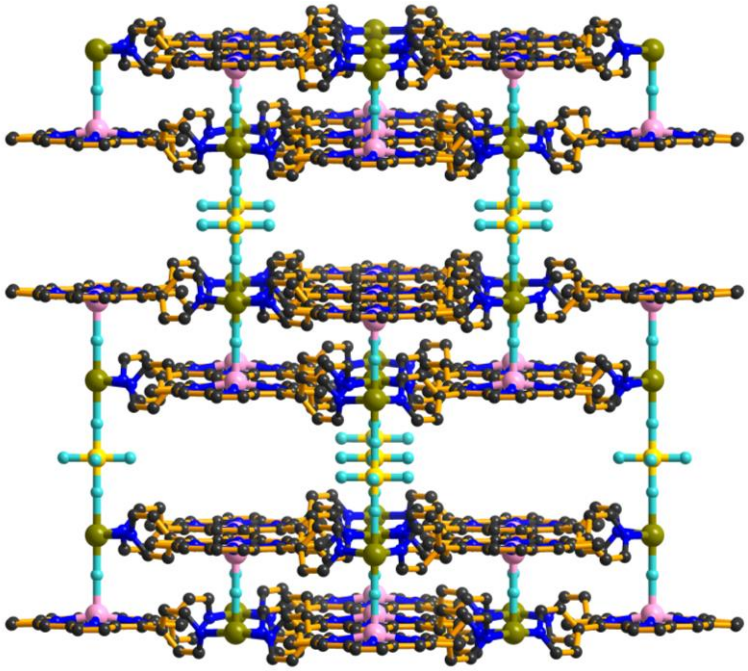

Fig. S31 Side view of the structure of CPM-132.

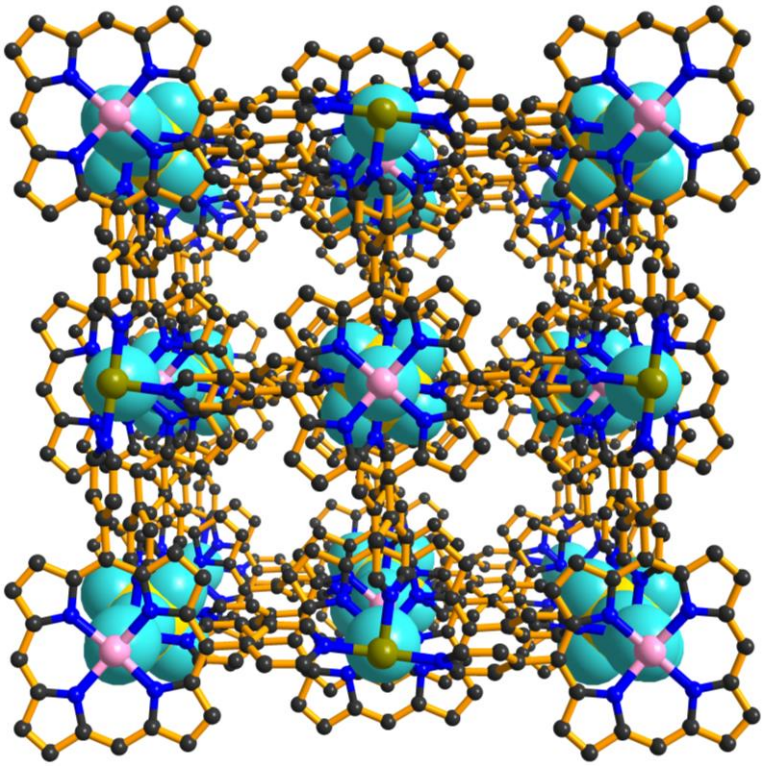

Fig. S32 Projection of structure of CPM-132 along *c* axis.

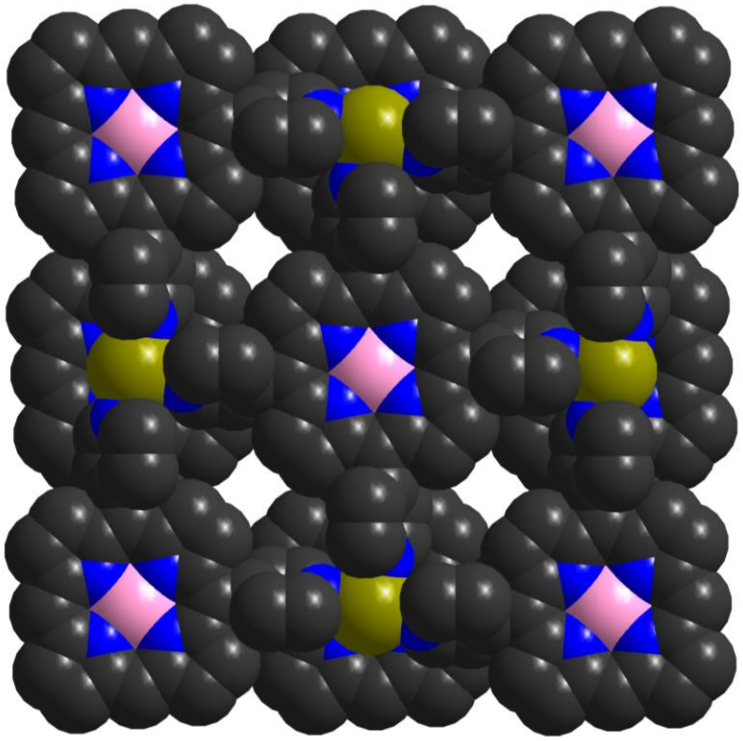

Fig. S33 Space-filling model of CPM-132 along *c* axis.

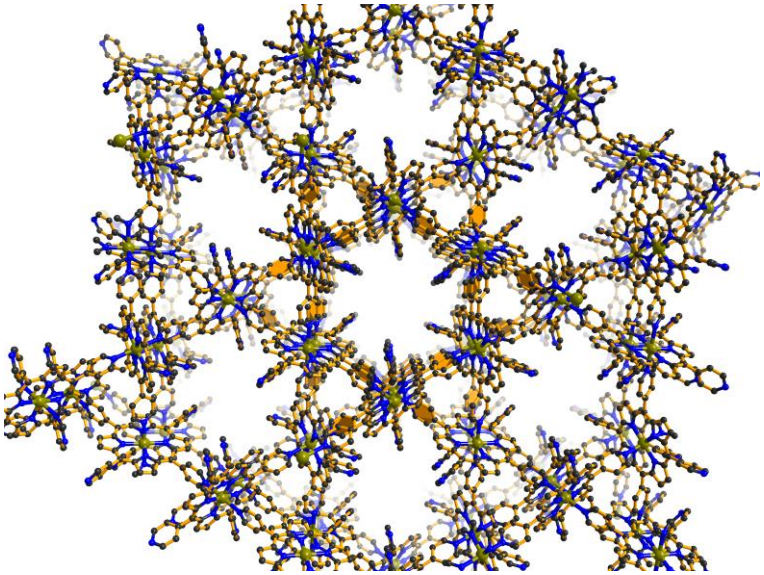

Fig. S34 Projection of the framework of CPM-133 along *c* axis.

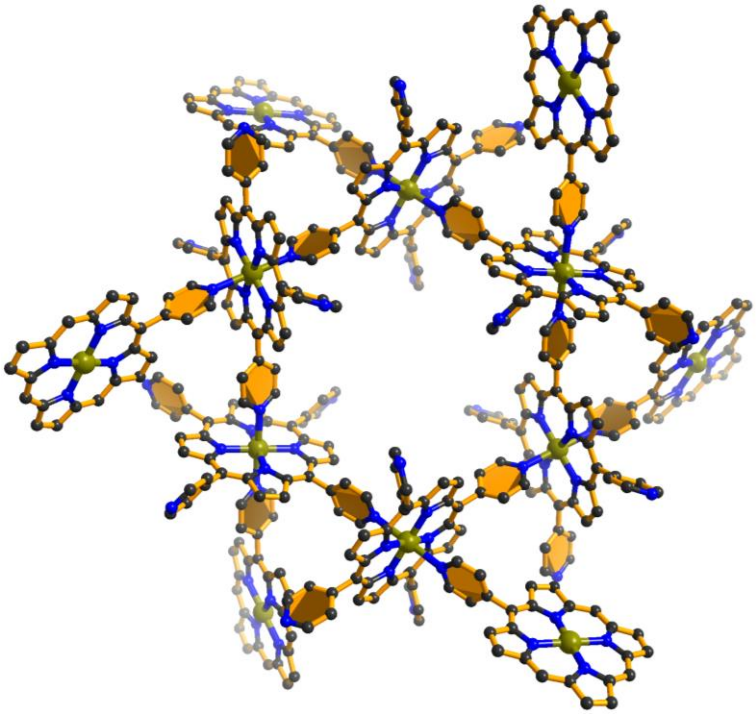

Fig. S35 Hexagonal channel of CPM-133 along *c* axis.

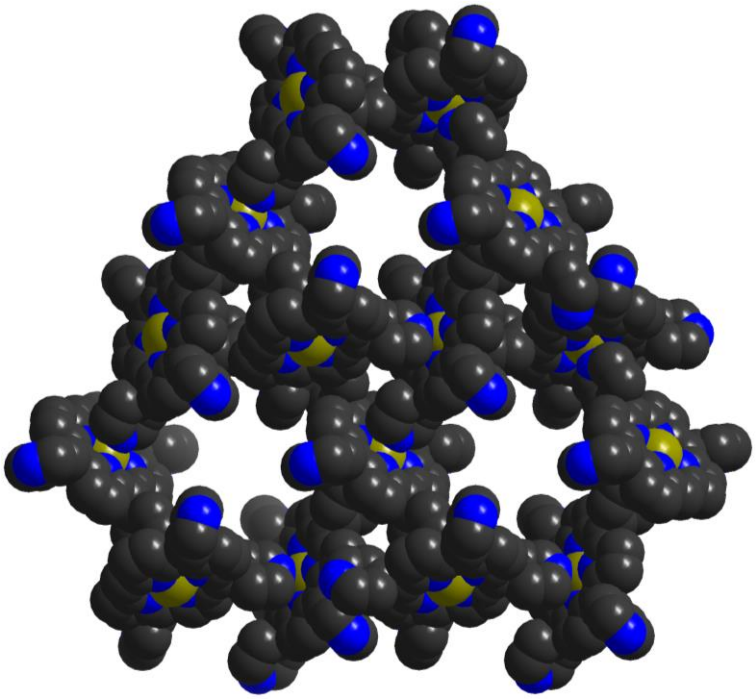

Fig. S36 Space-filling model of CPM-133 along *c* axis.

9. Gas sorptions

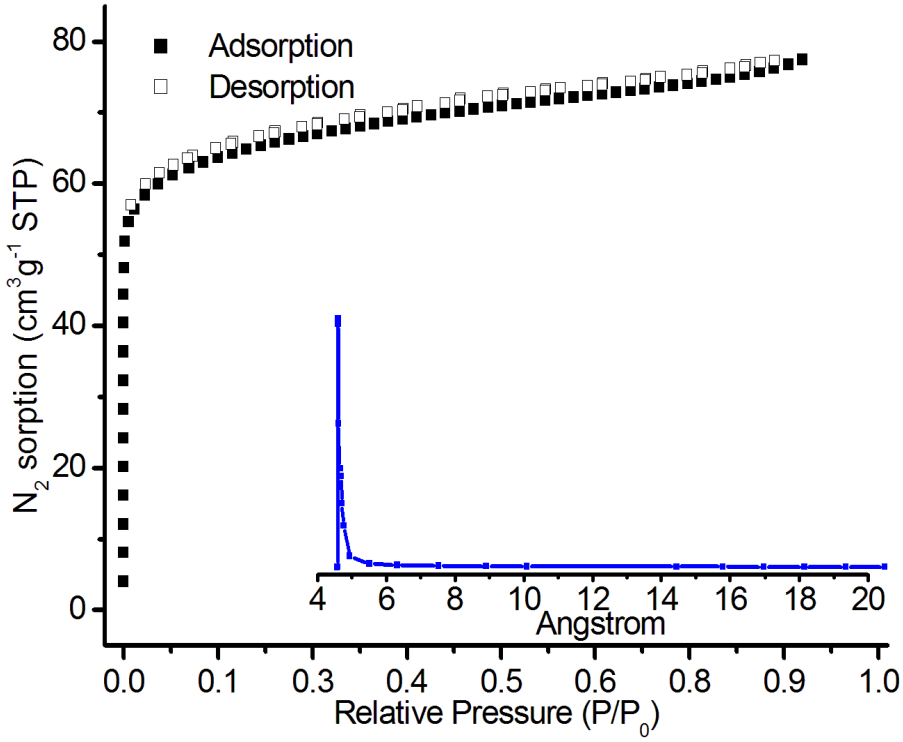

Fig. S37 N_2 adsorption-desorption isotherms with inset of pore size distribution (using Horvath-Kawazoe model) of CPM-131 at 77 K.

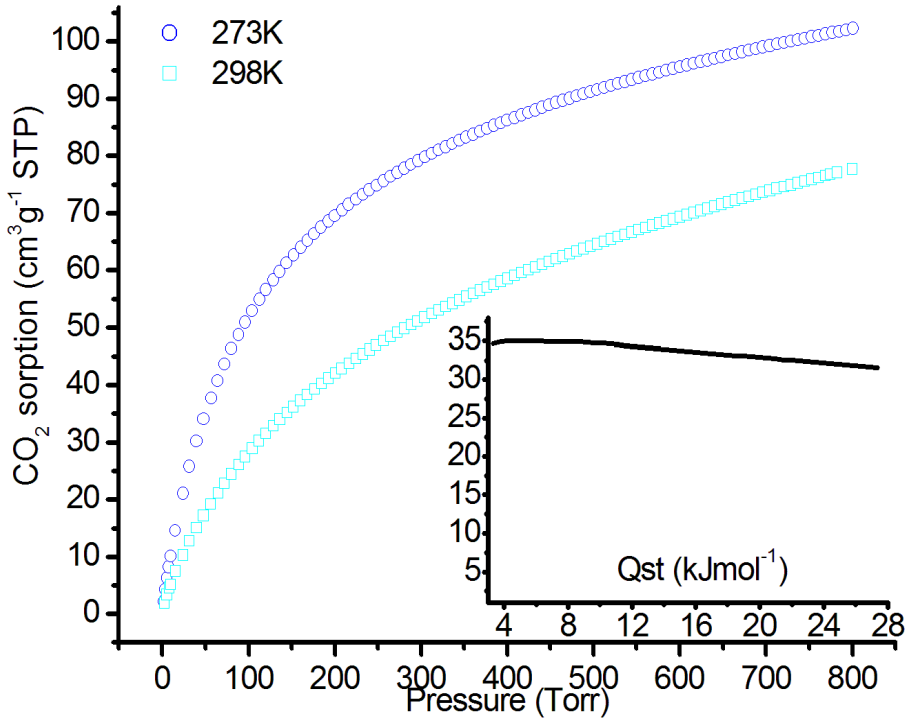

Fig. S38 CO_2 sorption with inset of Q_{st} of CPM-131.

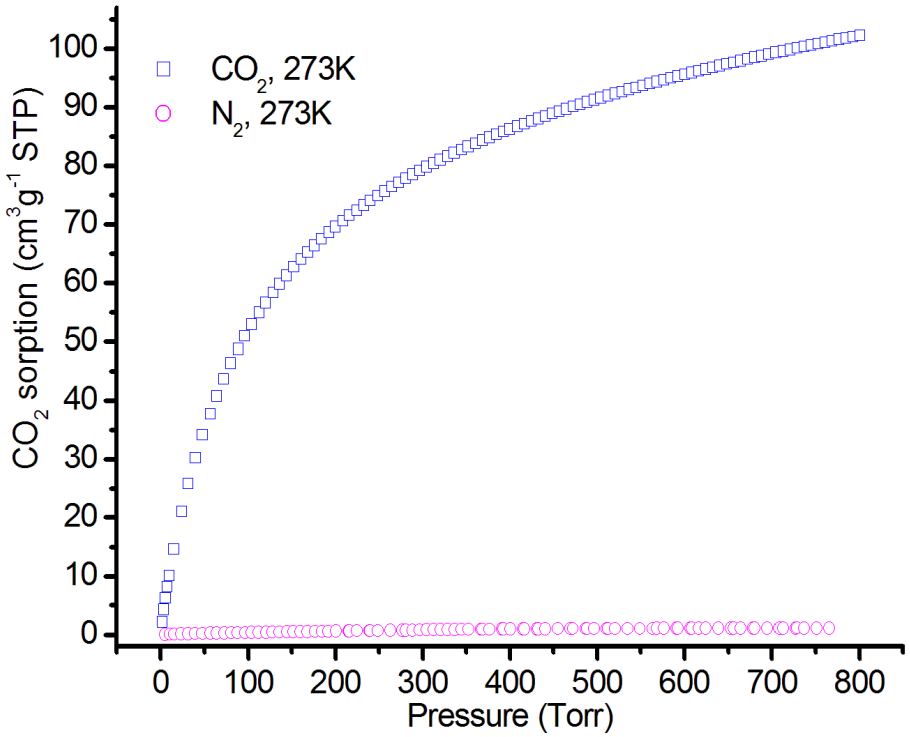

Fig. S39 CO_2 and N_2 adsorption of CPM-131 at 273 K.

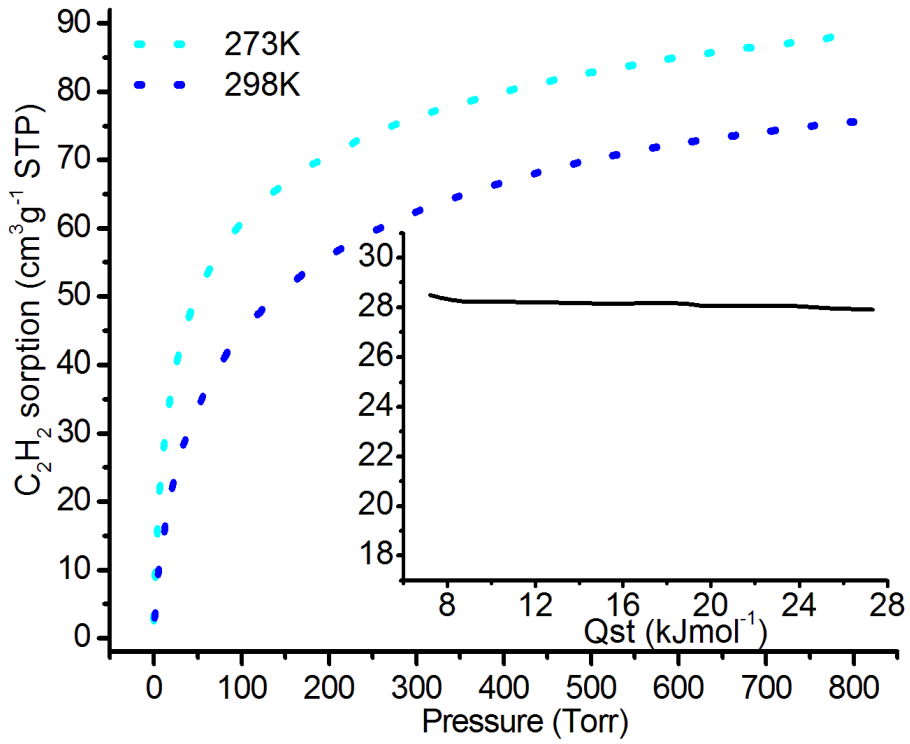

Fig. S40 C_2H_2 sorption with inset of Q_{st} of CPM-131.

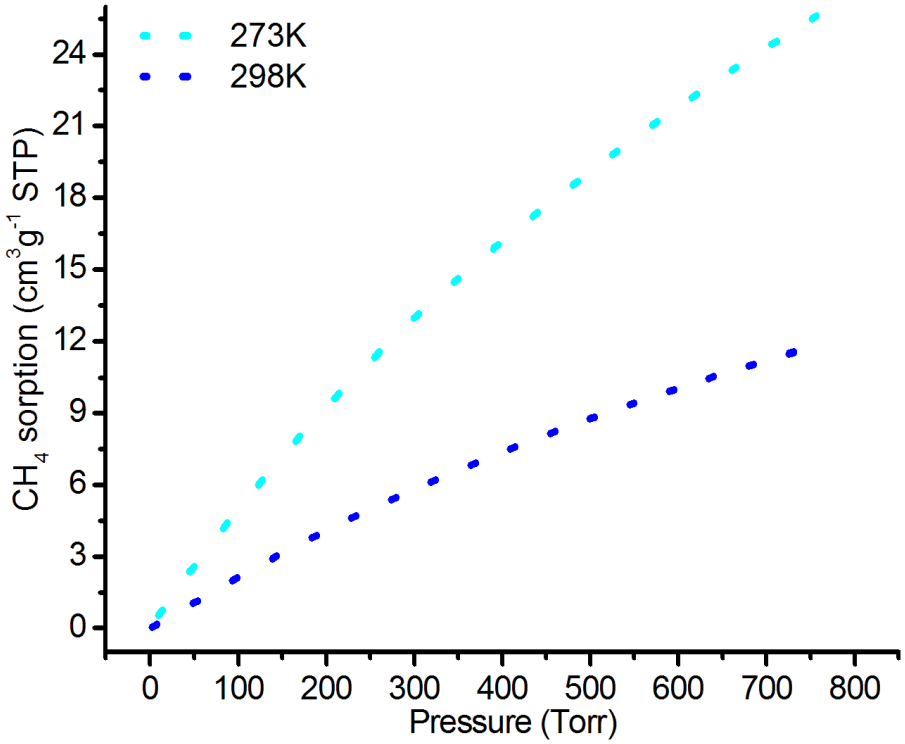

Fig. S41 CH_4 sorption of CPM-131.

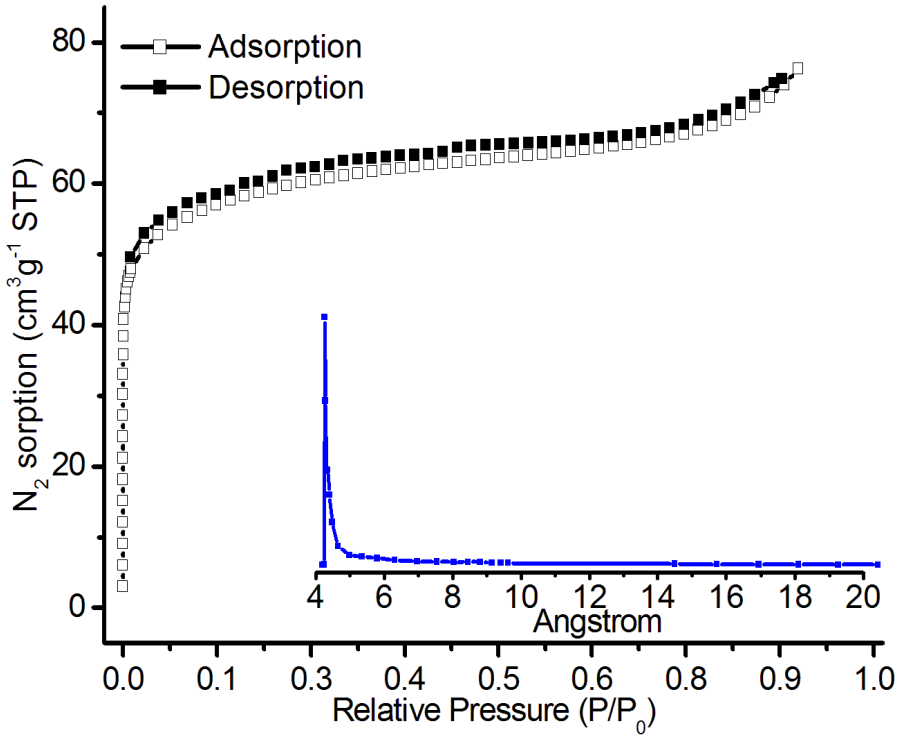

Fig. S42 N_2 adsorption-desorption isotherms with inset of pore size distribution (using Horvath-Kawazoe model) of CPM-132 at 77 K.

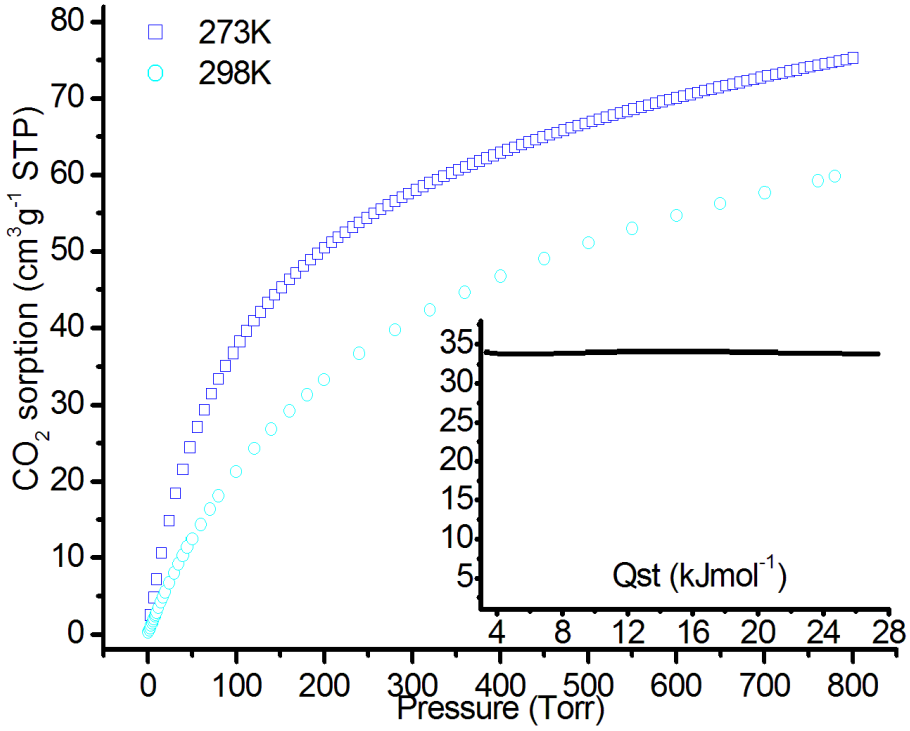

Fig. S43 CO_2 sorption with inset of Q_{st} of CPM-132.

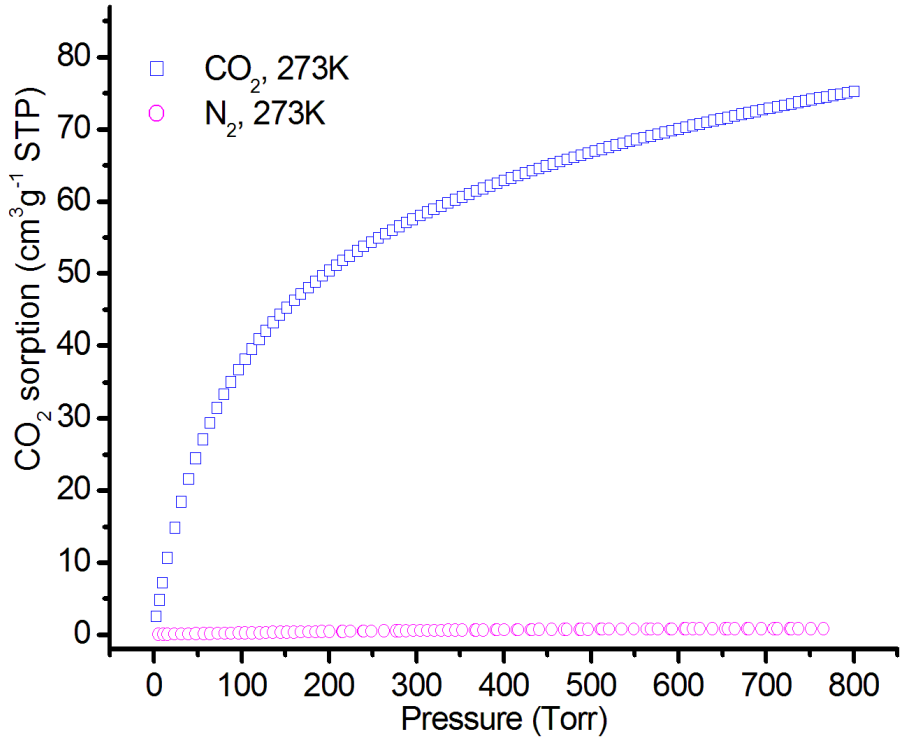

Fig. S44 CO_2 and N_2 adsorption of CPM-132 at 273 K.

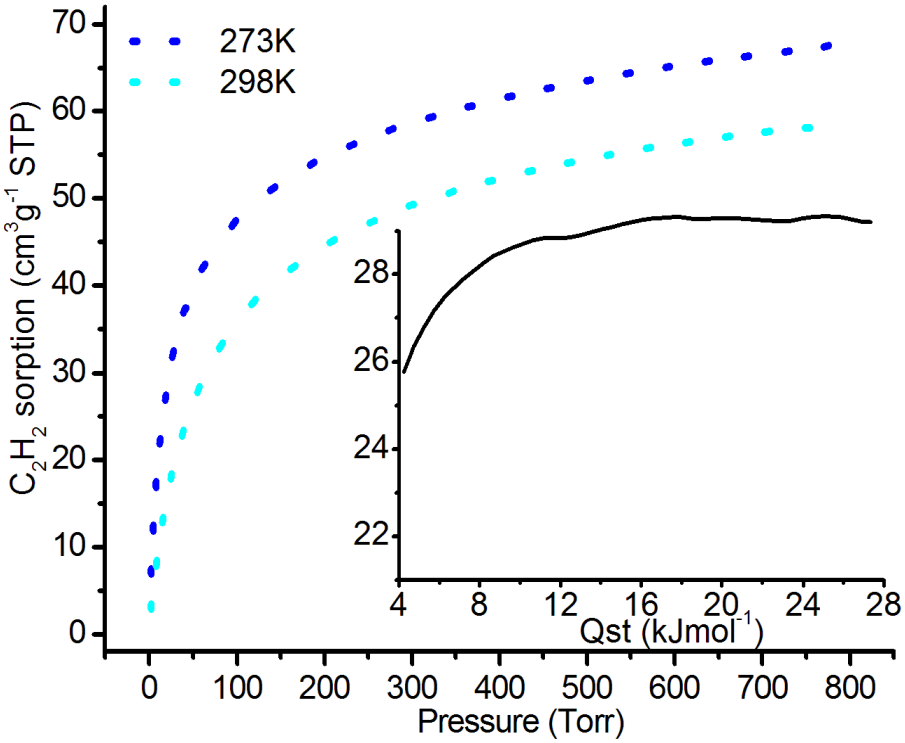

Fig. S45 C_2H_2 sorption with inset of Q_{st} of CPM-132.

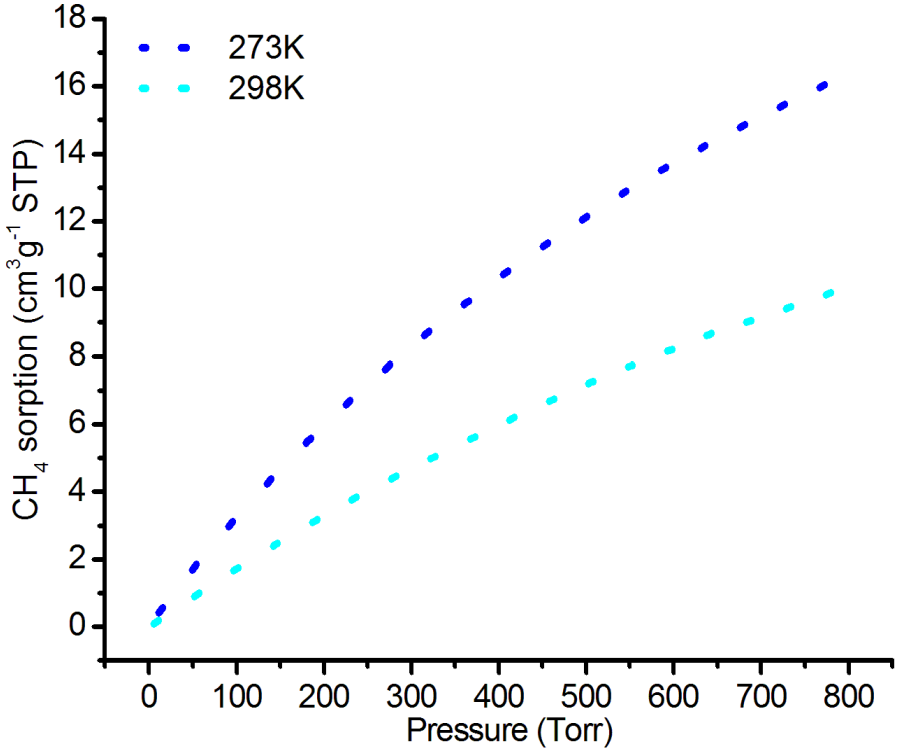

Fig. S46 CH_4 sorption of CPM-132.

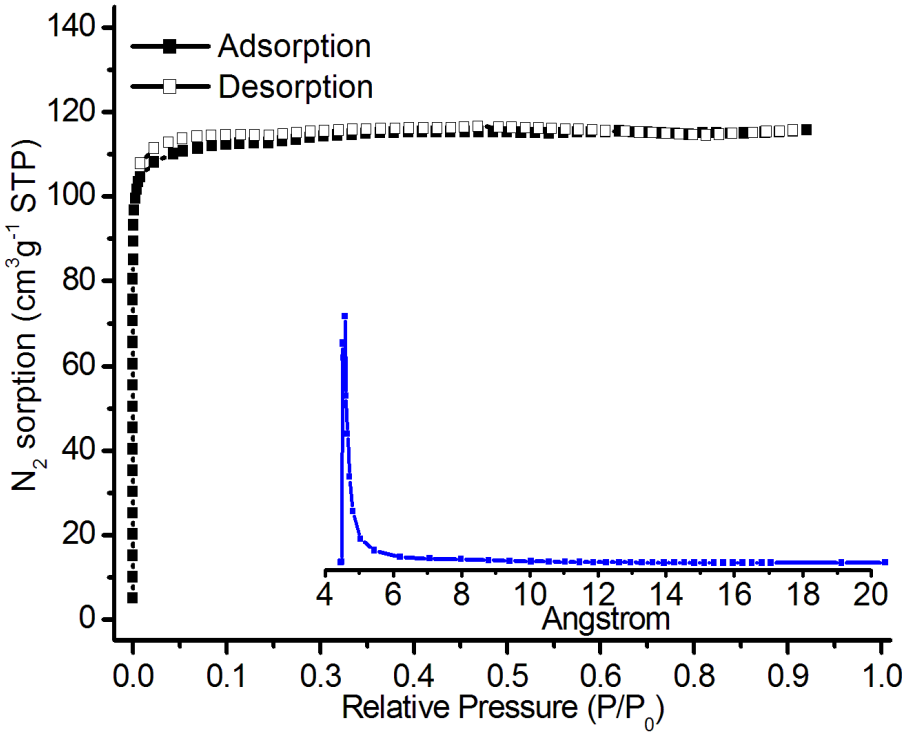

Fig. S47 N_2 adsorption-desorption isotherms with inset of pore size distribution (using Horvath-Kawazoe model) of CPM-133 at 77 K.

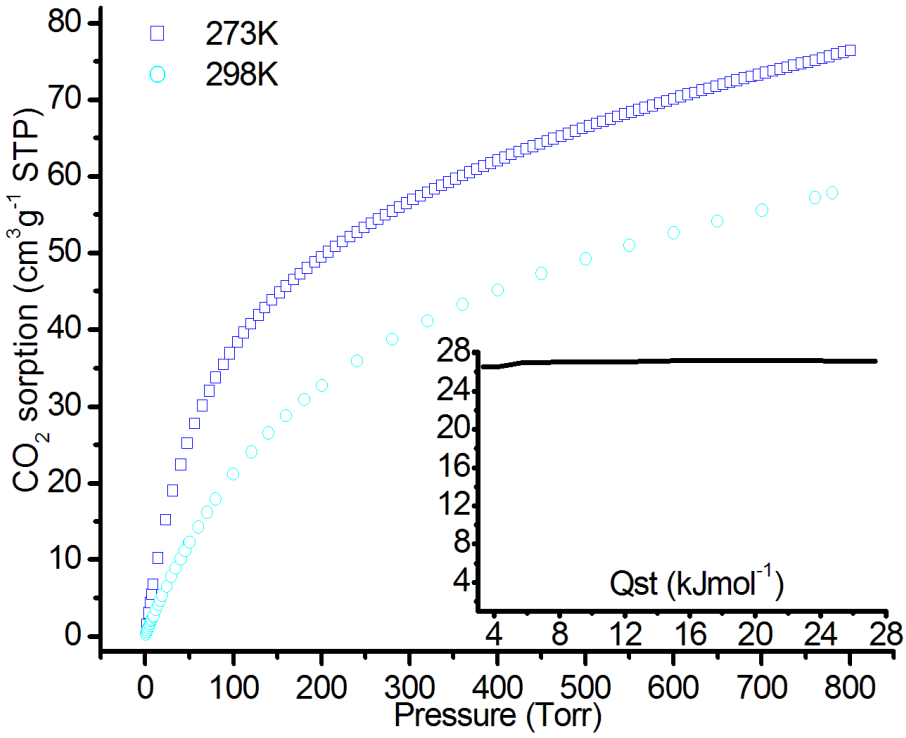

Fig. S48 CO_2 sorption with inset of Q_{st} of CPM-133.

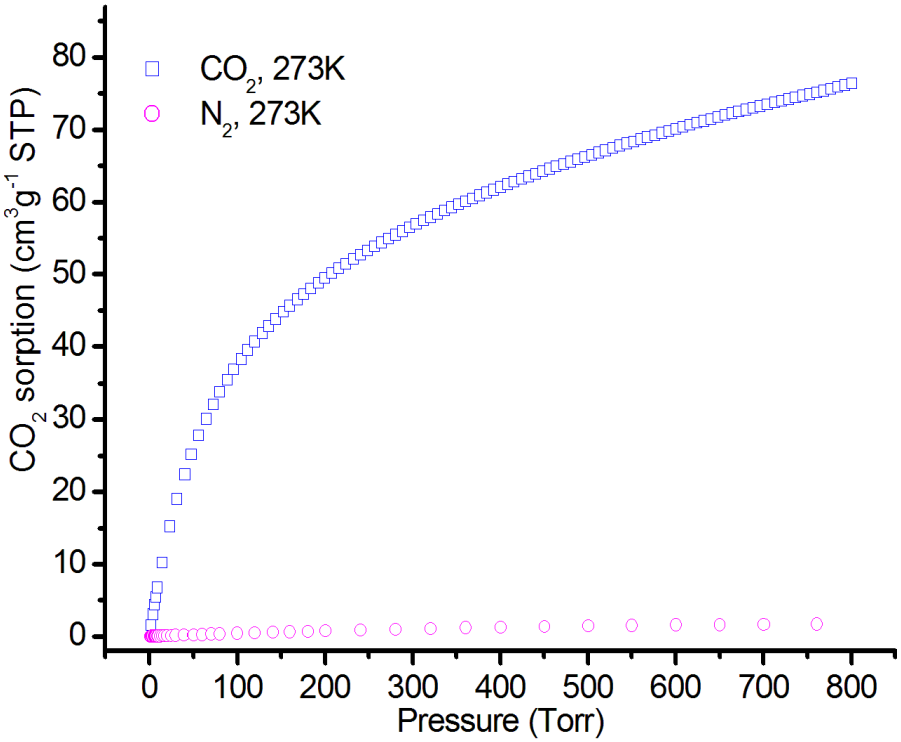

Fig. S49 CO_2 and N_2 adsorption of CPM-133 at 273 K.

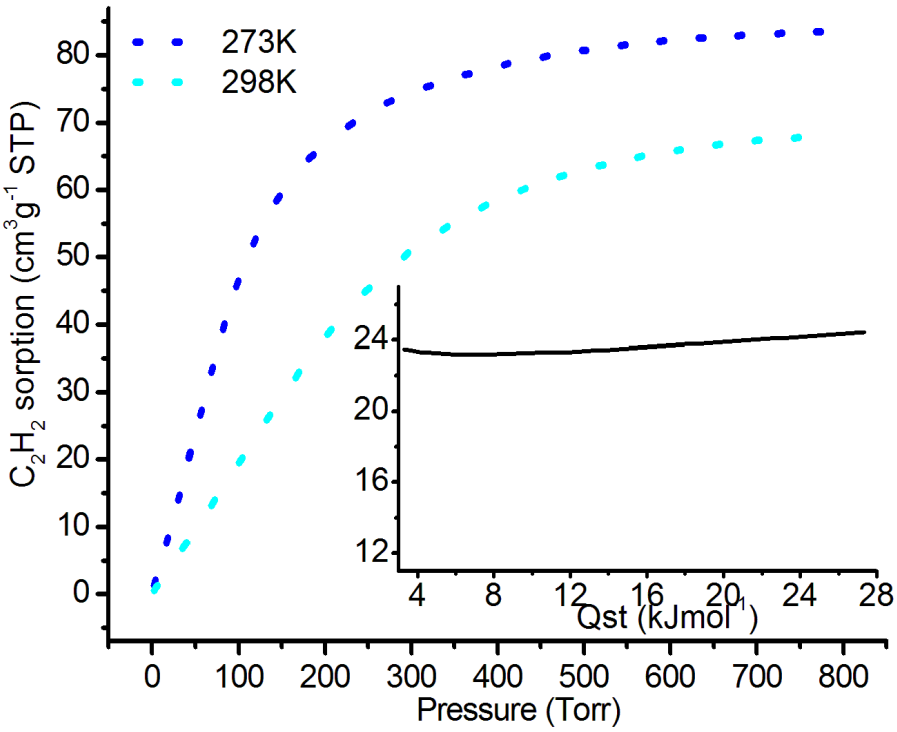

Fig. S50 C_2H_2 sorption with inset of Q_{st} of CPM-133.

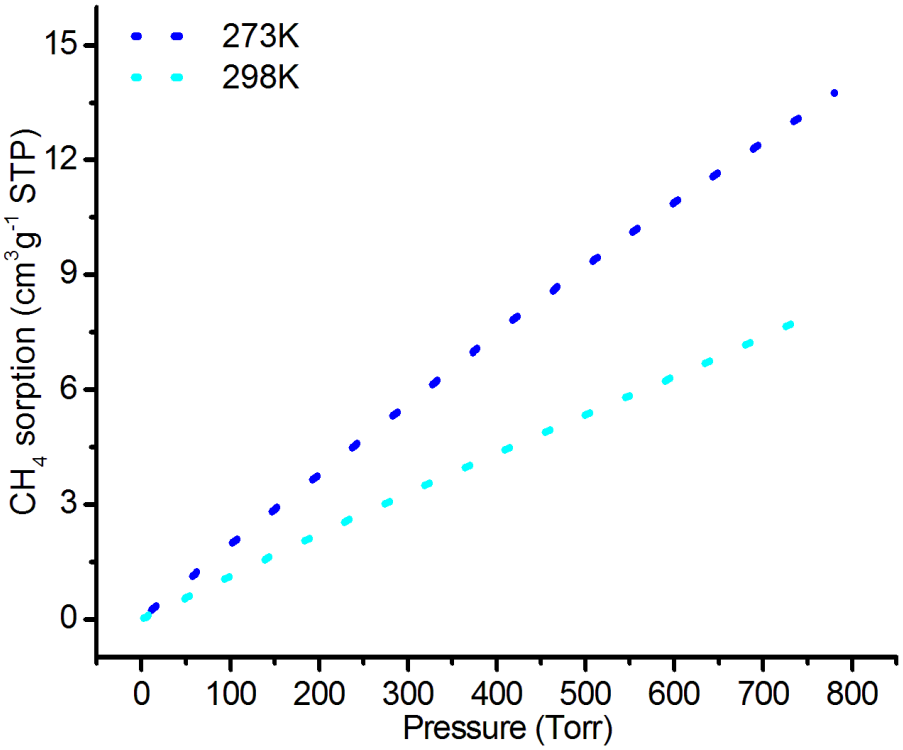

Fig. S51 CH_4 sorption of CPM-133.

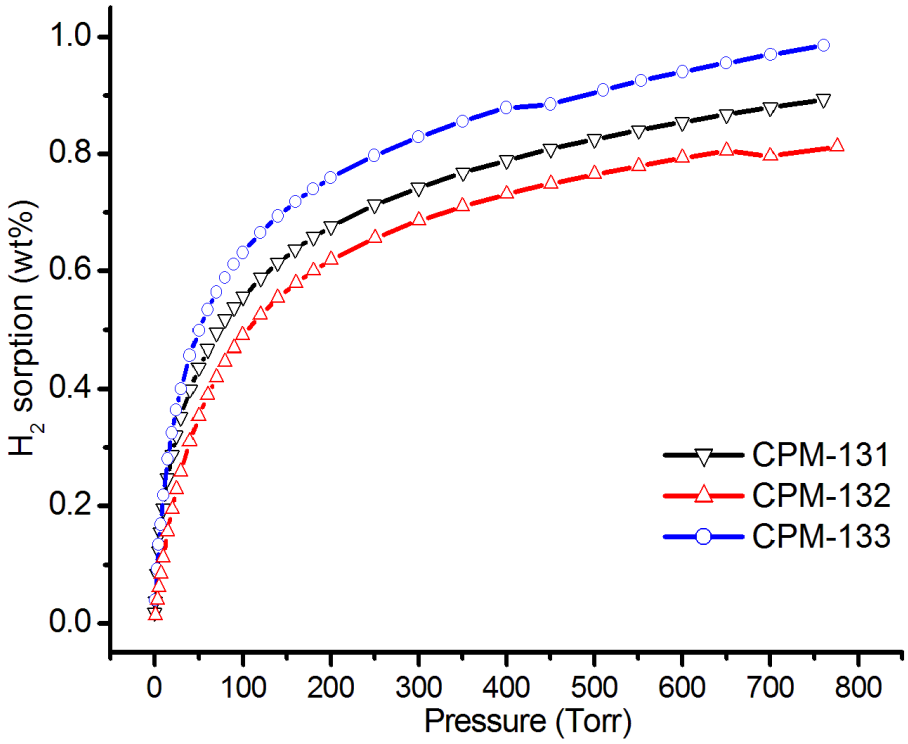

Fig. S52 H_2 sorption of CPM-13X at 77 K.

Table S2 A summary of porosity measurements.

Code	Framework Composition	Topology	S.A.	CO_2^{α}	CO_2^{β}	N_2^{α}	CH_4^{α}	Selectivity$^{\gamma}$	Pore Size	Q_{st}
CPM-131	$[(TPyP\text{-}Fe)Zn(SiF_6)]_n$	**fsc**	226/286	101/55	76/31	1.0/0.39	13/2.9	1211[108]	4.3 Å	35
CPM-132	$[(TPyP\text{-}Zn)_2F_2Zn_2(SiF_6)]_n$	**fsx**	204/258	74/40	59/23	0.8/0.25	8/2.8	942[104]	4.3 Å	34
CPM-133	$[TPyP\text{-}Cu]_n$	**nbo**	390/490	75/39	59/22	1.7/0.45	13/2.2	523[99]	4.8 Å	27

S.A. = (BET/Langmuir) surface area (m^2g^{-1}), $^{\alpha}$uptake @ 1/0.15 bar (cm^3g^{-1}) at 273 K, $^{\beta}$uptake @ 1/0.15 bar (cm^3g^{-1}) at 298 K, $^{\gamma}$selectivity for CO_2:N_2 (10:90) [selectivity for CO_2:CH_4 (50:50)] at 0.01 bar (273 K) by IAST, Q_{st} for CO_2 ($kJmol^{-1}$).

10. Pyrolysis of CPM-13X (to CPM-13X/C)

The pyrolysis reaction of CPM-13X to CPM-13X/C was carried out in quartz tubes (with two open ends) in tube furnace under Ar atmosphere. The CPM-13X samples were heated from the room temperature to 700, or 800, or 900 or 1000 ℃ with a heating rate of 4 ℃·min^{-1}, then kept the temperature for 4 hr in Ar gas, respectively. The carbonization products were denoted to CPM-13X/C-700, CPM-13X/C-800, CPM-13X/C-900 and CPM-13X/C-1000. FT-IR: ν = 3680 (m), 2990 (s), 2360 (s), 1390 (m), 1250 (m), 1070 (s), 879 (m) cm^{-1} for CPM-131/C; ν = 3680 (m), 2990 (s), 2360 (s), 1390 (m), 1070 (s) cm^{-1} for CPM-132/C; ν = 3680 (m), 2990 (s), 2340 (m), 1390 (m), 1230 (m), 1070 (s), 879 (w) cm^{-1} for CPM-133/C.

11. Characterization of CPM-13X/C

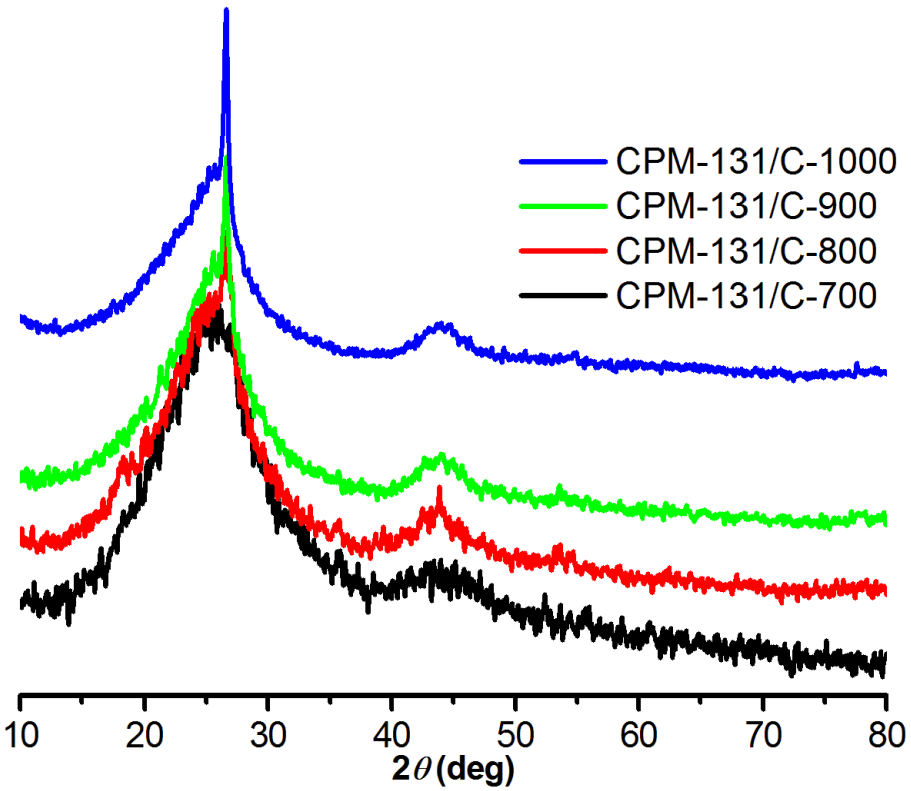

Fig. S53 PXRD patterns of CPM-131/C pyrolized at different temperature.

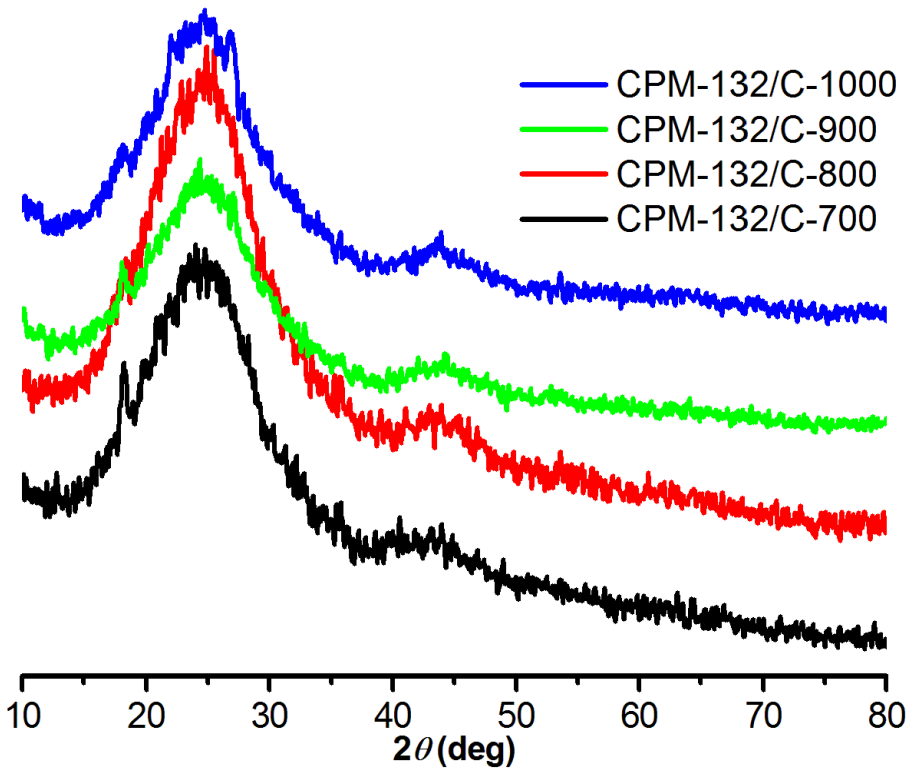

Fig. S54 PXRD patterns of CPM-132/C pyrolized at different temperature.

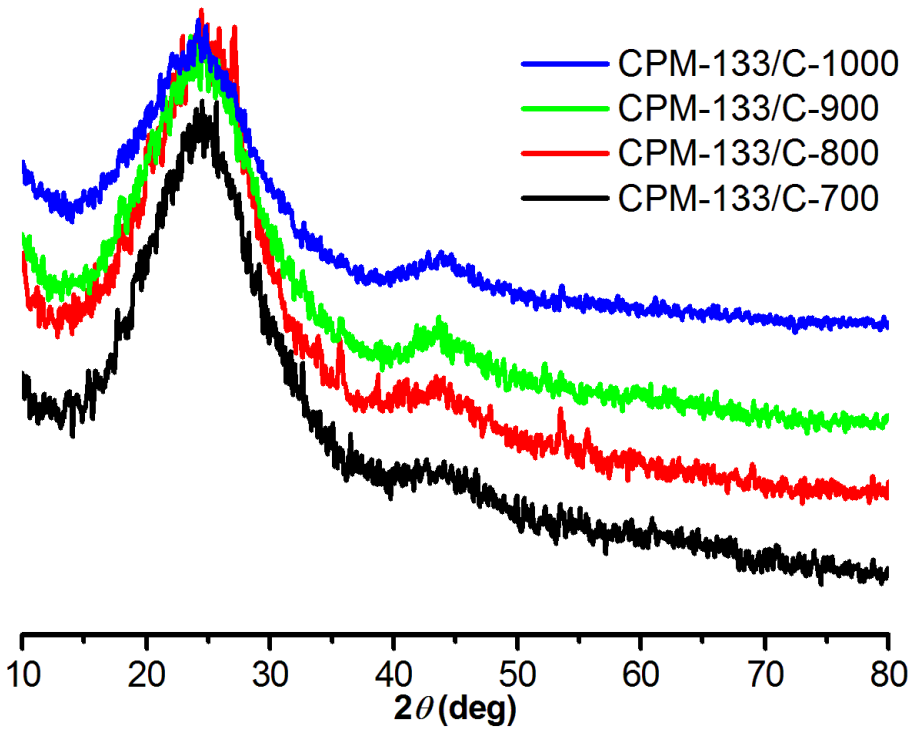

Fig. S55 PXRD patterns of CPM-133/C pyrolized at different temperature.

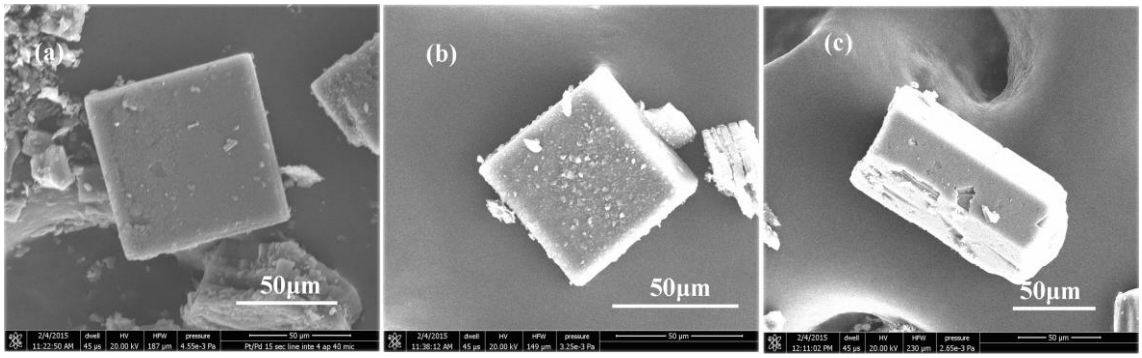

Fig. S56 SEM images of (a) CPM-131/C, (b) CPM-132/C, and (c) CPM-133/C.

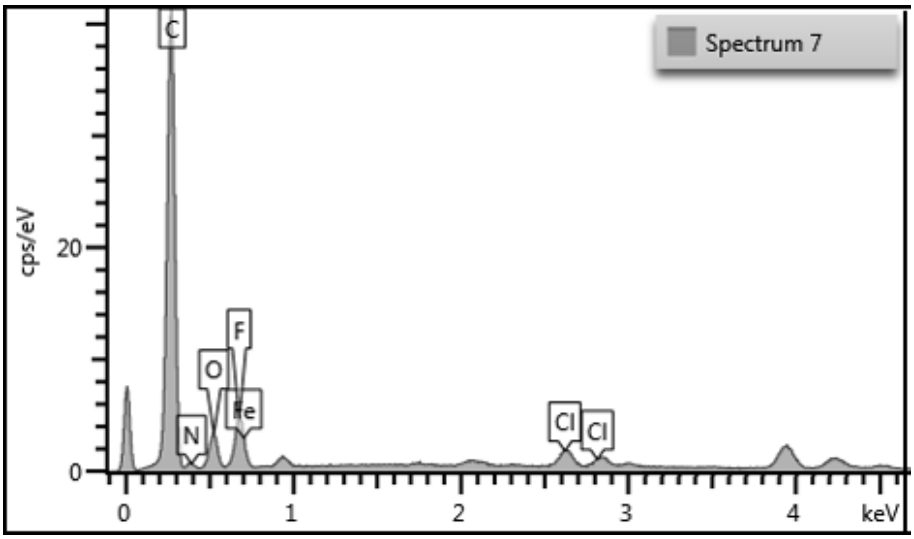

Fig. S57 EDX of CPM-131/C (coated with Pd/Pt).

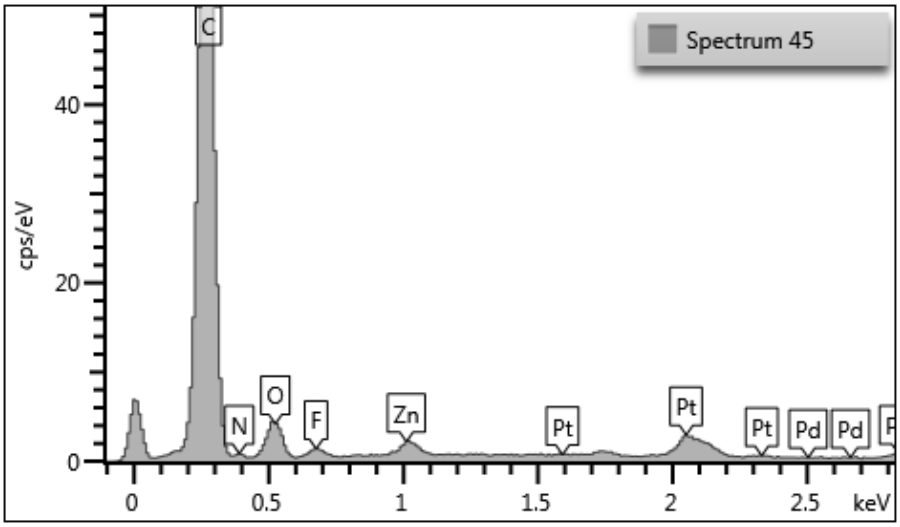

Fig. S58 EDX of CPM-132/C (coated with Pd/Pt).

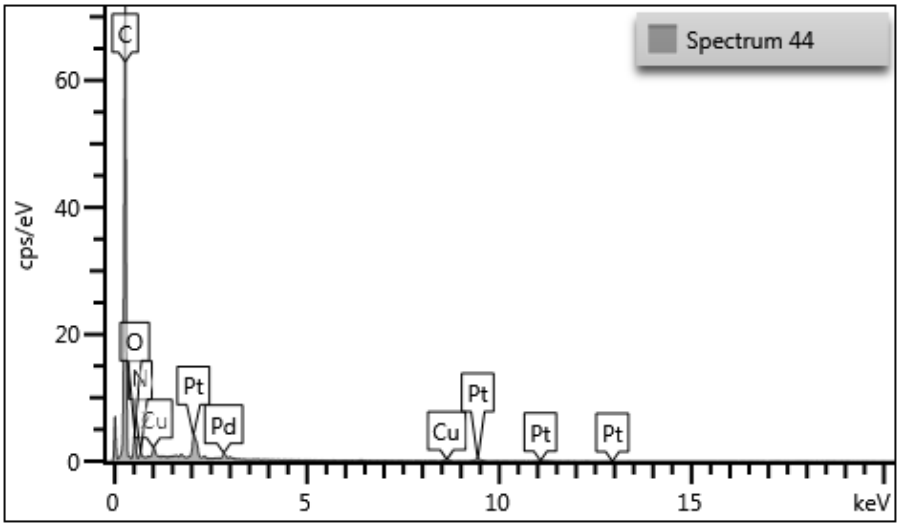

Fig. S59 EDX of CPM-133/C (coated with Pd/Pt).

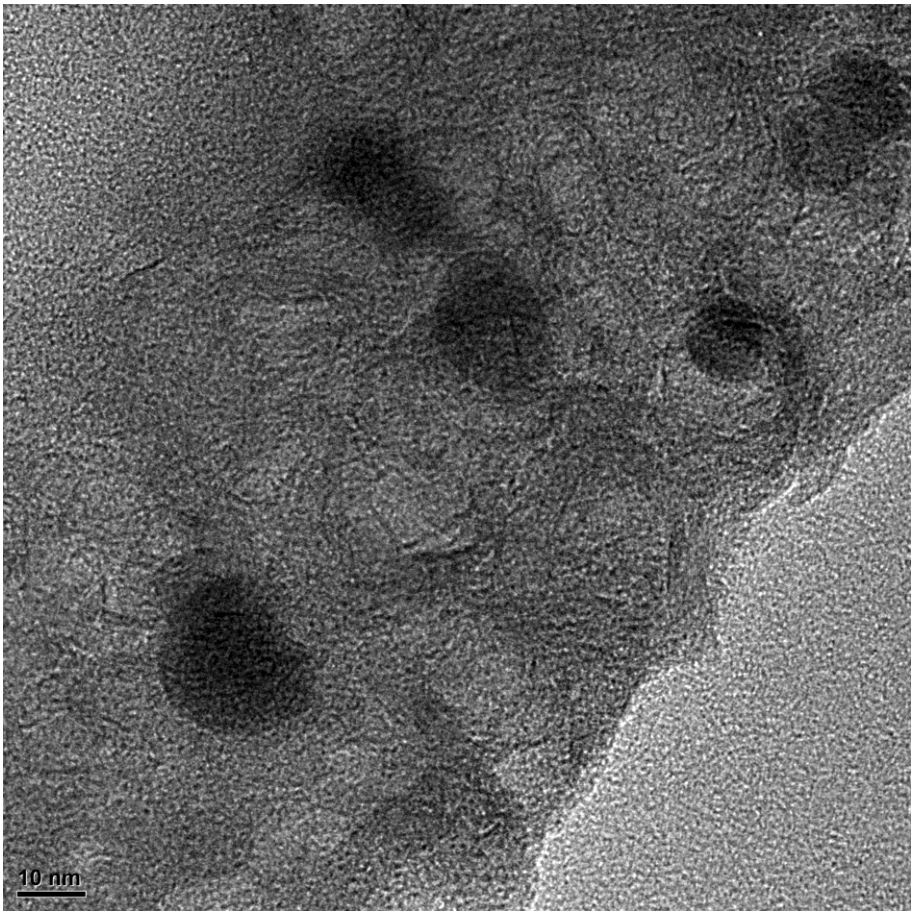

Fig. S60 TEM image of CPM-131/C.

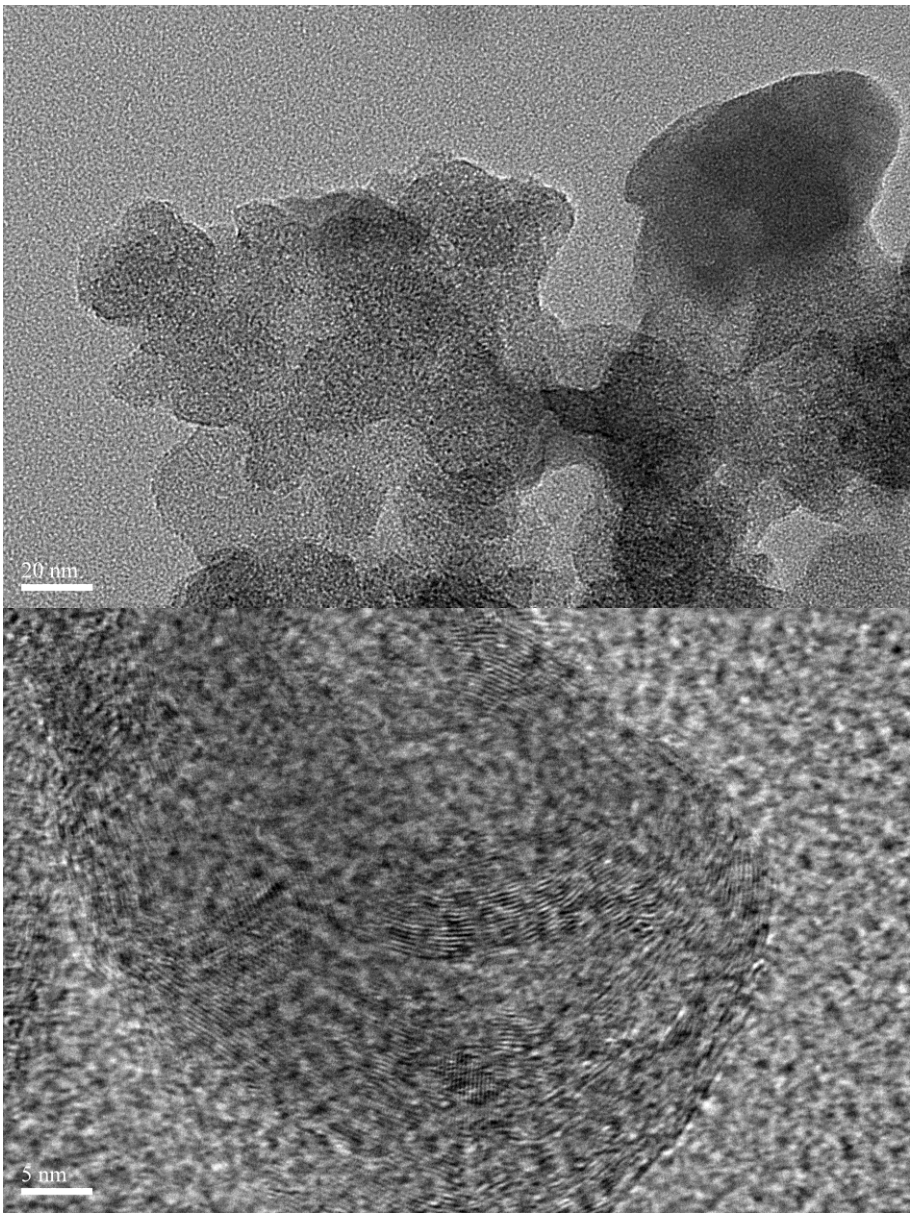

Fig. S61 TEM images of CPM-132/C.

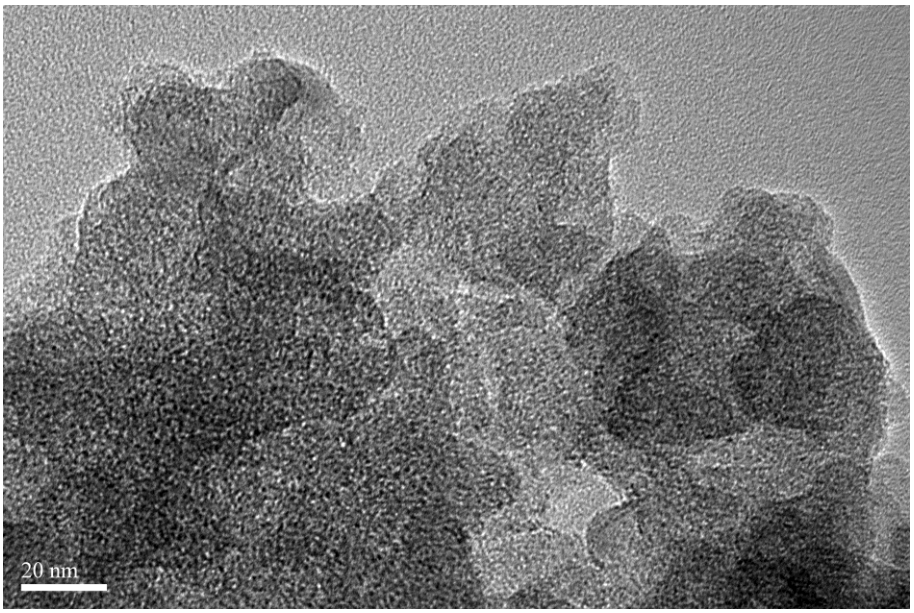

Fig. S62 TEM images of CPM-133/C.

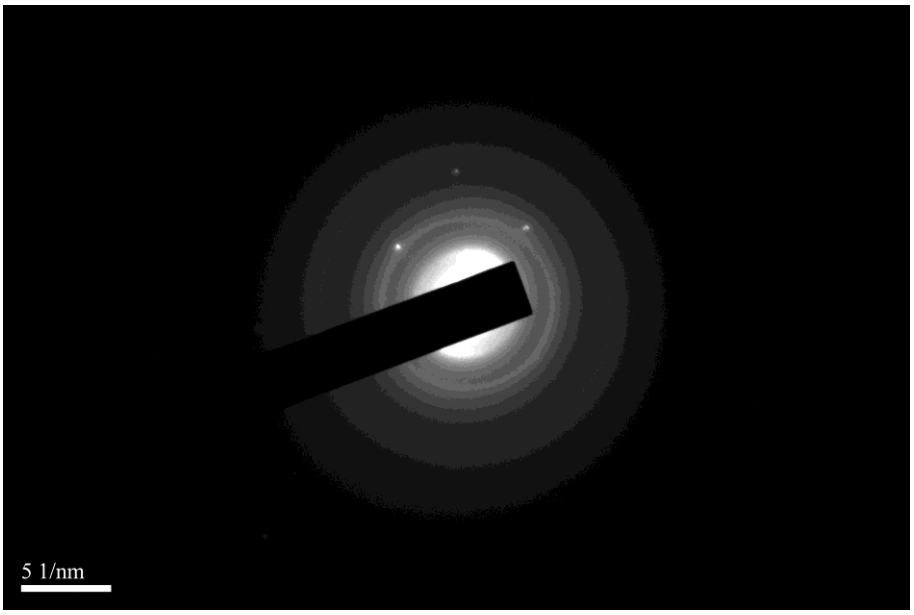

Fig. S63 SAED pattern of CPM-131/C.

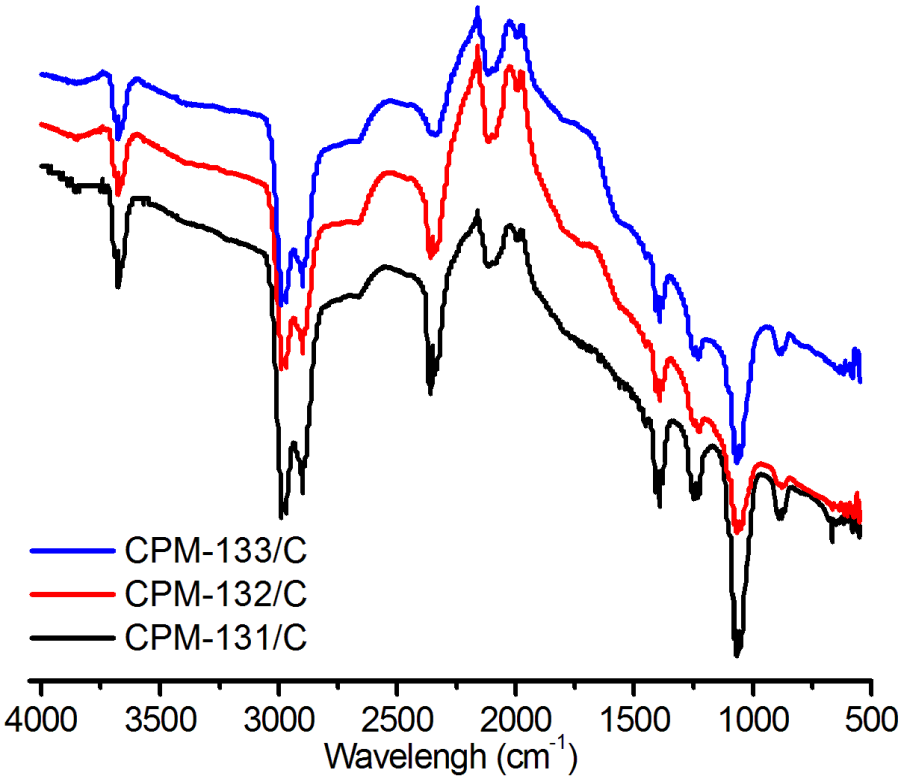

Fig. S64 FT-IR spectra of CPM-13X/C-700.

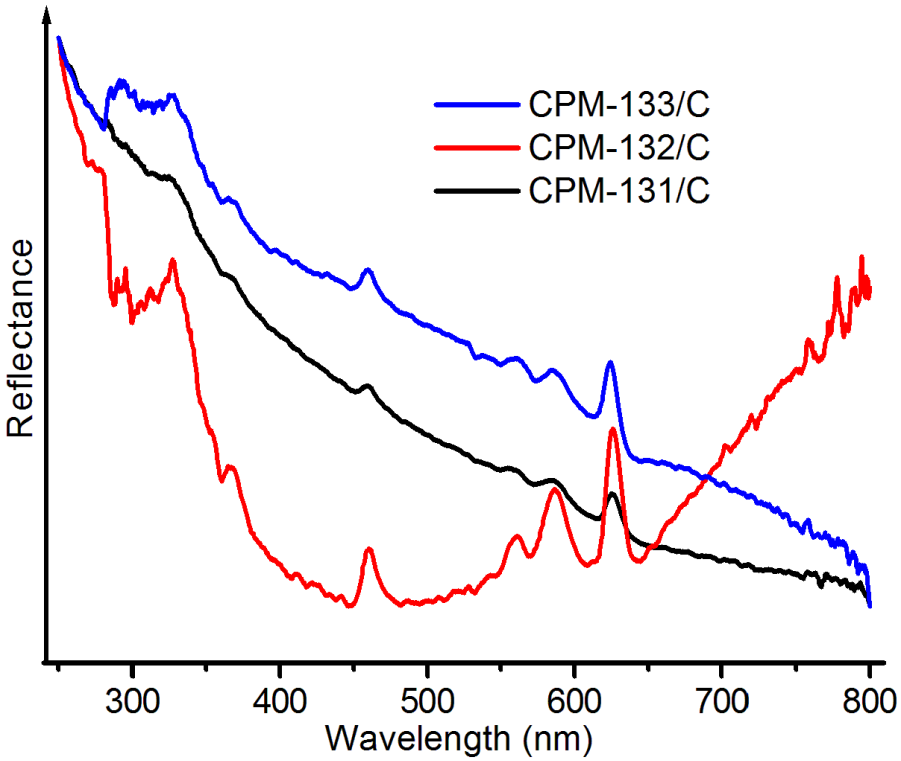

Fig. S65 Normalized solid-state diffuse reflectance spectra of CPM-13X/C-700.

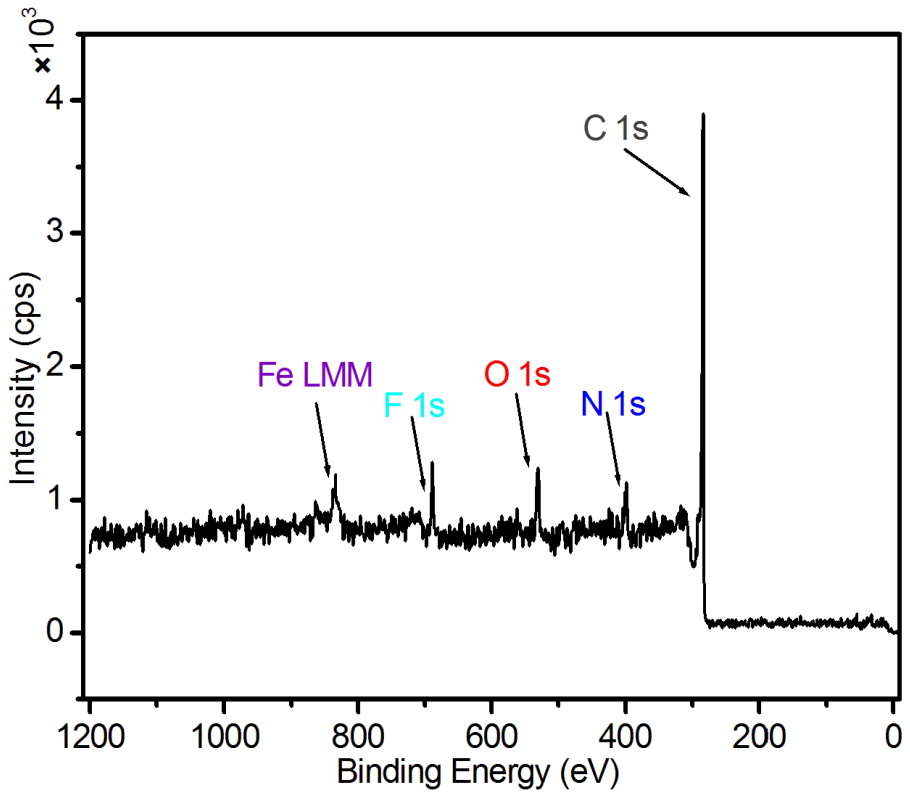

Fig. S66 XPS survey spectrum of CPM-131/C-700.

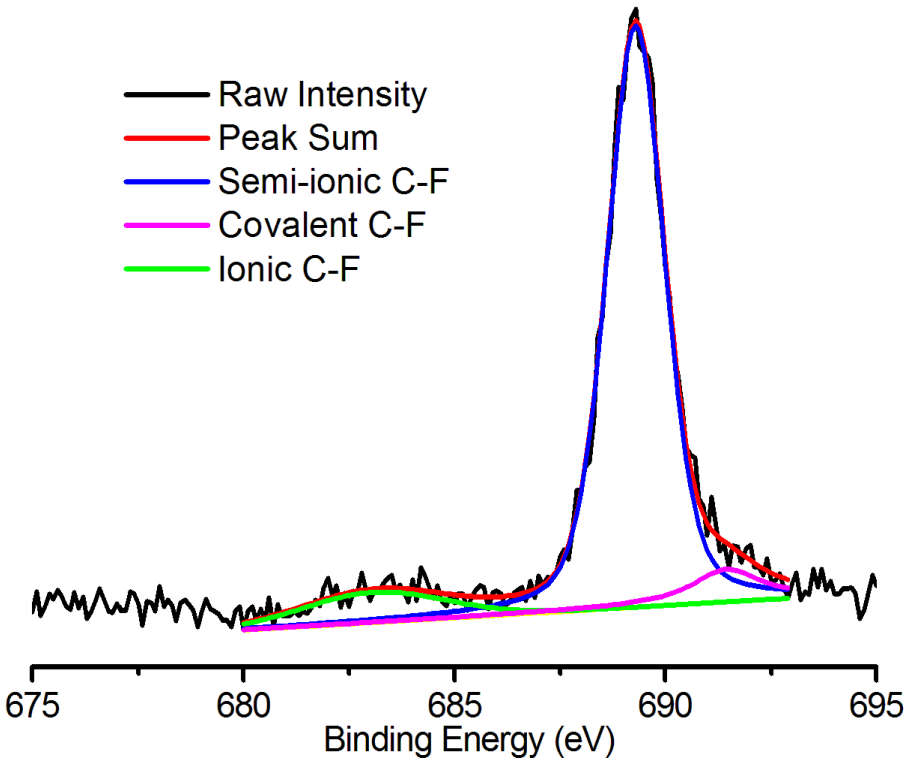

Fig. S67 XPS F 1s spectrum of CPM-131/C-700.

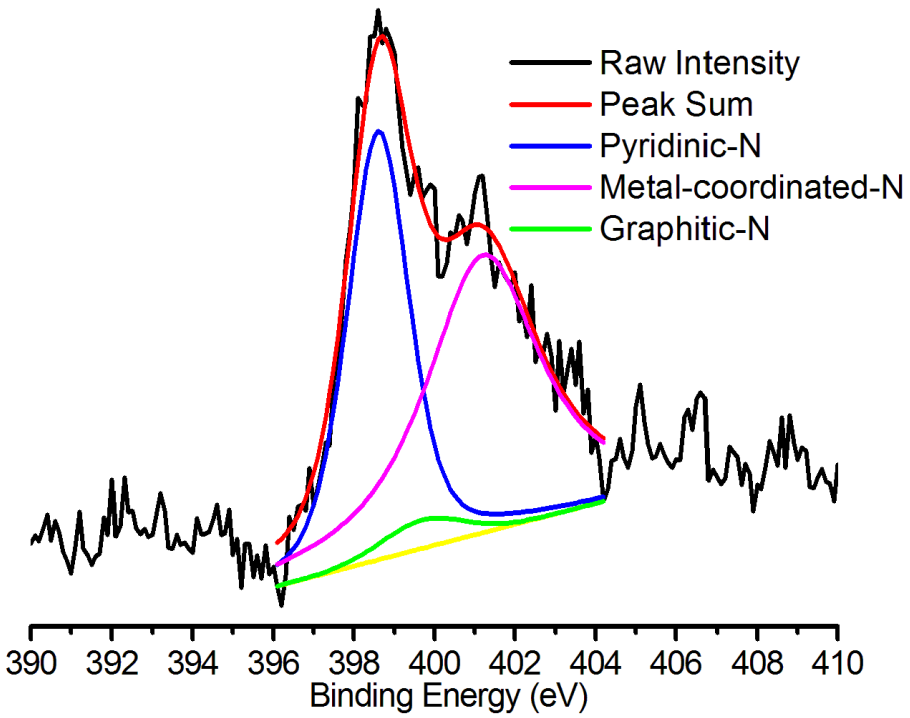

Fig. S68 XPS N 1s spectrum of CPM-131/C-700.

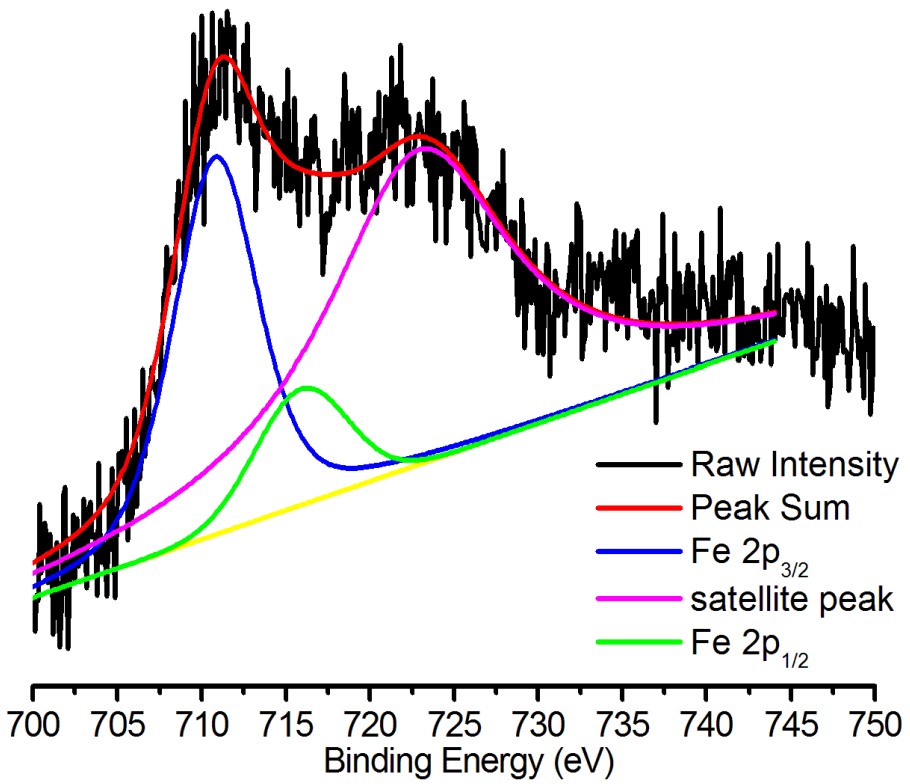

Fig. S69 XPS Fe 2p spectrum of CPM-131/C-700.

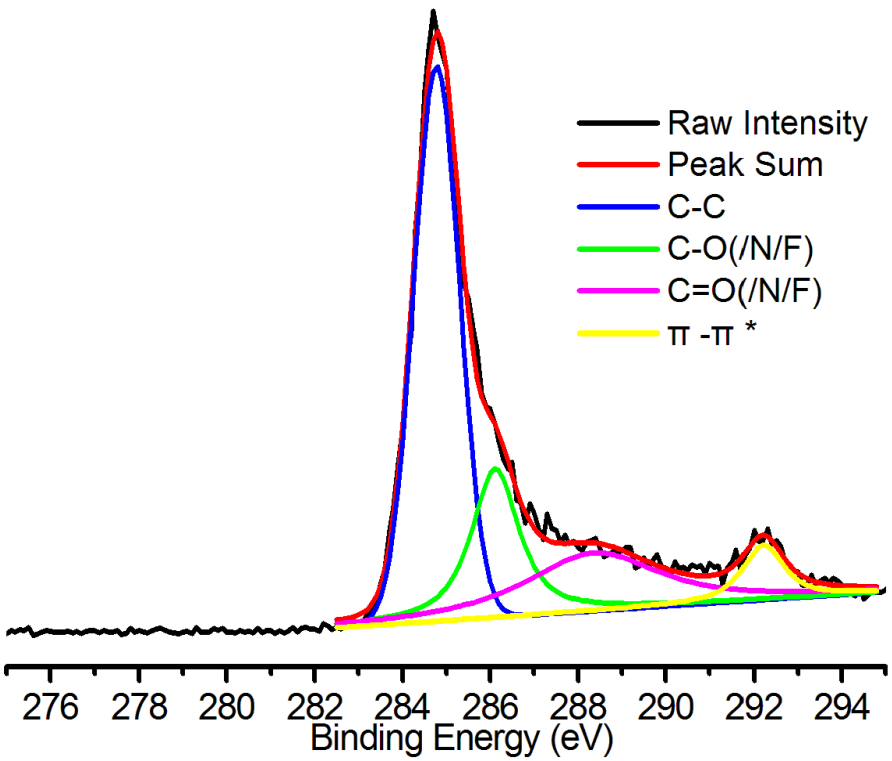

Fig. S70 XPS C 1s spectrum of CPM-131/C-700.

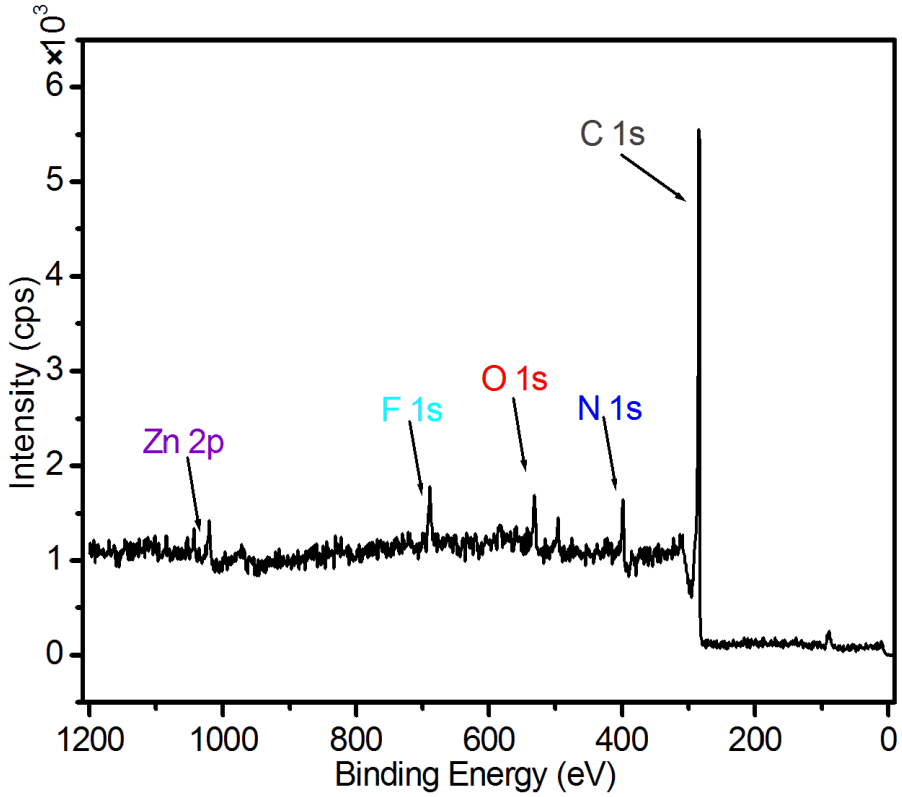

Fig. S71 XPS survey spectra of CPM-132/C-700.

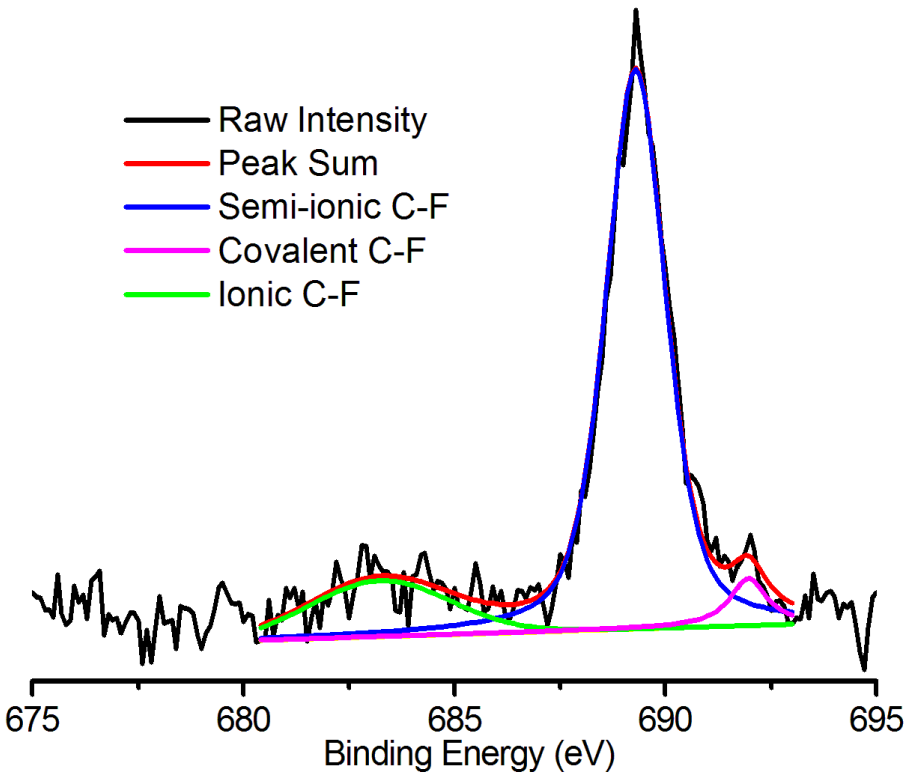

Fig. S72 XPS F 1s spectrum of CPM-132/C-700.

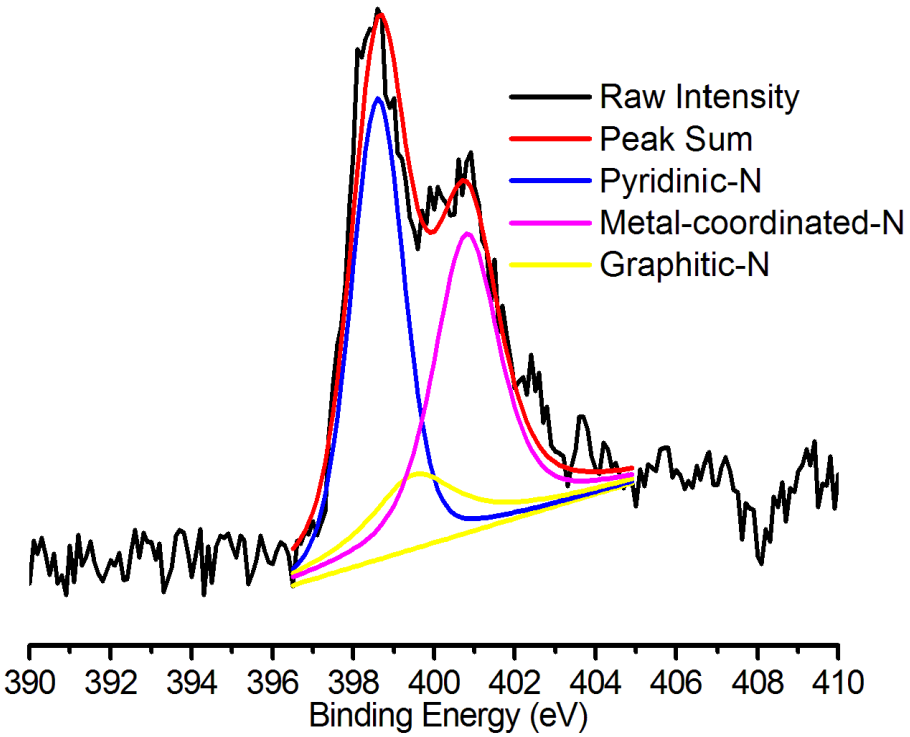

Fig. S73 XPS N 1s spectrum of CPM-132/C-700.

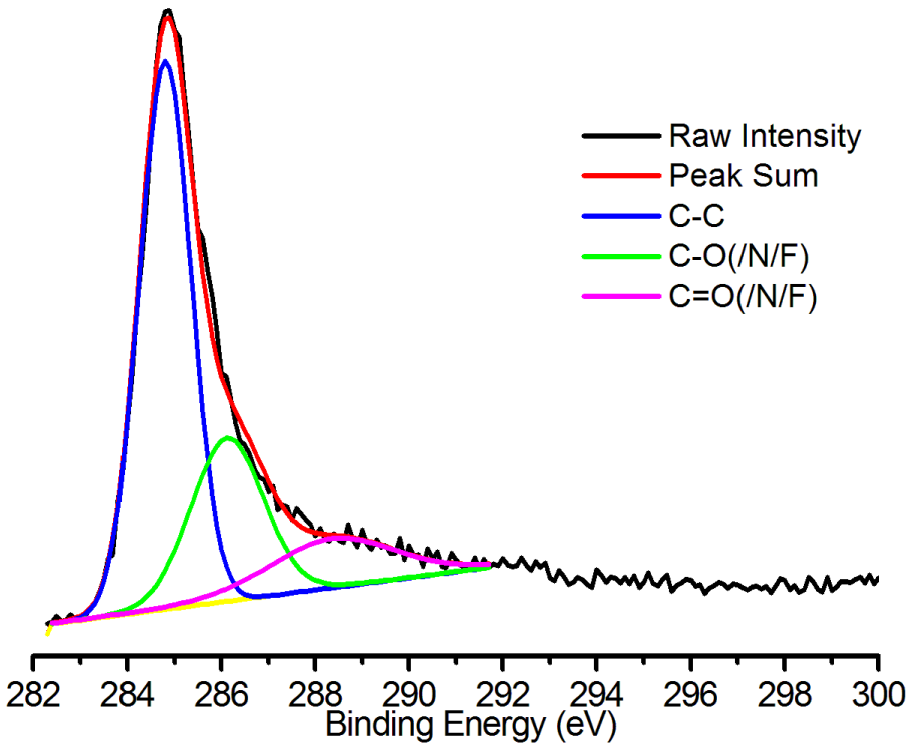

Fig. S74 XPS C 1s spectrum of CPM-132/C-700.

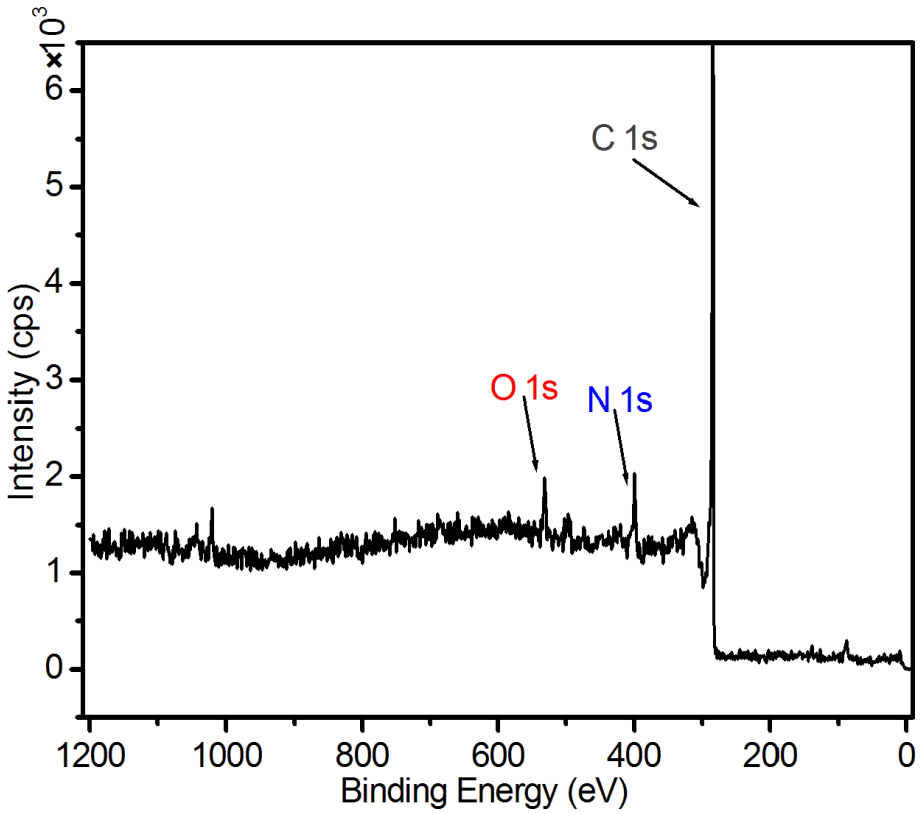

Fig. S75 XPS survey spectra of CPM-133/C-700.

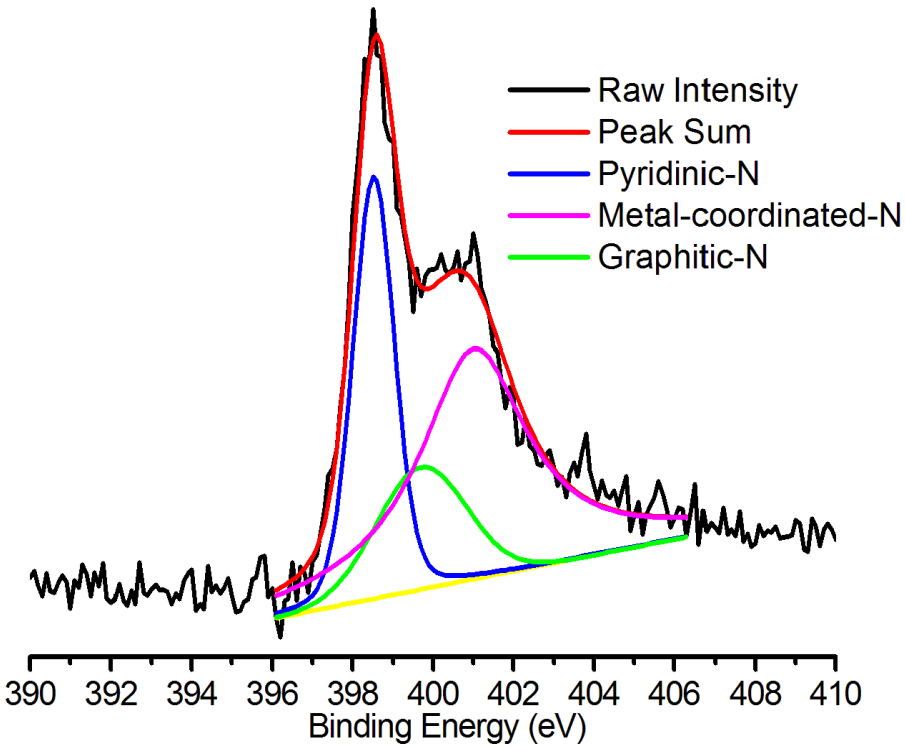

Fig. S76 XPS N 1s spectrum of CPM-133/C-700.

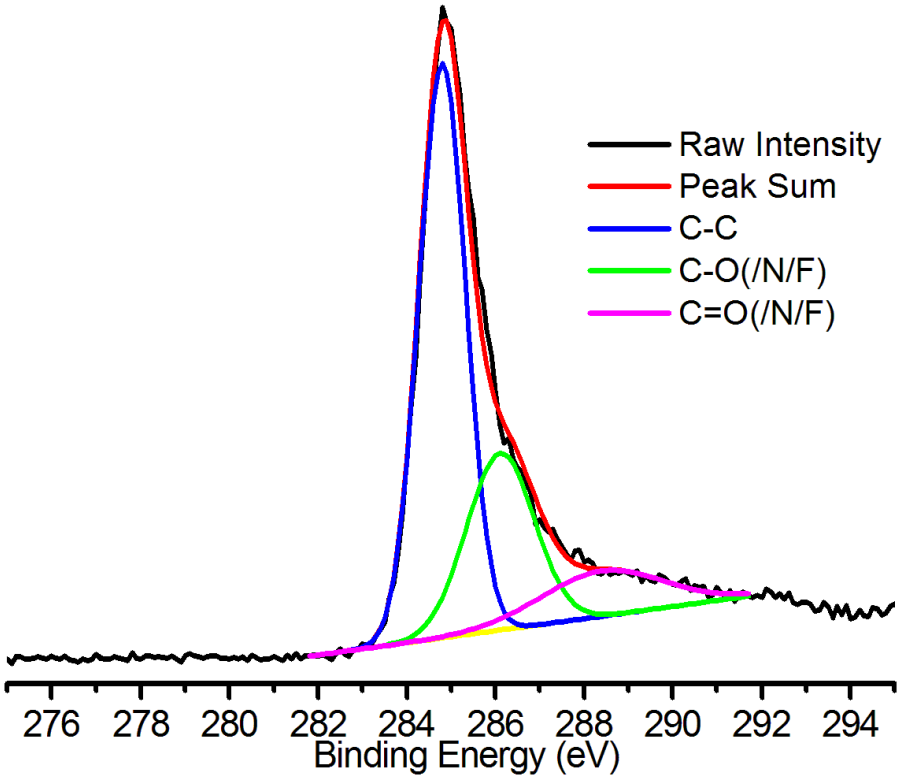

Fig. S77 XPS C 1s spectrum of CPM-133/C-700.

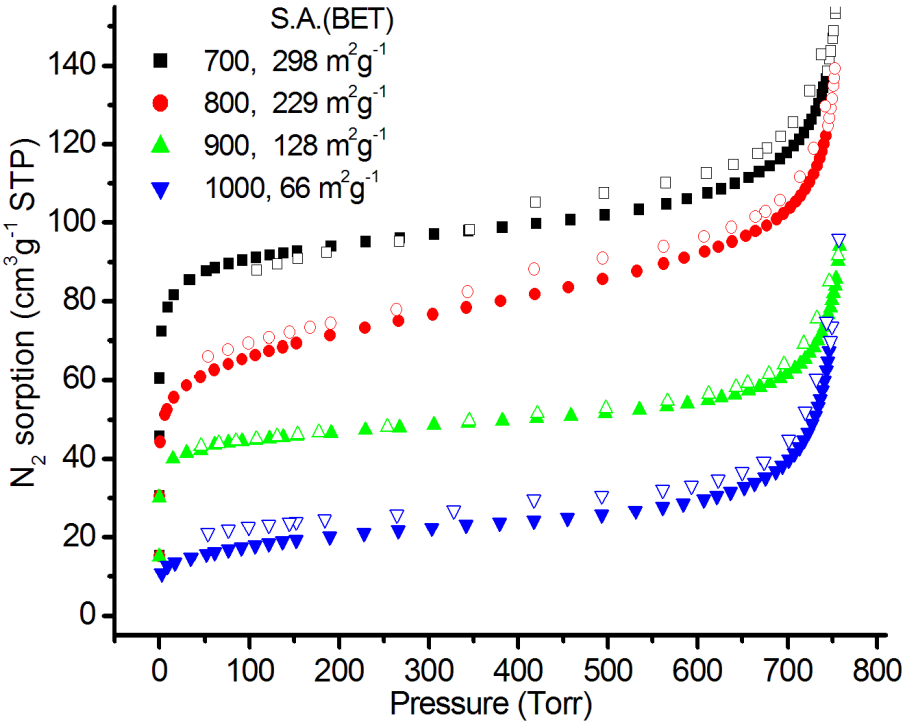

Fig. S78 N_2 sorption of CPM-131/C.

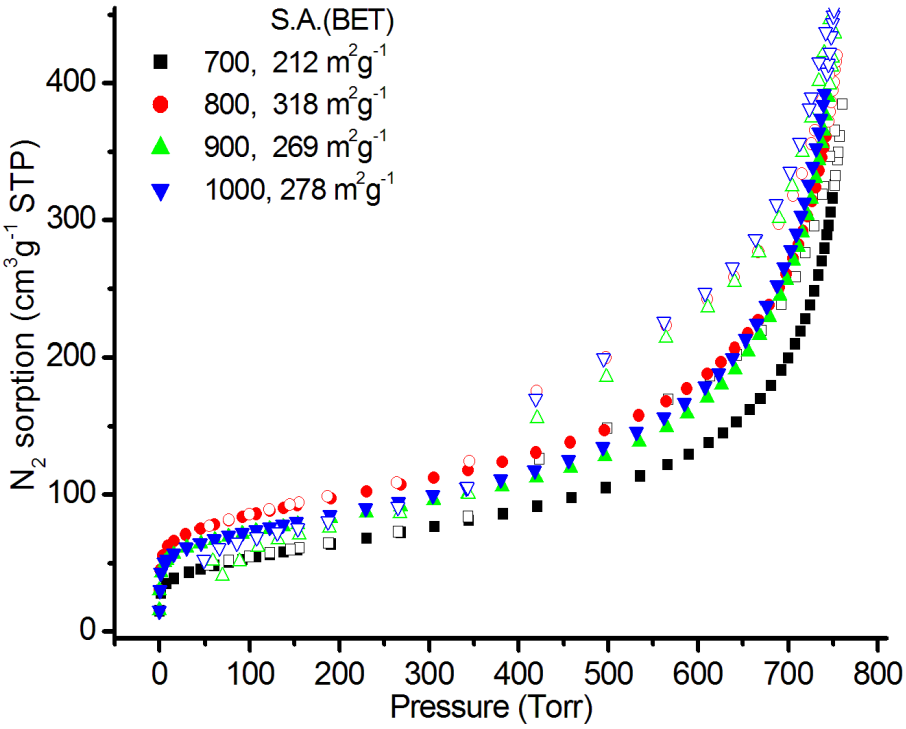

Fig. S79 N_2 sorption of CPM-132/C.

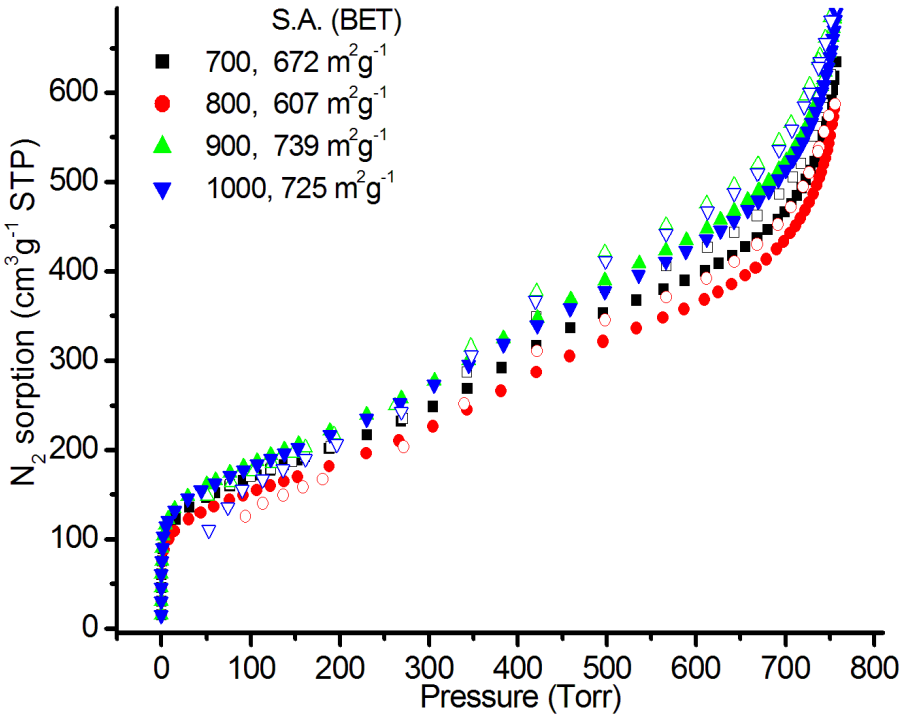

Fig. S80 N_2 sorption of CPM-133/C.

12. Electrocatalytic activities for ORR

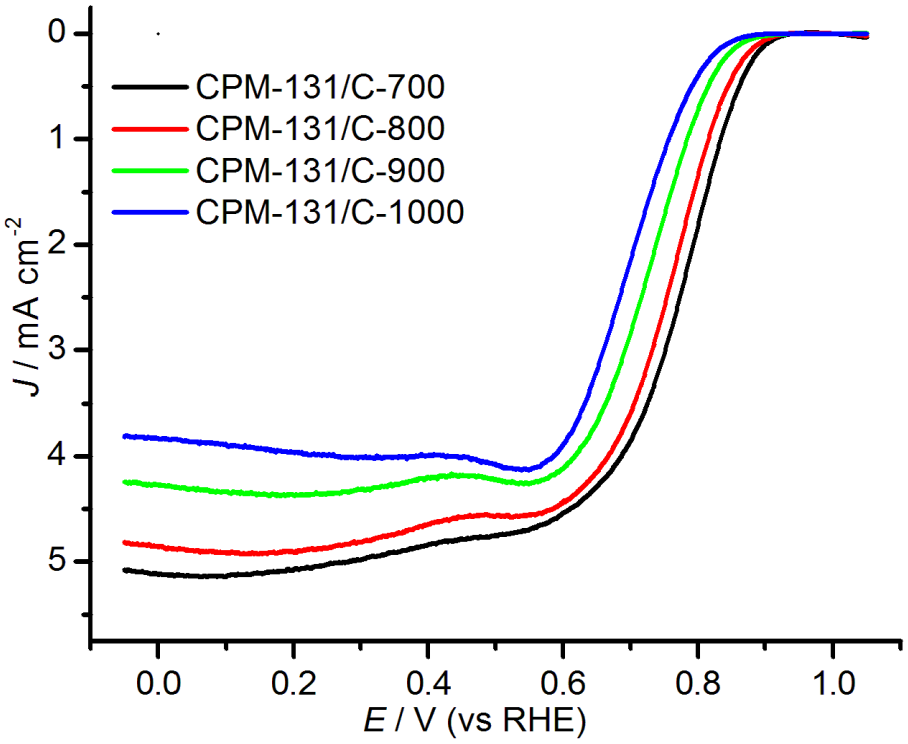

Fig. S81 LSV curves at rotation rate of 1600 rpm on CPM-131/C calcined at different temperature in O_2-saturated 0.1 M KOH solution.

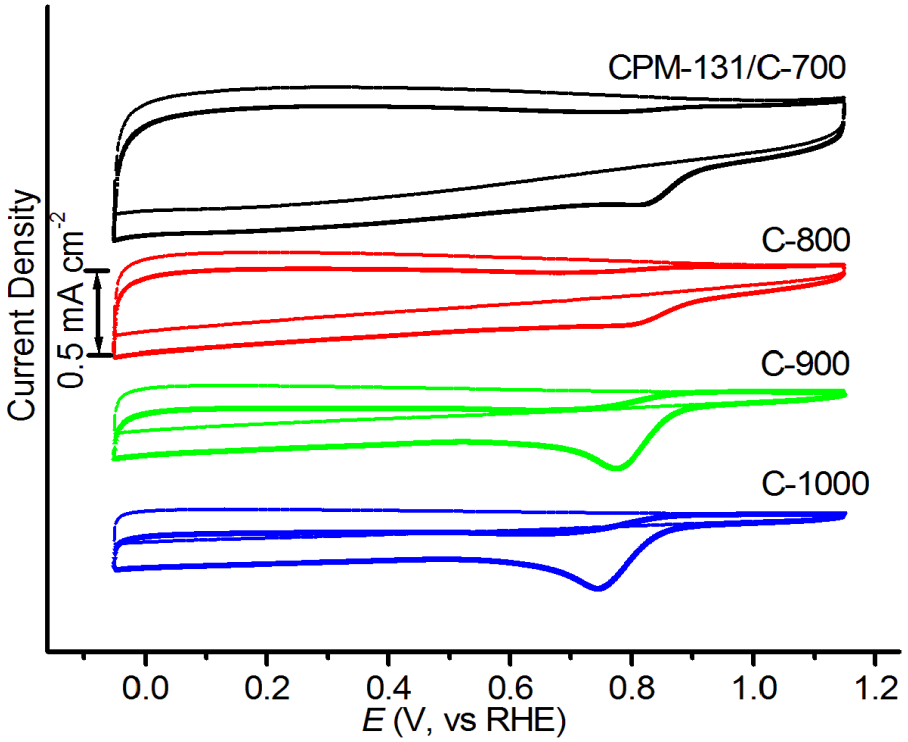

Fig. S82 CVs on CPM-131/C calcined at different temperature in O_2-saturated 0.1 M KOH solution.

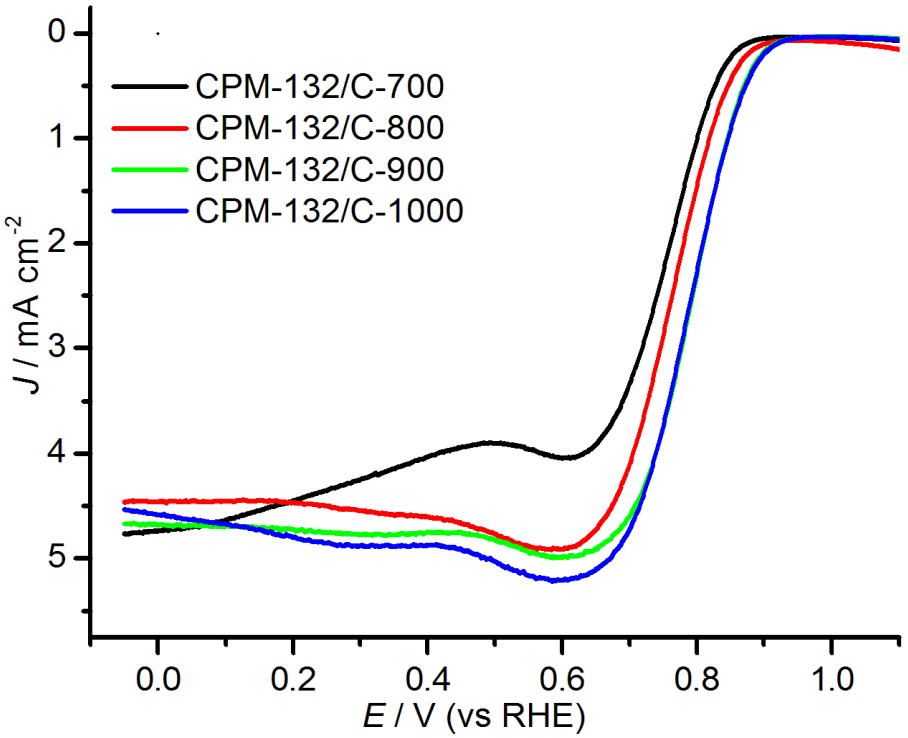

Fig. S83 LSV curves at rotation rate of 1600 rpm on CPM-132/C calcined at different temperature in O_2-saturated 0.1 M KOH solution.

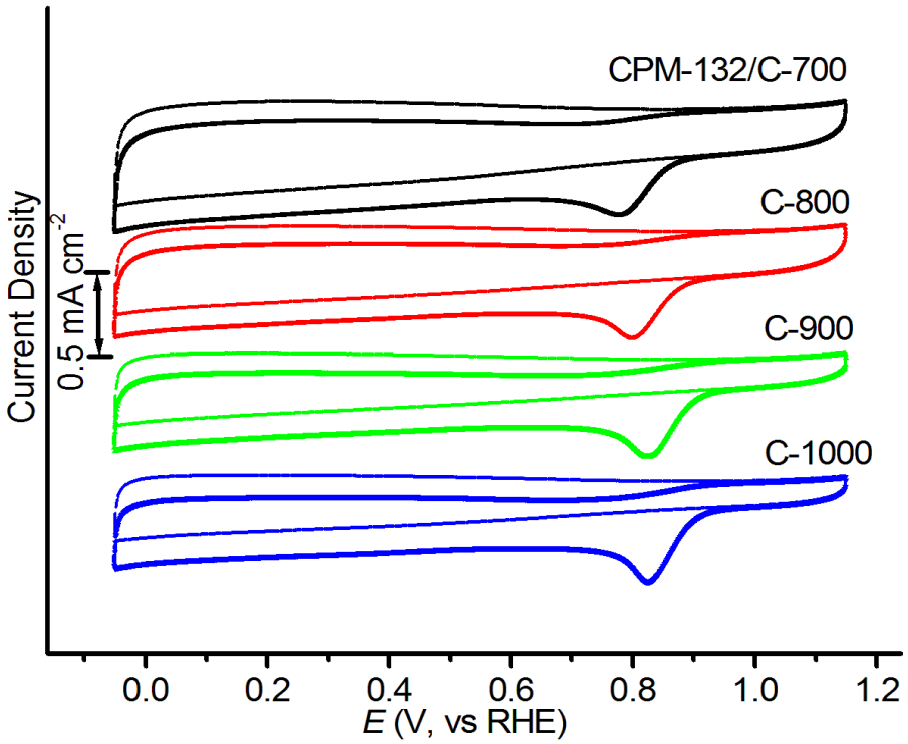

Fig. S84 CVs on CPM-132/C calcined at different temperature in O_2-saturated 0.1 M KOH solution.

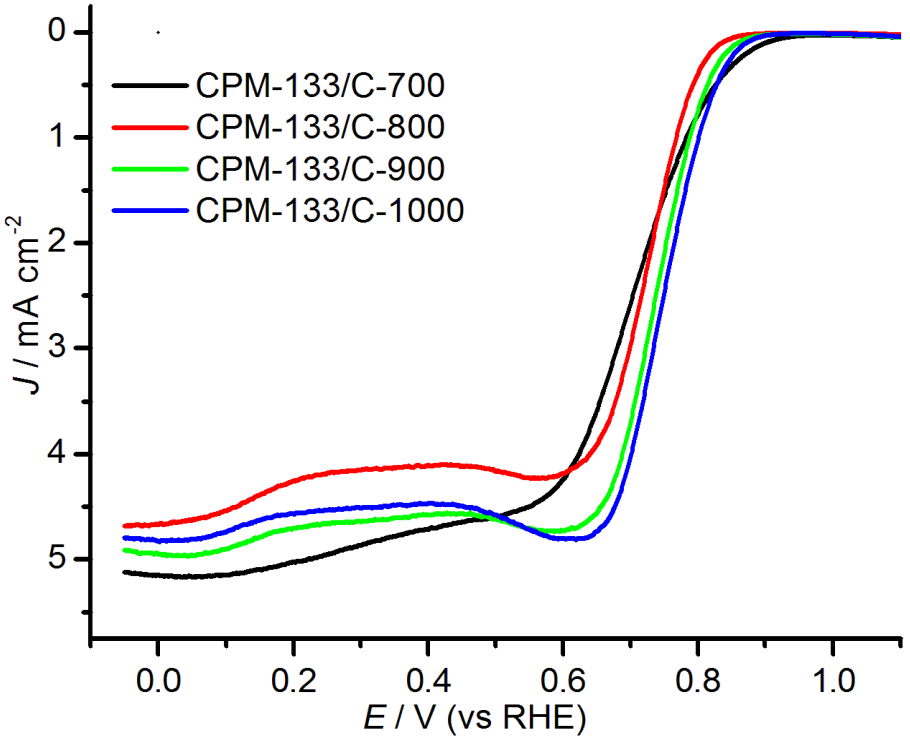

Fig. S85 LSV curves at rotation rate of 1600 rpm on CPM-133/C calcined at different temperature in O_2-saturated 0.1 M KOH solution.

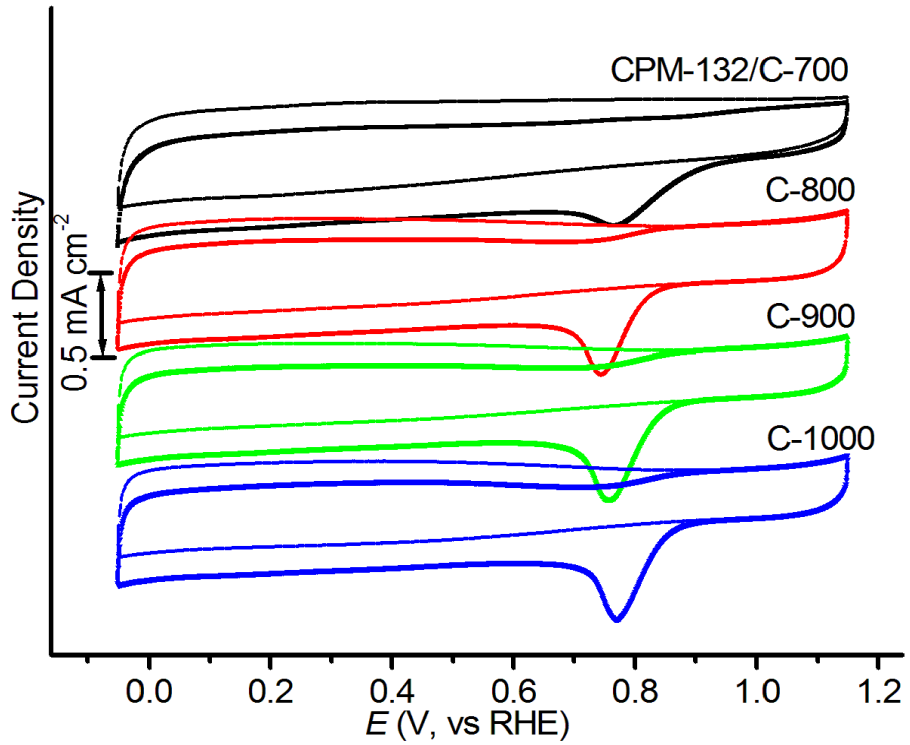

Fig. S86 CVs on CPM-133/C calcined at different temperature in O_2-saturated 0.1 M KOH solution.

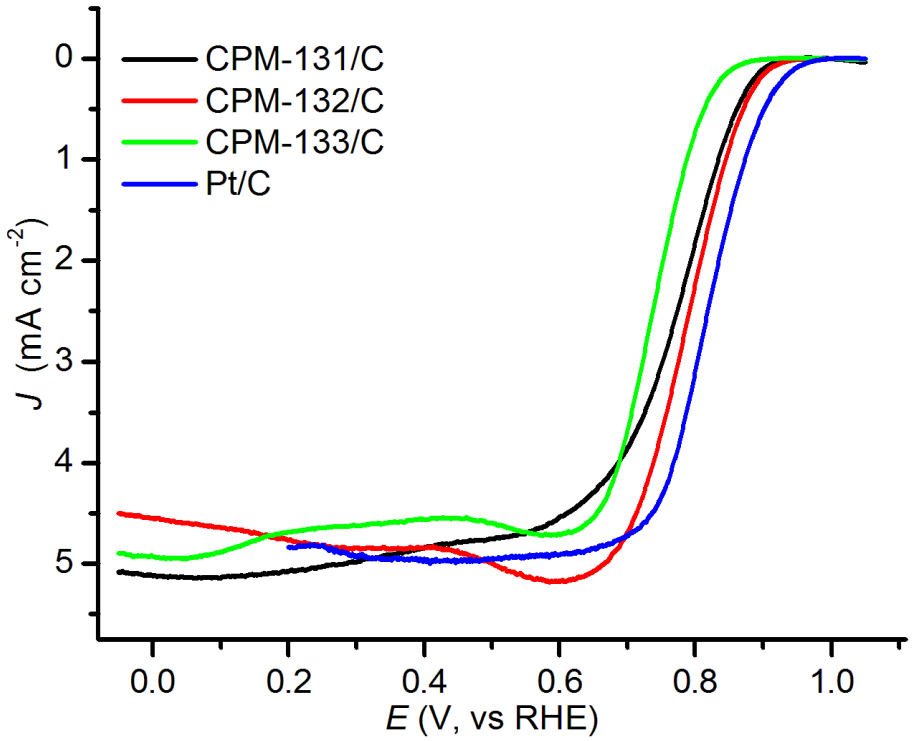

Fig. S87 LSV curves at rotation rate of 1600 rpm on CPM-13X/C and 20% Pt/C in O_2-saturated 0.1 M KOH solution.

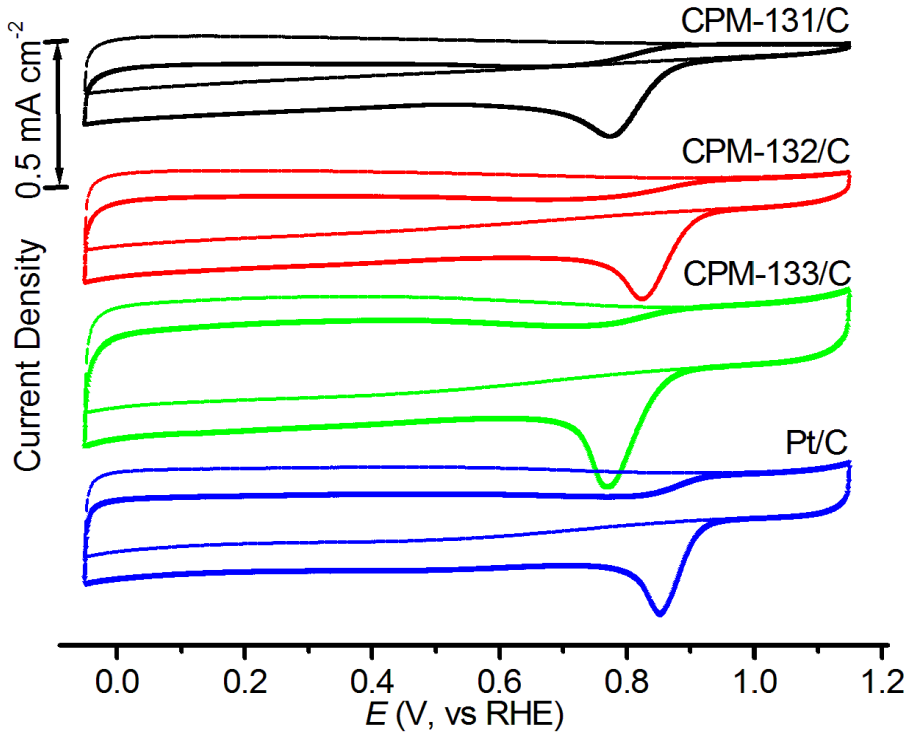

Fig. S88 CVs on CPM-13X/C and 20% Pt/C in O_2-saturated 0.1 M KOH solution.

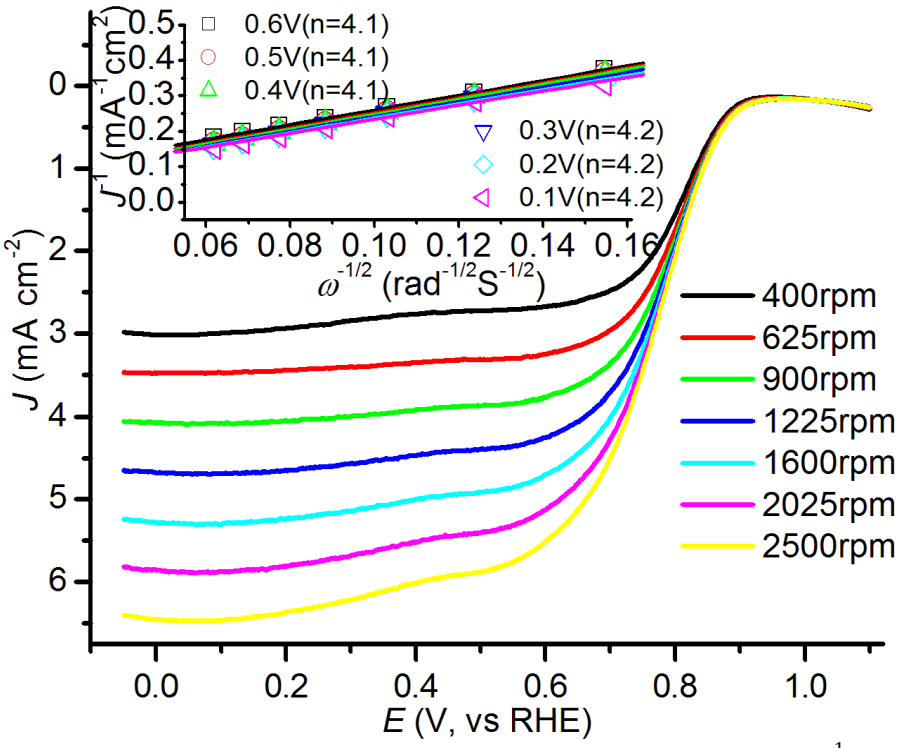

Fig. S89 LSV curves at different rotation rates with inset of K-L plots of J^{-1} versus ω^{-1} on CPM-131/C-1000 in O_2-saturated 0.1 M KOH solution.

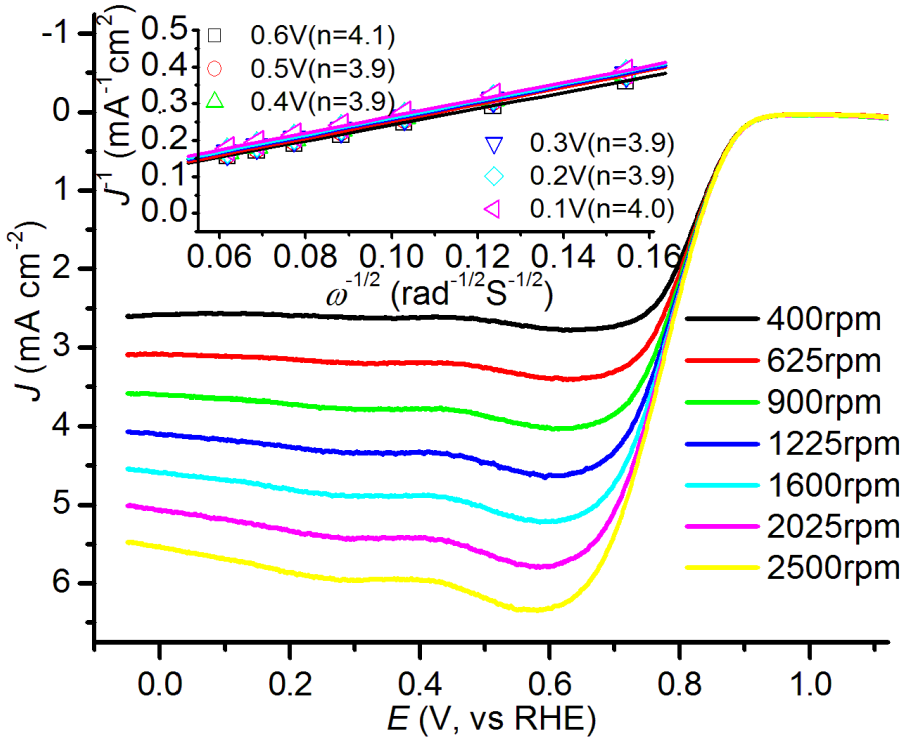

Fig. S90 LSV curves at different rotation rates with inset of K-L plots of J^{-1} versus ω^{-1} on CPM-132/C-1000 in O_2-saturated 0.1 M KOH solution.

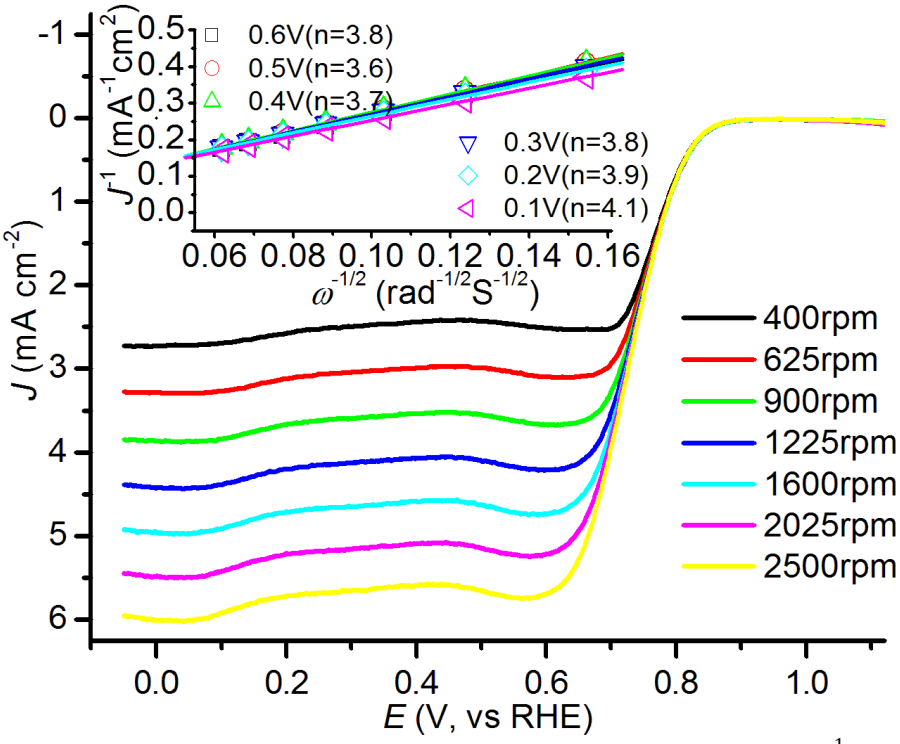

Fig. S91 LSV curves at different rotation rates with inset of K-L plots of J^{-1} versus ω^{-1} on CPM-133/C-1000 in O_2-saturated 0.1 M KOH solution.

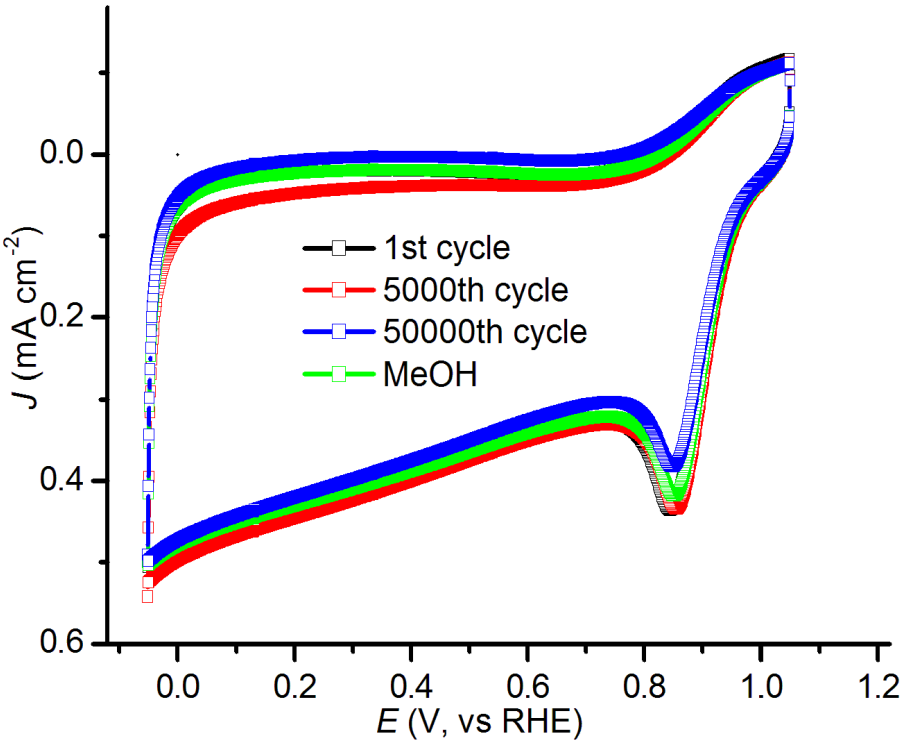

Fig. S92 Cycling CVs and methanol-poisoning effects over CPM-132/C-1000 in O_2-saturated 0.1 M KOH solution.

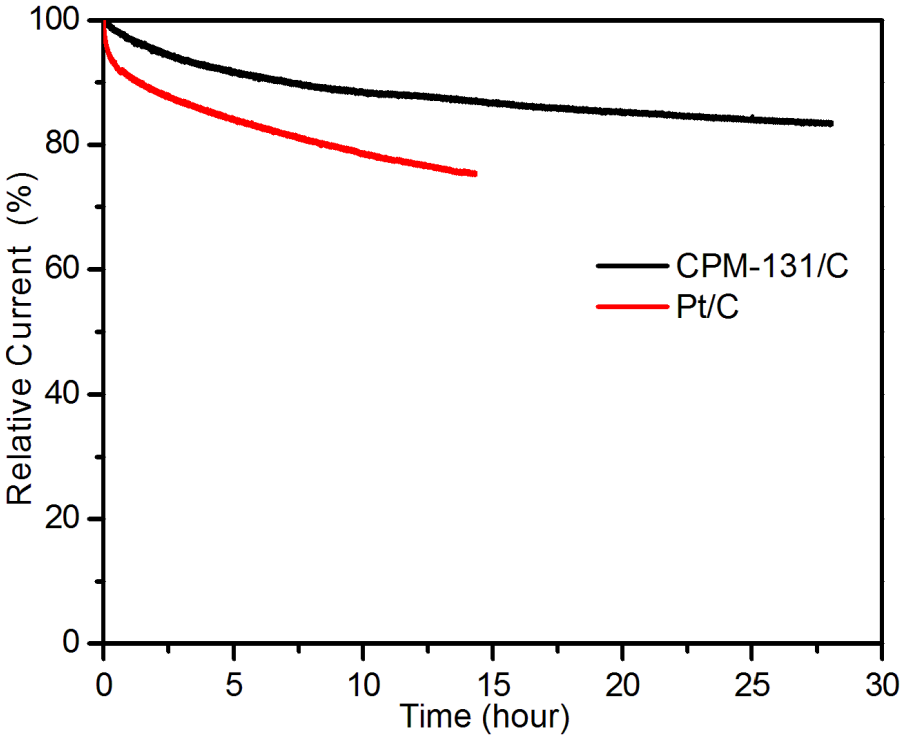

Fig. S93 Current-time (*i-t*) chronoamperometric response over CPM-132/C-1000 and 20% Pt/C in O_2-saturated 0.1 M KOH solution.

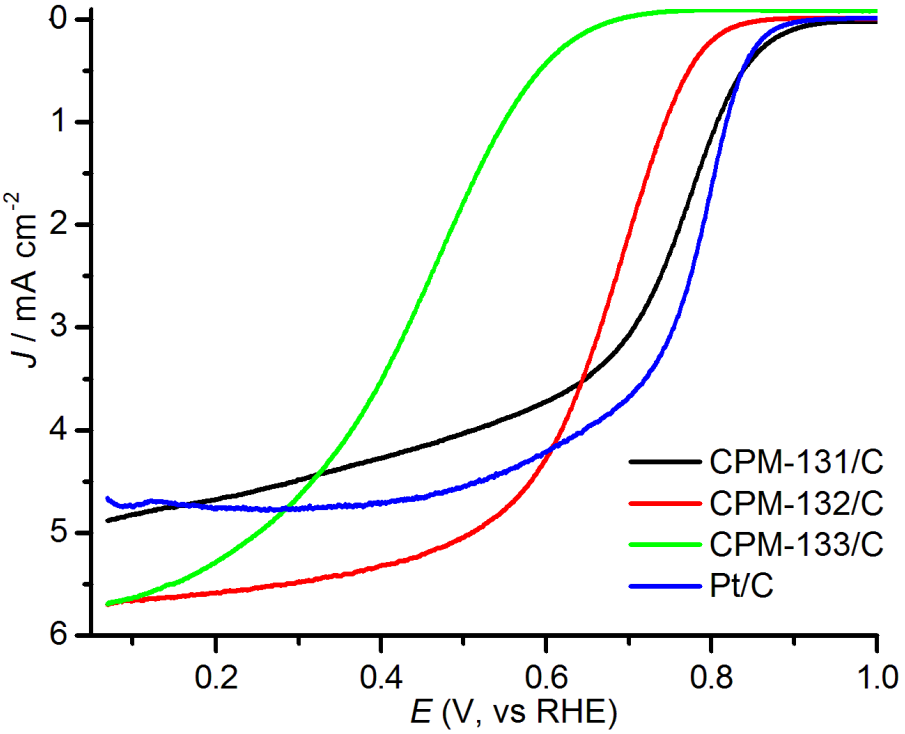

Fig. S94 LSV curves at rotation rate of 1600 rpm on CPM-13X/C and 20% Pt/C in O_2-saturated 0.1 M $HClO_4$ solution.

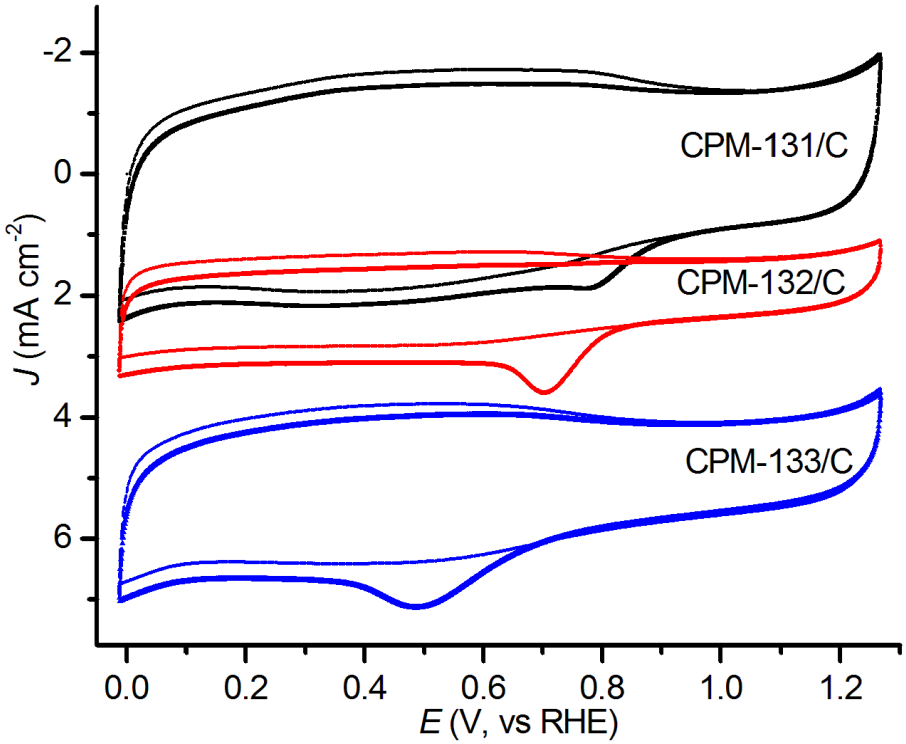

Fig. S95 CVs on CPM-13X/C and 20% Pt/C in O_2-saturated 0.1 M $HClO_4$ solution.

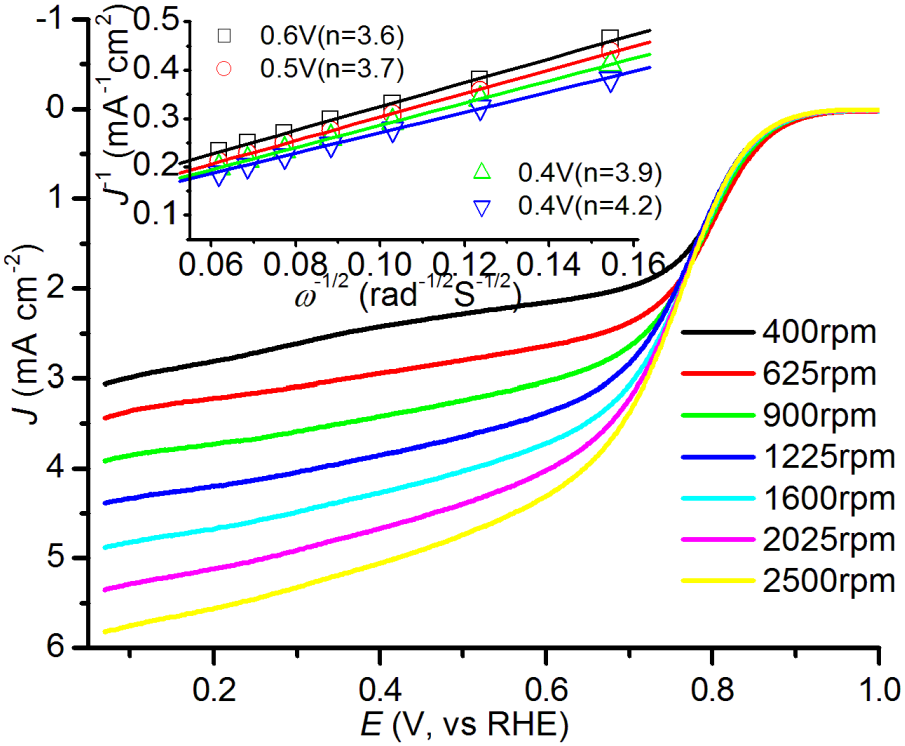

Fig. S96 LSV curves at different rotation rates with inset of K-L plots of J^{-1} versus ω^{-1} on CPM-131/C in O_2-saturated 0.1 M $HClO_4$ solution.

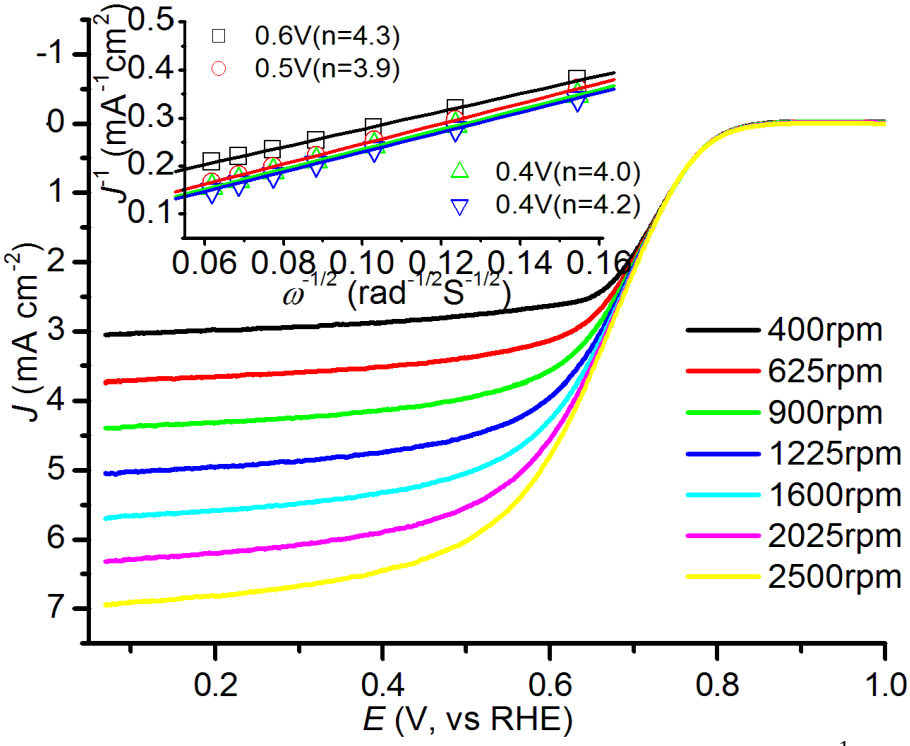

Fig. S97 LSV curves at different rotation rates with inset of K-L plots of J^{-1} versus ω^{-1} on CPM-132/C in O_2-saturated 0.1 M $HClO_4$ solution.

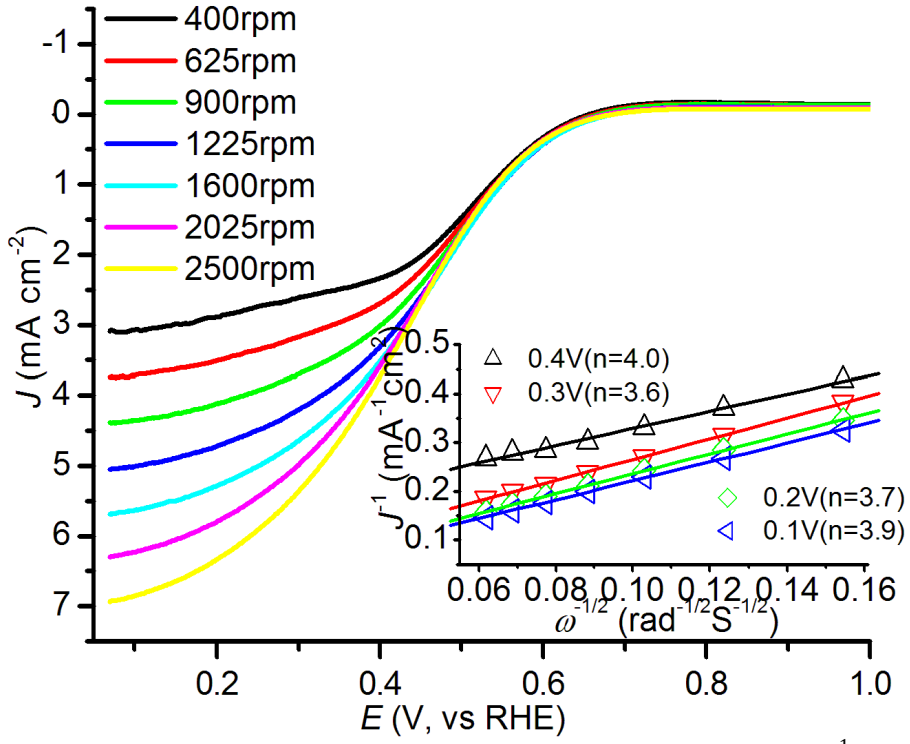

Fig. S98 LSV curves at different rotation rates with inset of K-L plots of J^{-1} versus ω^{-1} on CPM-133/C in O_2-saturated 0.1 M $HClO_4$ solution.

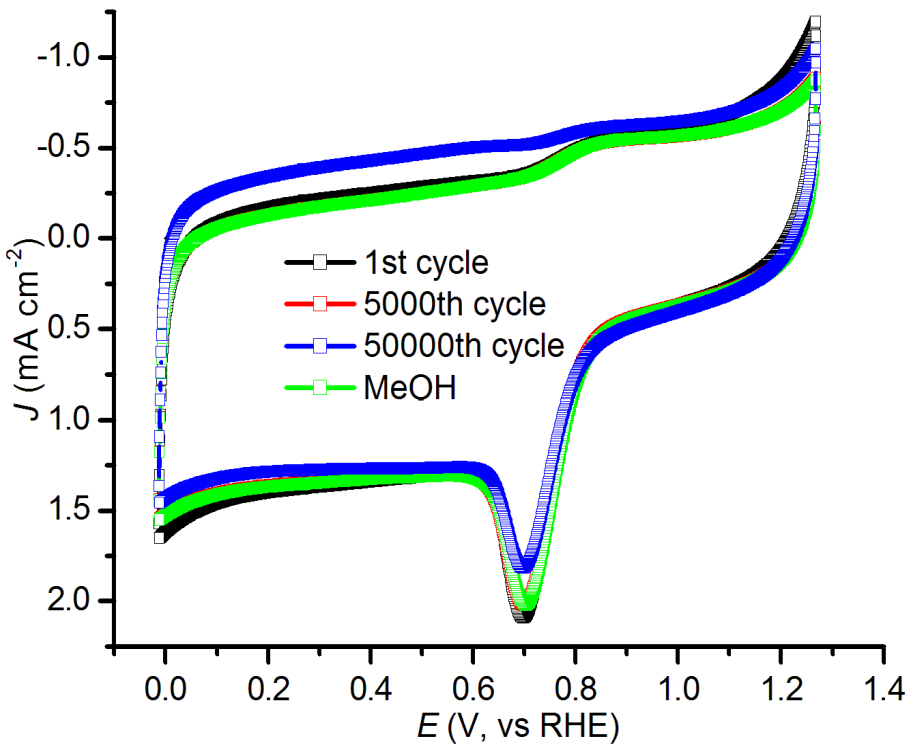

Fig. S99 Cycling CVs and methanol-poisoning effects over CPM-132/C-1000 in O_2-saturated 0.1 M $HClO_4$ solution.

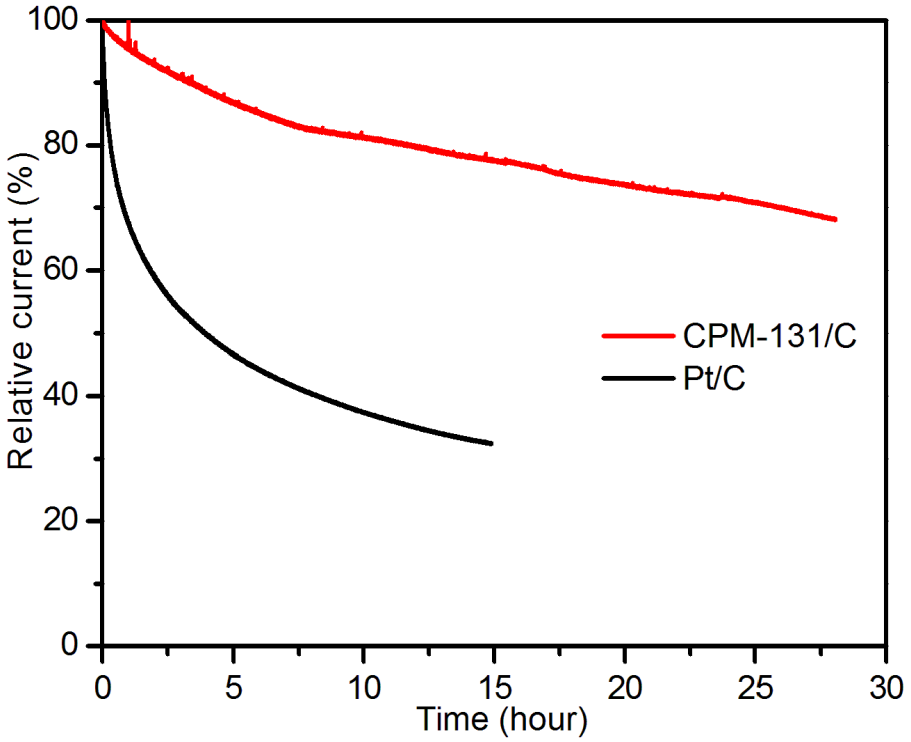

Fig. S100 Current-time (*i-t*) chronoamperometric response over CPM-132/C-1000 and 20% Pt/C in O_2-saturated 0.1 M $HClO_4$ solution at a scan rate of 10 mV s^{-1}.

13. Supplementary reference

1. ShelXTL, Version 5.1, G. M. Sheldrick, *Program for Crystal Structure Solution and Refinement*. Göttingen University, (Germany), 1997.
2. (a) A. D. Adler; F. R. Longo, J. D. Finarelli; J. Goldmacher; J. Assour; L. J. Korsakoff, *J. Org. Chem.*, **1967**, *32*, 476; (b) T. Aya and A. D. Hamilton, *Bioorg. Med. Chem. Lett.*, **2003**, *13*, 2651.